Paul J. Wilbur

NASA CR-135101

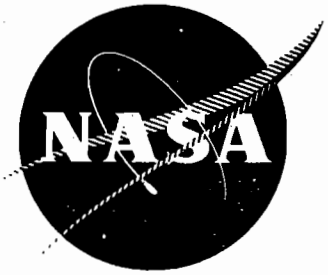

MULTIPOLE GAS THRUSTER DESIGN

PREPARED FOR

LEWIS RESEARCH CENTER

NATIONAL AERONAUTICS AND SPACE ADMINISTRATION

GRANT NSG-3011

by

Gerald C. Isaacson

Approved by

Harold R. Kaufman

June 1977

Department of Mechanical Engineering
Colorado State University
Fort Collins, Colorado

1. Report No.	2. Government Accession No.	3. Recipient's Catalog No.
CR-135101		

4. Title and Subtitle	5. Report Date
MULTIPOLE GAS THRUSTER DESIGN	June 1977
	6. Performing Organization Code
7. Author(s)	8. Performing Organization Report No.
Gerald C. Isaacson	
	10. Work Unit No.
9. Performing Organization Name and Address	11. Contract or Grant No.
Department of Mechanical Engineering Colorado State University Fort Collins, Colorado 80523	NSG 3011
	13. Type of Report and Period Covered
12. Sponsoring Agency Name and Address	Contractor Report
National Aeronautics and Space Administration Washington, D.C. 20546	14. Sponsoring Agency Code

15. Supplementary Notes

Grant Manager - Vincent K. Rawlin
NASA Lewis Research Center, Cleveland, Ohio 44135

This report is a reproduction of the Ph.D. Thesis of Gerald C. Isaacson.

16. Abstract

The development of a low field strength multipole thruster operating on both argon and xenon is described. The design makes extensive use of flat and cylindrical sheetmetal parts that can be easily fabricated. This, along with modular type construction, lends the design to rapid optimization and scaling. A simple theory is presented for determining the required integrated magnetic flux above the anodes and is compared with experimental results. The ion-chamber corner losses are evaluated and a corrective action in the form of recessing the corner anodes is implemented. Electron diffusion across the magnetic fringe field is examined and found to correspond to a turbulent plasma condition.

Experimental results were obtained with a 15-cm diameter multipole thruster and are presented for a wide range of discharge-chamber configurations. Minimum discharge losses were 300-350 eV/ion for argon and 200-250 eV/ion for xenon. Ion beam flatness parameters in the plane of the accelerator grid ranged from 0.85 to 0.93 for both propellants. Thruster performance is correlated for a range of ion chamber sizes and operating conditions as well as propellant type and accelerator system open area.

A 30-cm diameter ion source designed and built using the procedure and theory presented herein is shown capable of low discharge losses and flat ion-beam profiles without optimization. This indicates that by using the low field strength multipole design, as well as general performance correlation information provided herein, it should be possible to rapidly translate initial performance specifications into easily fabricated, high performance prototypes.

17. Key Words (Suggested by Author(s))	18. Distribution Statement
Electric Propulsion Ion Beams Ion Sources	Unclassified - unlimited

19. Security Classif. (of this report)	20. Security Classif. (of this page)	21. No. of Pages	22. Price*
Unclassified	Unclassified		

* For sale by the National Technical Information Service, Springfield, Virginia 22161

TABLE OF CONTENTS

Chapter		Page
	TABLE OF CONTENTS	ii
	LIST OF FIGURES	iii
I.	INTRODUCTION	1
	Thruster Operation	1
	Discharge Chamber Development	4
	Thruster Design	10
	Present Investigation	12
II.	APPARATUS	13
III.	PROCEDURE	19
IV.	THEORY	21
	Primary Electron Containment	21
	Maxwellian Electron Diffusion	24
	Neutral Loss	28
V.	EXPERIMENTAL RESULTS AND DISCUSSION	32
	Primary Electron Considerations	32
	Plasma Properties and Phenomena	41
	Effect of Discharge Chamber Configuration	60
	30-cm Diameter Multipole Source	72
	Performance Correlation	73
	Design Example	80
VI.	CONCLUSIONS	83
	REFERENCES	85
	APPENDIX	88

LIST OF FIGURES

Figure		Page
1.	Electron-Bombardment Ion Thruster.	2
2.	Discharge Chamber Types and Their Associated Beam Current Density Profiles	6
3.	Sketch of 15-cm Multipole Gas Thruster	14
4.	Iron Filing Magnetic-Field Map	22
5.	Electron Interaction with Fringe Magnetic Field Above Anode.	23
6.	Variation of Discharge Loss with Magnetic Field for MP-I .	33
7.	Variation of Discharge Loss with Magnet Current for Different Anode Configurations with Argon Propellant for MP-I	35
8.	Variation of Discharge Loss with Magnet Current for Different Anode Configurations with Xenon Propellant for MP-I	36
9.	Magnetic Field Between Pole Pieces of MP-I	37
10.	Variation of Discharge Loss with Magnet Current for MP-II.	40
11.	Anode Distribution of Discharge Current Per Unit Anode Length	42
12.	Effect of Anode Configuration on Discharge-Chamber Performance with Argon Propellant for MP-II.	43
13.	Effect of Anode Configuration on Discharge-Chamber Performance with Xenon Propellant for MP-II.	44
14.	Plasma Properties for 8.1 cm Chamber Length with Argon Propellant	46
15.	Plasma Properties for 8.1 cm Chamber Length with Xenon Propellant	48
16.	Variation of Discharge-Chamber Performance for Different Anode Widths with Argon Propellant	50
17.	Variation of Discharge-Chamber Performance for Different Anode Widths with Xenon Propellant	51

Figure Page

18. Plasma Property Contours for 8.1 cm Chamber Length with Argon Propellant 53

19. Plasma Property Contours for 8.1 cm Chamber Length with Xenon Propellant 55

20. Comparison of Calculated and Measured Discharge Currents at Various Maxwellian Number Densities for Electron Temperatures of about 5 and 10 eV with Argon Propellant. 58

21. Comparison of Calculated and Measured Discharge Currents at Various Maxwellian Number Densities for Electron Temperatures of about 5 and 10 eV with Xenon Propellant. 59

22. Effect of Chamber Length on Discharge-Chamber Performance with Argon Propellant. 61

23. Effect of Chamber Length on Ion Beam Profiles with Argon Propellant. 63

24. Effect of Chamber Length on Discharge-Chamber Performance with Xenon Propellant. 64

25. Effect of Chamber Length on Ion Beam Profiles with Xenon Propellant 66

26. Effect of Flow Rate on Discharge-Chamber Performance with Argon Propellant. 68

27. Effect of Flow Rate on Ion Beam Profiles with Argon Propellant 69

28. Effect of Flow Rate on Discharge-Chamber Performance with Xenon Propellant. 70

29. Effect of Flow Rate on Ion Beam Profiles with Xenon Propellant 71

30. Discharge-Chamber Performance for 30 cm Diameter Ion Source with Argon Propellant 74

31. Ion Beam Profile for 30 cm Diameter Ion Source with Argon Propellant 75

32. Performance Correlation for all Discharge-Chamber Lengths and all Flow Rates with Argon Propellant 77

Figure Page

33. Performance Correlation for all Discharge-Chamber Lengths and all Flow Rates with Xenon Propellant 78

34. General Performance Correlation for all Discharge-Chamber Lengths and all Flow Rates for Both Argon and Xenon Propellants with MP-II and for the 30 cm Ion Source with Argon Propellant 79

A-1 Effect of Discharge Current and Voltage on Double to Single Ion Current Ratio for Various Flow Rates with Argon Propellant. 90

A-2 Effect of Discharge Current and Voltage on Double to Single Ion Current Ratio for Various Flow Rates with Xenon Propellant. 91

I. INTRODUCTION

The primary objective of this investigation was to understand the operation of the low field strength multipole ion source. A further objective was the development of scaling relationships that would permit new high-performance multipole ion sources to be designed without the usual trial-and-error development program. Both argon and xenon were used as propellants. Xenon appears to be the gas best suited for space propulsion with high atomic weight and ease of storage being the major factors in this choice. Argon is a possible alternative if tons of propellant are required (so that cryogenic storage is practical) and excess electrical power makes efficiency (and hence atomic weight) less important. Both of these gases offer environmental advantages over the usual propellants of cesium and mercury. Argon is also the preferred propellant in the recent ground applications of thruster technology such as cleaning, micromachining, and ion etching of solid-state devices.

Thruster Operation

A sketch of a typical electron-bombardment ion source is shown in Figure 1. It consists of a cylindrical discharge chamber bounded on the sides by an anode, on the upstream end by the body, and on the downstream end by the accelerator system. During operation, neutral propellant is introduced into the chamber where it is ionized through electron bombardment. These electrons are emitted by the cathode which is maintained 30-50 V negative of the anode. This potential difference is determined by the need to accelerate the electrons to the energy

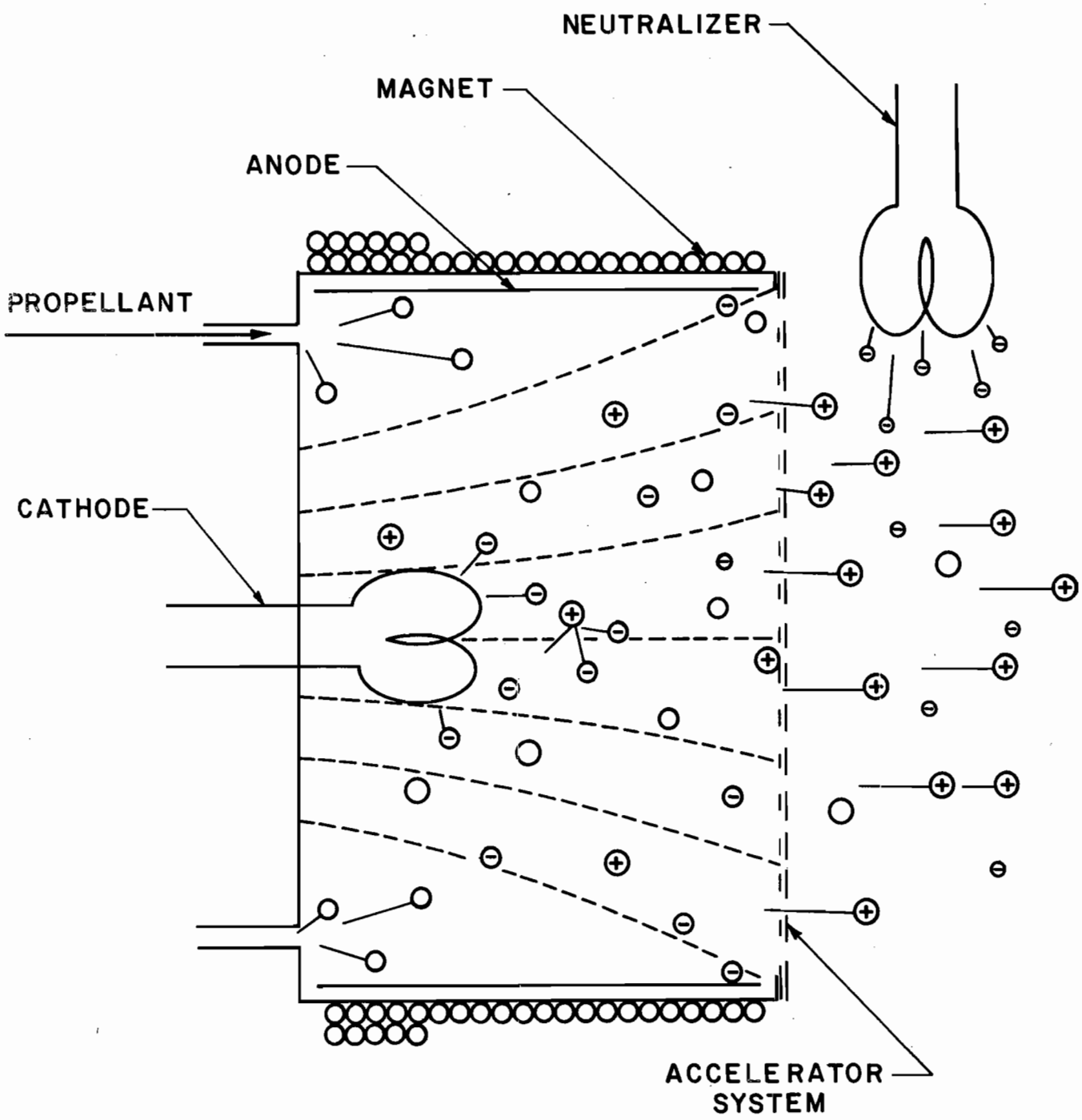

Figure 1. Electron-bombardment ion thruster.

range where the ionization cross section is near maximum for the given propellant. These energetic, or primary, electrons are constrained by the ends of the discharge chamber which are maintained at cathode potential and by a magnetic field which prevents them from having direct access to the anode. The magnetic field is required because the mean free path for an electron-neutral collision is on the order of a few meters while the discharge chamber dimensions are typically measured in centimeters. Although the primary electrons make up only about 10 percent of the total electron population, they account for roughly half of the ionizations. The remainder of the electron population is made up of the lower energy electrons produced as a result of collision processes. These electrons rapidly randomize into an approximate Maxwellian distribution with a characteristic temperature of about 5 eV. Because of their lower energy and hence higher cross-section for coulomb collisions, these electrons then migrate across the magnetic field and are collected by the anodes.

On the basis of the physical model just presented, the azimuthal boundary of the volume containing the primary electrons is defined approximately by the first magnetic field line that does not intersect the anode. Primary electrons are restricted to this volume because the anode sheath is small and will not reflect any energetic electrons that reach it, hence, any primary electron on a field line that does intersect the anode will be lost. Because of this primary electron containment, the bulk of the ionization will also take place within this region.

The ions produced within the discharge chamber move with near equal probability in all directions. Those reaching the downstream end are

extracted out through the accelerator system and form the ion exhaust beam. The ion accelerator system consists of two closely spaced (~1 mm) perforated grids. The inner (or screen) grid, along with the body and the cathode, is maintained at a high positive potential (~1 to 3 kV) with respect to the spacecraft or the test facility ground. This grid has an open area fraction of typically 60 to 70 percent and, as a result, nearly all of the ions reaching it are extracted. The outer (or accelerator) grid is maintained at a negative potential (typically-0.5 to -1.5 kV) and usually has a lower open area fraction (~25 to 40%). The reduction in open area for the accelerator grid increases the restriction to neutrals, thus reducing the neutral atom loss rate. Both grids can be made slightly spherical in shape to improve their mechanical stability to thermal gradients.

For space applications, the resulting ion beam must be current neutralized, to avoid charge buildup on the spacecraft, and charge neutralized, to avoid charge buildup within the ion beam. This need for neutralization, however, is somewhat diminished in ground applications. Current neutralization may be unnecessary due to ground return circuits while charge neutralization may be obtained from secondary electrons at the target. The use of a neutralizer in ground applications is usually advantageous, though, because it offers the advantage of better operating stability, together with a slightly smaller beam spread.

Discharge Chamber Development

Throughout the development of the electron-bombardment ion thruster, major objectives have been high electrical efficiency, high propellant utilization, and uniformity of the ion beam current density

profile. The first two correspond to the minimization of power and neutral propellant losses which is an obvious requirement for space propulsion, while uniformity of the ion-beam profile will result in more efficient use of the ion beam area. The power and neutral losses tend to be less important in ground applications, but the uniformity is often critical in ion machining.

In an effort to satisfy these various objectives, several different designs have been developed. Since, as previously indicated, the bulk of the ionization takes place within a primary-electron region that is defined by the magnetic field, it is not surprising that many of the improvements have been associated with changes in the magnetic field shape. In addition, studies have shown that a good correlation exists between the ion beam profile at the accelerator grid and the ion number density profile at the screen grid.[1,2] Therefore, modification of this region would be expected to strongly affect both the performance and the ion beam profile.

The electron-bombardment thruster started as a simple cylinder with a nearly uniform magnetic field roughly parallel to its axis.[3,4] The first change in the field shape was to make it moderately divergent as shown in Figure 2 (a). In this design, the magnetic field strength decreases in the downstream direction. Typical performance for mercury propellant obtained with a 10 cm (anode diameter) thruster operating at a beam current of 0.125 A was 500 eV/ion with a propellant utilization of 80 percent.[5] The ion beam profile, however, was very peaked. This peaked profile can be explained by examining the primary electron region within the thruster. The energetic electrons are emitted by the cathode which is located on the centerline of the discharge chamber. These

(a) MILDLY DIVERGENT FIELD SHAPE

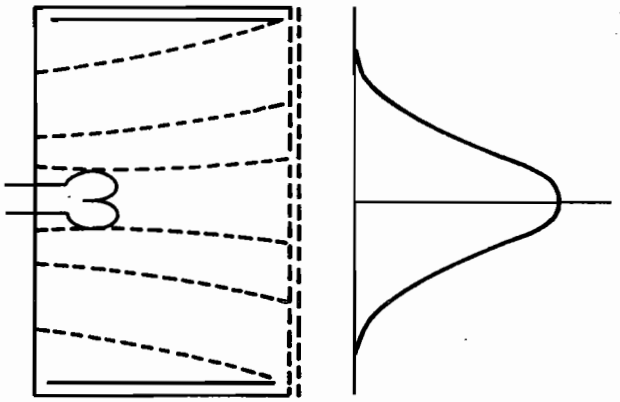

(b) STRONGLY DIVERGENT FIELD SHAPE

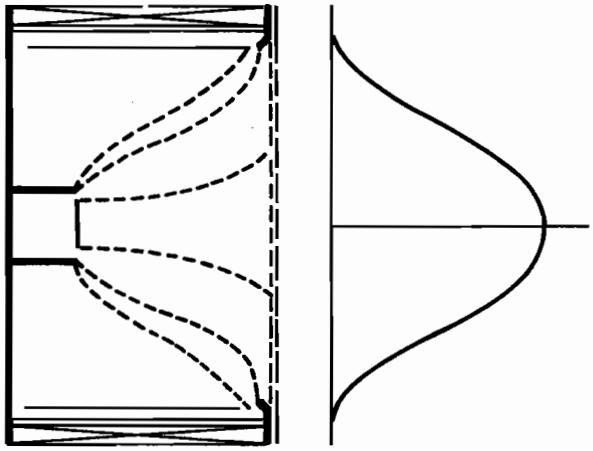

Figure 2. Discharge chamber types and their associated beam current density profiles.

electrons have direct access to only a small central portion of the discharge chamber. In order to reach the remainder of the chamber they must experience energy depleting collisions. This results in an electron energy distribution across the chamber with the most energetic electrons being in the center. Since the high energy electrons are more efficient in the ionization process than the lower energy electrons, the bulk of the ionization would be expected to occur near the centerline of the chamber as is indicated by the peaked ion beam profile shown in Figure 2 (a). The strongly divergent field shape of Figure 2 (b) was developed in an extensive test program. With a 15 cm diameter thruster using mercury propellant, discharge losses of about 200 eV/ion with propellant utilizations of about 85 percent were obtained at an ion beam current of 0.250 A.[6] Much of the improvement in performance in this design is due to the primary electrons now having direct access to the entire discharge chamber cross-section, which results in increased ionization near the boundaries. This explanation is supported by the substantial improvement in the uniformity of the ion beam profile.

Comparison of the primary electron region shape and the ion beam profile indicates that one is nearly the mirror image of the other. Since the ion beam density appears to be a function of the depth of the primary electron region, this suggests that further improvement in the uniformity of the ion beam profile could be obtained by making the depth of the primary electron region more uniform across the diameter. This can be explained by the residence-time theory which is discussed in detail in the literature[7,8,9] and will only be summarized here.

If it is assumed that all ionizations take place within the primary electron region, then the probability of a neutral being ionized is a function of its residence-time within this region. For a neutral drifting straight through the discharge chamber, this residence-time is then a function of the particle velocity and the depth of the region. Thus, near the boundaries where the depth of the primary electron region is small, fewer ionizations will occur than in the center where the depth is much greater.

Recent magnetic field configurations reported by Knauer, et al.,[2] Beattie,[9] Moore, [10] and Ramsey[11] offer different designs through which the uniformity of the primary electron region has been increased. The radial field thruster of Knauer, et al. is shown in Figure 2 (c) and might be considered as a limiting case of the divergent field approach. Here the magnetic field lines are predominantly radial and the anode is located at the upstream end of the discharge chamber. Thus the primary electrons have direct access to a region that extends over the entire discharge chamber cross-section and is of nearly uniform depth. The 15 cm diameter thruster operated by Knauer, et al. obtained losses as low as 180 eV/ion at 90% utilization and a beam current of 0.265 A. In addition, a very flat ion beam profile was obtained.

The cusped magnet field thruster of Beattie is also a modification of the strongly divergent field design. As shown in Figure 2 (d), a second pole piece was added between the existing anode and cathode pole pieces. This produced the cusped magnetic field and results in an increased primary electron region depth near the boundaries. Operation of this thruster yielded losses of about 250 eV/ion at 85% utilization with a beam current of about 0.600 A. At the time that this

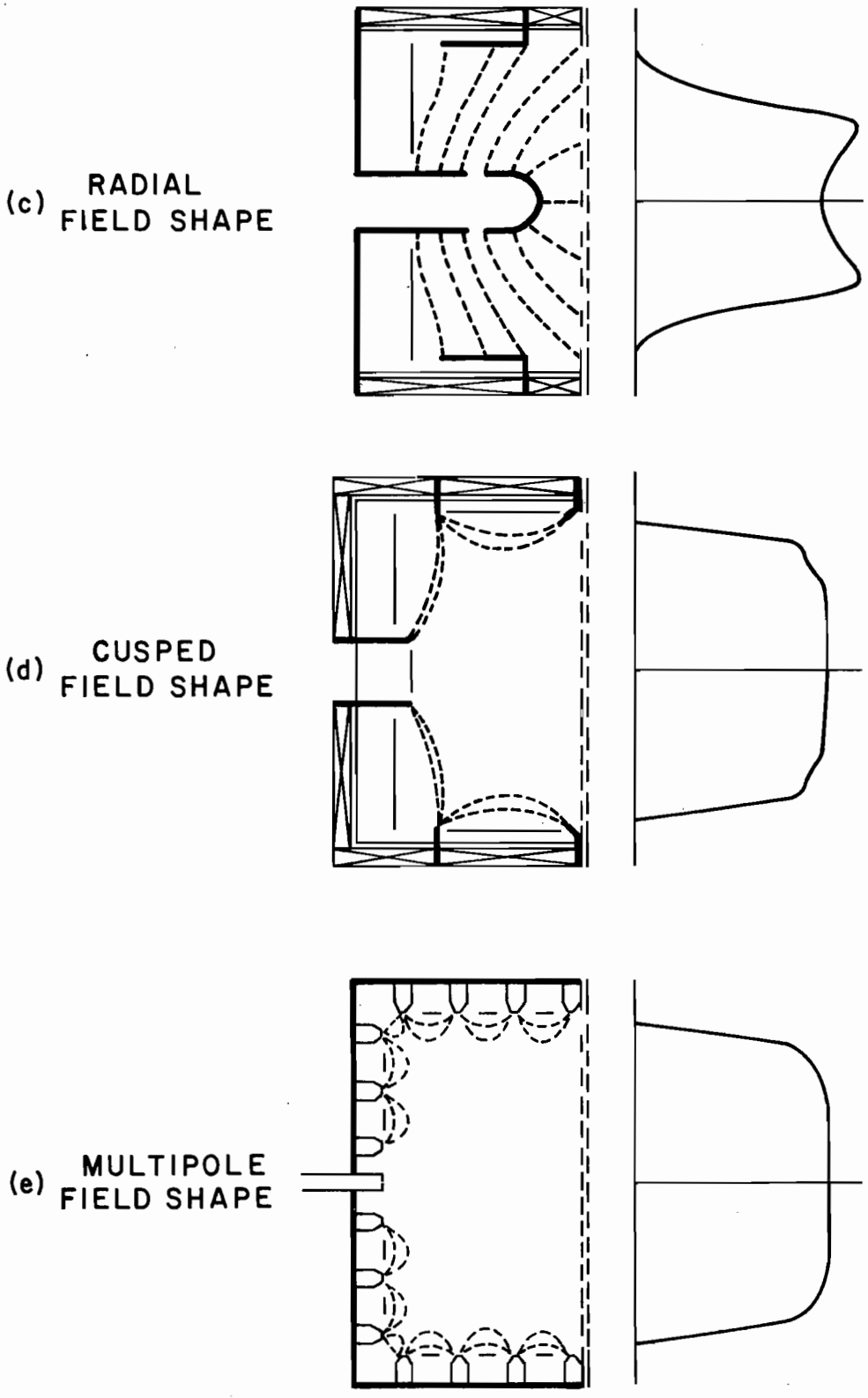

Figure 2. (concluded)

investigation was undertaken, this design had produced the most uniform ion beam profile reported in the literature.

The multipole design of Moore and Ramsey is shown in Figure 2 (e) and can be considered an adaption of the "picket fence" concept of plasma containment in fusion research. In this design a large number of permanent magnet pole pieces are located around the perimeter of the discharge chamber. They are arranged so that the magnetic polarity of adjacent pole pieces is opposite. The magnetic field is thus confined to a small region near the pole pieces, leaving a large region of uniform depth and negligible field strength throughout the remainder of the discharge chamber. This allows the energetic electrons to have direct access to almost the entire chamber. The 12 cm diameter multipole thruster operated by Ramsey on mercury propellant gave losses of 160 eV/ion at 90% utilization and a beam current of 0.325 A. The ion beam profile was not described by Ramsey, but it would be expected to be as uniform as any previously obtained with other designs. This expectation was realized in the results of this investigation where profiles of the shape indicated in Figure 2 (e) were obtained.

Cesium and mercury have been the propellants in most of these investigations. However, researchers have demonstrated that electron-bombardment thrusters can be operated on a variety of gases.[12-16] Argon and xenon have been the preferred gases for the reasons given earlier.

Thruster Design

As a result of the advancement of electron-bombardment ion source technology, a large number of applications have been proposed for these

devices. Typical types of applications are primary propulsion systems for deep space missions, auxiliary propulsion systems for station-keeping and altitude control of satellites, and the previously mentioned ground applications. Because of these widely different applications, it is not possible for one ion source to fulfill all of the requirements. Sources having diameters from 2.5 cm to 150 cm have, therefore, been designed, fabricated and operated. Development of a new ion source, however, has usually been very costly in terms of both time and hardware. This is primarily due to insufficient knowledge of the necessary design and scaling parameters. For example, the 15 cm diameter strongly divergent magnetic field design of Figure 2 (b) required a test program of over 100 configurations in optimizing the performance.[6] Subsequent scaling of this design to a 30 cm diameter size by simply doubling all of the dimensions resulted in significantly poorer performance thereby requiring an additional test program.[17] These problems are not unique to the strongly divergent magnetic field design as similar difficulties also arose in scaling the radial magnetic field design.[18] Scaling and performance correlations do exist,[7,19,20,21,22] but they have not eliminated the need for this trial-and-error approach.

Much of the testing involved in these programs is involved with the reshaping of the magnetic field. Since the spacing between pole pieces changes when a given design is scaled to a new size, the magnetic field also changes. This results in a field which differs in both magnitude and shape. Determination of the necessary field strength can be easily accomplished by use of electromagnets. The field shape, however, is controlled primarily by the shape and location of the pole pieces. Thus optimization of the field shape requires the testing

of many different pole pieces. Additional tests are required in the determination of the cathode location, discharge chamber length, and the mode of propellant injection. The results of these tests, though, are also dependent upon the shape and strength of the magnetic field. With the multipole design the pole piece spacing can remain constant over a wide range of thruster sizes, thus many of these problems would be expected to be eliminated.

Present Investigation

The objective of this investigation was to understand the operation and to determine the necessary design and scaling relationships for a low field strength multipole gas ion source. Although the entire discharge chamber is of interest, most of the interesting phenomena are found in the fringe-field regions above the anodes. For maximum utility, the scaling relationships should involve only overall ion source performance specifications, readily available propellant properties, and experimental results that can be obtained through bench testing. Such an approach would permit initial performance specifications to be rapidly translated into high performance prototypes.

II. APPARATUS

The two multipole thrusters used in this investigation are shown in Figure 3. These thrusters are conceptually related to both the cusped field design of Beattie[9] and the multipole design of Moore[10] and Ramsey.[11] Similarities with the cusped field thruster are that thin pole pieces of soft iron are used with electromagnets between adjacent pole pieces. The major difference from the cusped field thruster is that more and smaller pole pieces are used, giving a larger fraction of low-field-strength volume in the ion chamber. The major similarities to the Moore and Ramsey design are the large number of pole pieces used and the general ion-chamber shape. Moore and Ramsey, however, used permanent magnets as pole pieces, with the magnetization direction towards or away from the center of the discharge chamber. When permanent magnets are used in the designs studied herein, they replace the electromagnets between adjacent pole pieces rather than becoming the pole pieces. As an additional difference, Moore and Ramsey used much higher magnetic field strengths.

The first thruster used in this investigation is shown in Figure 3 (a) and is designated MP-I. The pole pieces are fabricated of 1.5 mm thick soft iron and are 2.5 cm deep. For the side walls they are flat with an internal diameter of 15 cm, while the upstream pole pieces are cylindrical with mean diameters of 5, 10, and 15 cm. A spacing of 2.5 cm was used for all adjacent pole pieces with 1.5 mm thick aluminum anodes located midway between each pair of pole pieces. The length of the ion chamber could be varied in 2.5 cm steps by adding or removing anodes and pole pieces.

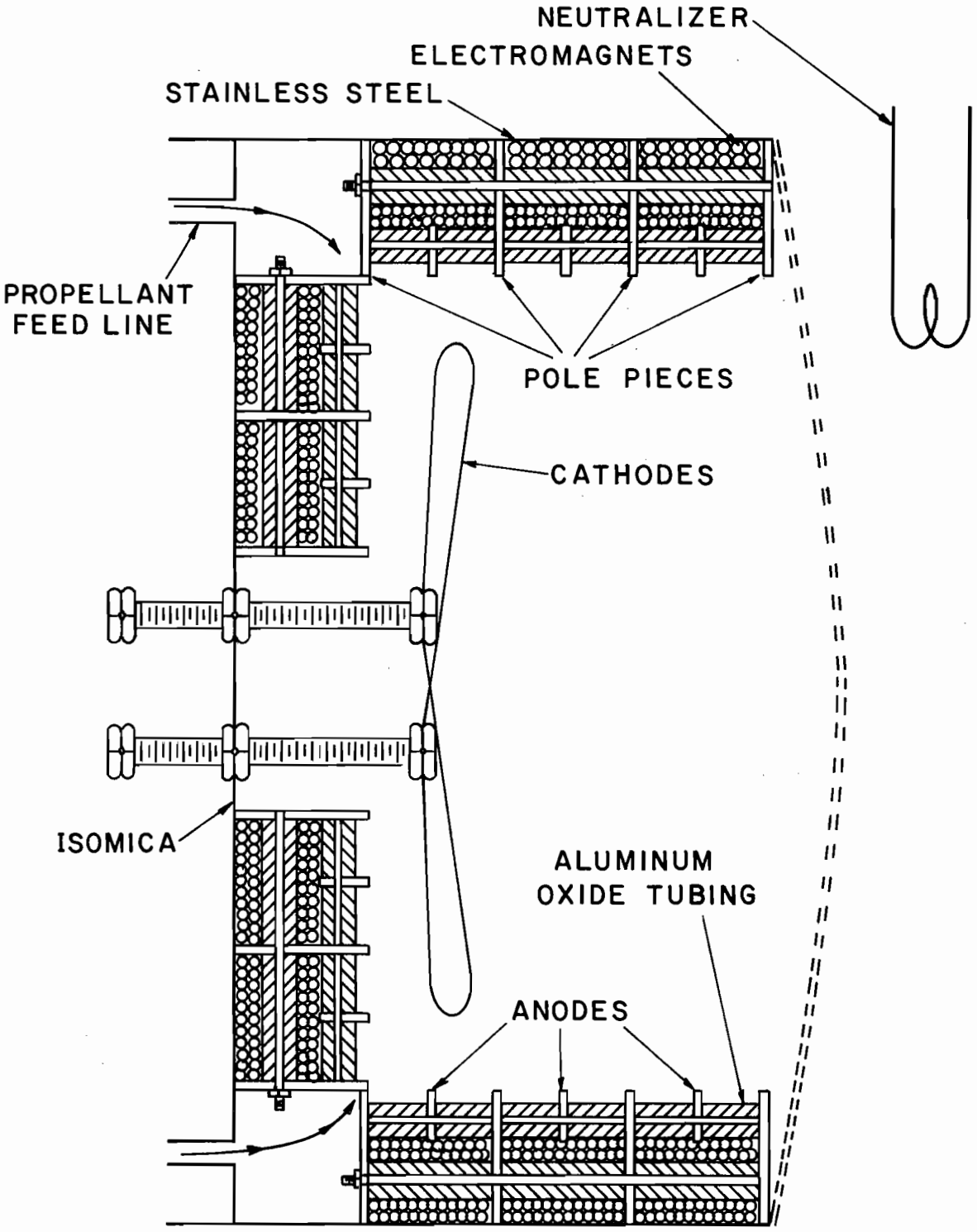

Figure 3 (a) MP-I

Sketch of 15-cm Multipole Gas Thruster.

The original magnetic configuration used four electromagnets between each adjacent pair of pole pieces. A modified magnetic field configuration was also used with eight electromagnets between each pair of pole pieces. The electromagnets in each section were positioned circumferentially in line with those in adjoining sections. All electromagnets in each configuration were connected in series, so that the current was the same through all windings.

Dished grids were used with a 67 percent open area screen and a 43 percent open area accelerator. The thickness of both grids was about 0.4 mm, while the center-to-center hole spacing within a grid was about 2.2 mm. The grids were assembled with a interelectrode spacing of about 1 mm and operated with +1000 and -500 volts.

Tungsten wire, 0.25 mm diameter, was used for both main and neutralizer cathodes. The main cathode consisted of 2 wires connected in parallel whereas the neutralizer was a single wire loop that extended 3-cm into the beam. The outer shell of the thruster was a tube, rolled from thin stainless steel. The backplate was Isomica. The propellant was introduced into the annular region formed by the two corner pole pieces, with several 6 mm holes through the pole pieces permitting flow radially inward into the ion chamber.

Due to saturation in the magnetic circuit, which will be discussed later, as well as thermal deterioration of the magnet windings and anodes, a second thruster was designed. This thruster, designated MP-II, is shown in Figure 3 (b). The pole pieces were again fabricated of 1.5 mm thick soft iron, with the exception of the 10 cm diameter upstream pole piece which was 3 mm thick. Note that intermediate side pole pieces were effectively 3 mm thick because they consisted of two

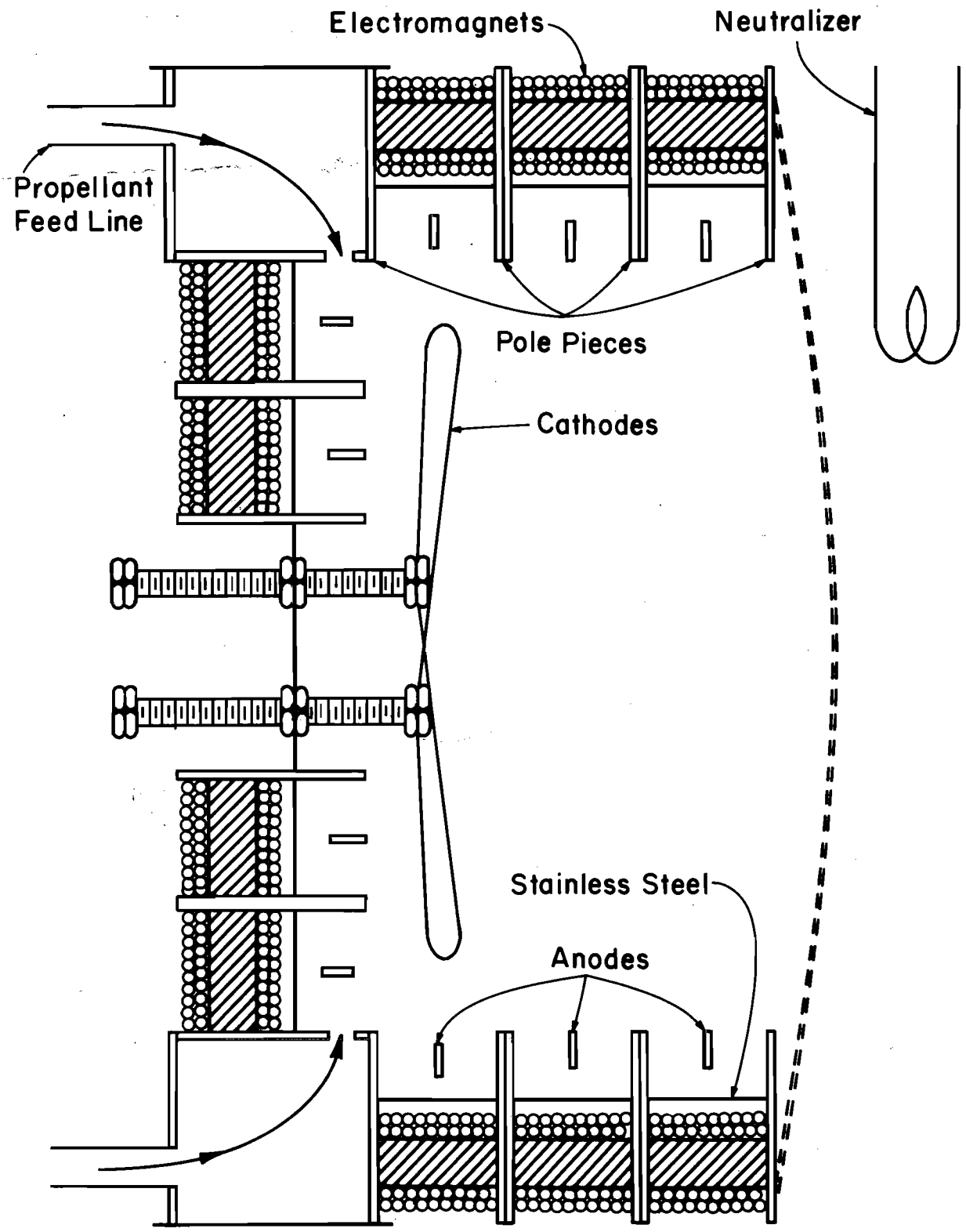

Figure 3 (b) MP-II

(Concluded.)

thicknesses of 1.5 mm thick soft iron. A center-to-center spacing of 2.7 cm was used for the pole pieces. The anodes in this design were constructed from 1.5 mm thick stainless steel and again were positioned midway between each pair of pole pieces. In order to protect the electromagnets from the hot discharge chamber environment, they were located outside the discharge chamber. This was accomplished by placing stainless-steel sealing rings between the anodes and the electromagnets. The upstream rings were flat and those on the side were cylindrical. Each side section, consisting of an anode, sealing ring, two pole pieces, and the electromagnets between the pole pieces, could be added or removed as a unit. This modular approach had two advantages. First, it doubled the pole piece thickness between two sections in order to prevent saturation problems and second, it allowed the discharge chamber length to be varied conveniently in 2.7 cm increments.

The disposition of electromagnets was twelve between each pair of side pole pieces, eight between the 10 and 15 cm diameter upstream pole pieces, and four between the 5 and 10 cm upstream pole pieces. The electromagnets in each section were positioned so that they were not circumferentially in line with electromagnets in adjoining sections. This was done to avoid the saturation problems that might have otherwise occurred. Again, all electromagents were connected in series.

Dished small hole accelerator grid (S.H.A.G.) optics were used, with a 67 percent open area screen and a 24 percent open area accelerator. The thickness of the screen and accelerator grids were 0.4 and 0.5 mm. The center-to-center hole spacing within each grid was about 2.2 mm and they were assembled with an interelectrode gap of about 1 mm.

All data presented were obtained at +1000 and -500 volts for screen and accelerator potentials respectively.

Tungsten wire, 0.25 mm diameter, was used for both the main and neutralizer cathodes. The neutralizer was the same as in MP-I, however, the number of main cathodes connected in parallel was increased from 2 to 4 in order to increase the emission capability. Propellant introduction was the same as in MP-I.

Propellant flow for both thrusters was controlled with an adjustable leak valve and measured with a mass flowmeter. The flowrate was maintained within ± 1 percent of the desired value while data was being obtained. A Faraday cup probe was installed 6.5 mm downstream of the center of the accelerator grid, which was installed convex side out for both thrusters. Details of the Faraday probe and associated electronics are given by Wilbur.[23] An $\vec{E} \times \vec{B}$ momentum analyzer was installed with the sensing probe 68 cm downstream of the accelerator grid. This probe was movable transverse to the ion beam, with the path of motion passing through the center of the ion beam. Details of the $\vec{E} \times \vec{B}$ sensing probe and its operation are given by Vahrenkamp,[24] with the method of analyzing the data given by Beattie.[25] A Langmuir probe, movable in two directions was used to obtain plasma data within the ion chamber. Details of the Langmuir probe system used are given by Wilbur.[23] The data was analyzed using the numerical procedure of Beattie.[25]

All testing was conducted in the 1.2 m diameter, 4.6 m long vacuum facility at the Engineering Research Center of Colorado State University. The pumping was accomplished by an 0.8 m diffusion pump together with a liquid-nitrogen cooled liner.

III. PROCEDURE

In order to determine the capabilities of this design, the thruster was operated over a wide range of conditions using both argon and xenon as propellants. Flow rates of approximately 400, 500, 900, and 1500 ma-equivalent were used with argon and of approximately 200, 400, and 600 ma-equivalent with xenon. Six discharge chamber lengths were examined and ranged from 2.7 cm to 16.2 cm in 2.7 cm increments.

After the initial startup, the thruster was operated for about 30 minutes before taking data. This allowed both the thruster and the thermal flowmeter to warm up and stabilize. Following this warm up period, the propellant flow rate was adjusted to obtain the desired flow ± 1 percent. This was accomplished by monitoring the output of the flowmeter on a digital voltmeter and adjusting the flow to the desired value ± 0.02 volts. If the flow varied beyond this range, data acquisition was suspended until the flow was brought back within the desired range. Once the proper flow rate had been obtained, data were recorded. Those data included magnet current, discharge current, discharge voltage, accelerator current, and beam current. Appropriate probe currents and voltages were also included for Langmuir probe surveys within the discharge chambers, Faraday probe surveys of the ion beam, or $\vec{E} \times \vec{B}$ momentum analyzer measurements.

In addition, the effect of varying the magnetic field strength and of shorting various anodes to body potential was also examined. These data were not obtained for each operating condition. Magnetic field strength data were typically obtained at the first operating condition following startup to insure that subsequent operation would be at the

optimum magnetic field strength. The anode configuration data were obtained only at 50 volts discharge voltage for argon and 45 volts discharge voltage for xenon at each flow rate.

All propellant utilizations presented herein were corrected for double ionization and propellant backflow. The propellant backflow was calculated from facility pressure and the free-molecular-flow conductance of the accelerator system. The double ionization correction was calculated using the surveys of the $\vec{E} \times \vec{B}$ momentum analyzer. The numerical corrections obtained for double ionization are shown in the appendix.

IV. THEORY

Pertinent theory for the multipole discharge chamber includes the containment of primary electrons, diffusion of Maxwellian electrons to the anodes, and the escape of neutrals through the accelerator system. The more important theory elements in these areas are described below.

Primary Electron Containment

The primary electrons should be contained within the ion chamber so that they expend most of their energy in producing ions before being lost to the anodes. The fringe magnetic field between adjacent pole pieces should therefore be sufficiently high to prevent primary electrons from reaching an anode without an intermediate collision. In order to help determine the optimum magnetic field, a simple model was developed. An iron filing map of the magnetic field within the discharge chamber is shown in Figure 4. As shown, it consists of a relatively strong magnetic field existing only near the boundary with the majority of the chamber being essentially field free. To approximate the field of Figure 4, a magnetic field of uniform strength was assumed to exist over a limited distance above each anode, as shown in Figure 5 (a). Beyond the uniform field region, the field strength was assumed to fall to zero. Picking the direction of motion for a primary electron such that it has the deepest penetration into this fringe field, it is evident from Figure 5 (a) that this corresponds to two cyclotron radii. The cyclotron radius is defined as

$$r_c = \frac{mv}{qB} \tag{1}$$

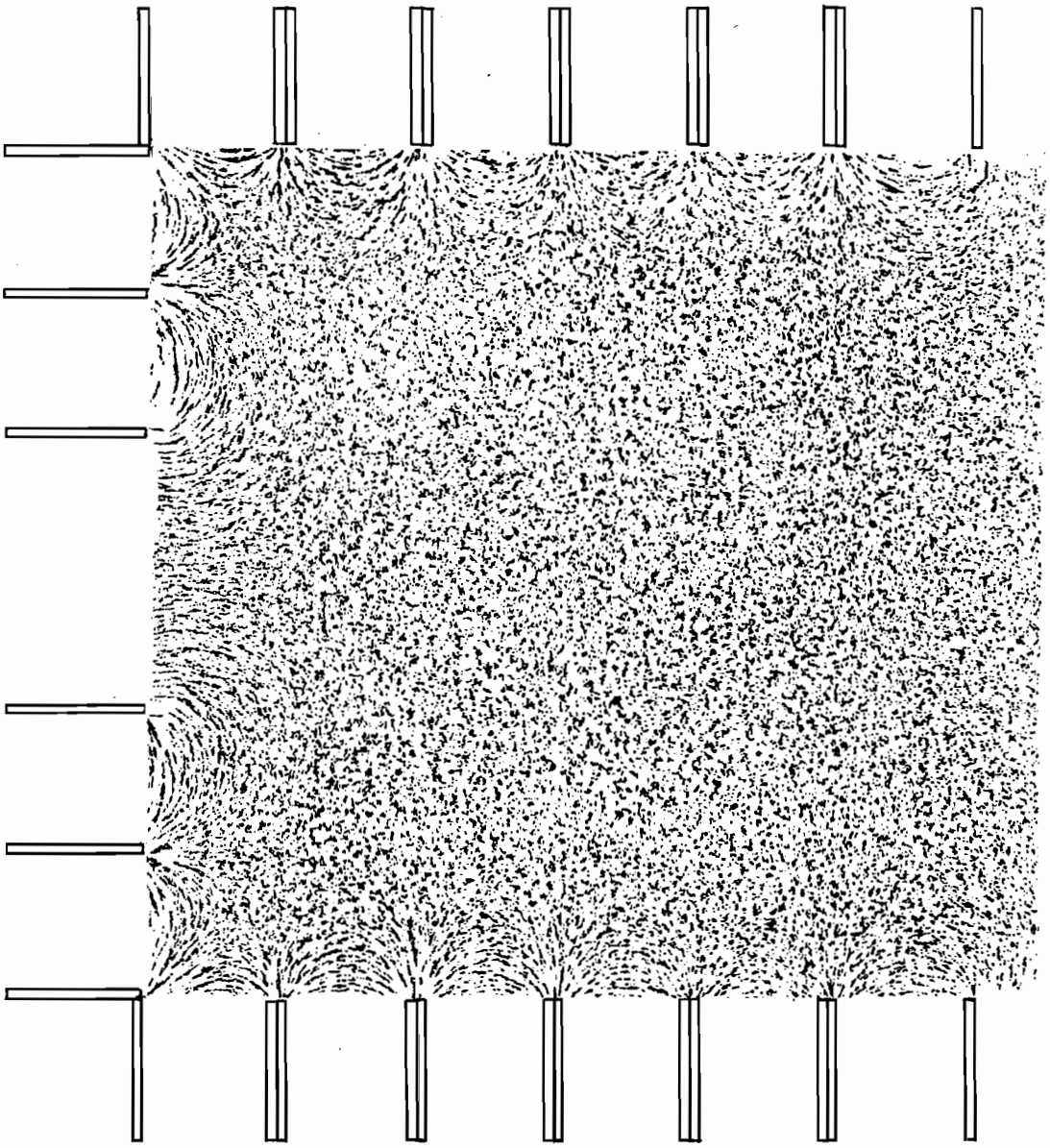

Figure 4. Iron filing magnetic-field map.

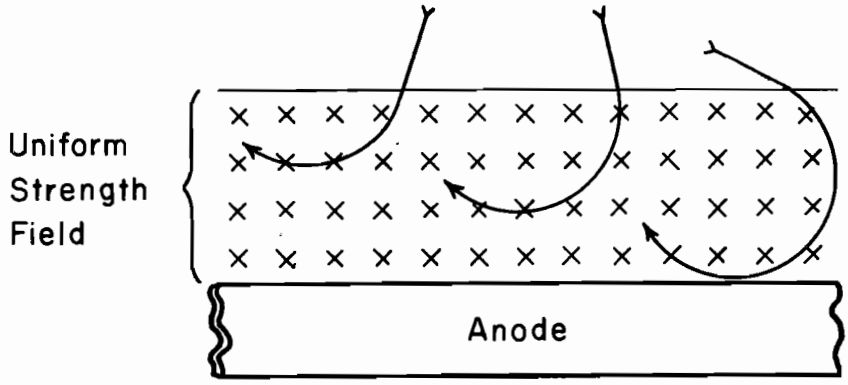

(a) Simplified Deflection Configuration

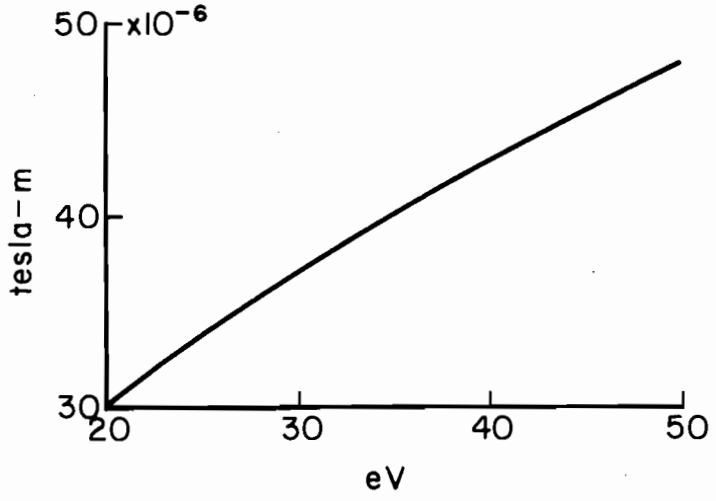

(b) Required Flux per Unit Anode Length as a Function of Electron Energy

Figure 5. Electron interaction with fringe magnetic field above anode.

where r_c = cyclotron radius

m = mass of the particle

v = velocity of the particle

q = electronic charge of the particle

B = magnetic induction.

For a primary electron, the equation can be rewritten in terms of electron energy (in eV) in the form

$$r_c = 3.37 \times 10^{-6} \frac{\sqrt{eV}}{B} \qquad (2)$$

This can be further rewritten as

$$2\, r_c B = 6.74 \times 10^{-6} \sqrt{eV} \qquad (3)$$

where $2\, r_c$ is the depth of the fringe field above the anode, and B is the magnetic induction of this field. The product of $2\, r_c B$ can therefore be thought of as the number of flux lines per unit anode length. The distribution of these flux lines is not important. For example, half the magnetic induction extending twice as far from the anode would have the same effectiveness in deflecting primary electrons. This conclusion was also shown to be valid by Robinson and Kaufman[26] for the more realistic case of field strength varying with distance from anode. The required flux per unit anode length is shown in Figure 5 (b). For comparison of units, 50×10^{-6} tesla-m equals 50 gauss-cm.

Maxwellian Electron Diffusion

Electrons are emitted into, and ions extracted out of the discharge chamber plasma. For equilibrium operation, these currents must be

balanced by a Maxwellian electron current out of the plasma to the anodes. However, in order to reach the anodes, the Maxwellian electrons must diffuse across the magnetic field. Figure 4 indicates that for the multipole design, the magnetic field decreases rapidly with distance from the anode. Therefore, the diffusion process occurs only over a small region near the boundary.

The equation of motion for electrons diffusing across the magnetic field as a result of both voltage and density gradients is given by Chen[27] as

$$v_e = \frac{q}{m_e \nu} \frac{dV}{dr} - \frac{qT_e}{n_e m_e \nu} \frac{dn_e}{dr} \tag{4}$$

where v_e = Maxwellian electron drift velocity.

q = electronic charge

ν = collision frequency

m_e = electron mass

n_e = Maxwellian electron number density

T_e = Maxwellian electron temperature in eV

$\frac{dV}{dr}$ = radial potential gradient

$\frac{dn_e}{dr}$ = radial density gradient

The coefficients of the voltage and density gradient terms are the mobility and the diffusion coefficients respectively:

$$\mu = \frac{q}{m\nu} \quad \text{Mobility} \tag{5}$$

$$D = \frac{qT_e}{m\nu} \quad \text{Diffusion} \tag{6}$$

They are related by the Einstein relation:

$$\mu = \frac{D}{T_e} \tag{7}$$

Using these relations, the resulting electron current density can be written as

$$j_e = qn_e v_e = \frac{qn_e D}{T_e} \frac{dV}{dr} - q D \frac{dn_e}{dr} \tag{8}$$

Finally, the predicted anode current can be determined by multiplying this current density by the appropriate collection area.

Early theoretical studies of electron diffusion used the classical approach in which the plasma within the magnetic field is assumed to be free of any collective behavior, or turbulence. The diffusion of electrons is then entirely due to electron-atom and coulomb collisions. In this case, the collision frequencies for the different collision processes are added together to obtain the total collision frequency. This value is then used in Equation (6) to obtain the "laminar" diffusion coefficient. However, diffusion coefficients obtained in this manner have often been found to be inadequate. This discrepancy is due to the plasma within the magnetic field region being turbulent rather than laminar as assumed.[28,29]

The presence of turbulence was deduced from the anomalously high diffusion rates obtained experimentally, compared to the classical predictions. The first, and best known, approach toward obtaining an effective turbulent diffusion coefficient is the empirical expression given by Bohm,[28]

$$D = \frac{10^4 T_e}{B} \tag{9}$$

and in subsequent publications as, [27,30]

$$D = \frac{10^4 T_e}{16 B} \tag{10}$$

where B is the magnetic field strength. Although this relationship has not been given a successful mathematical treatment, it has been verified in an extensive series of experiments.[27]

A theoretical approach has been presented by Kaufman.[29] This method uses two-stream instability and a simple derivation to predict turbulent diffusion rates. This theory assumes the plasma to be of uniform density and uniform electron temperature. Then for small electric fields, the plasma will correspond to the laminar case since the current density in Equation (8) would vary linearly with the electric field. As the magnetic field is increased to give more efficient use of the ionizing electrons, the electric field will also increase due to the increased resistivity and thus the drift velocity in Equation (4) will also increase. When the drift velocity exceeds a critical value, instabilities will be amplified into plasma waves of finite amplitude. These waves will deflect electrons thereby increasing the collision frequency and resulting in increased diffusion. Since the magnetic field strength is empirically selected to give efficient operation, some degree of turbulence would be expected in most thruster designs.

These conclusions are supported by the experimental discharge-chamber results obtained by Domitz[31] where plasma noise, or instability, was determined as a function of magnetic field strength. At low field strengths, less than about 25 gauss for a 7.5 cm chamber diameter, little or no noise was observed, which corresponds to the laminar case. However, ion production costs (power required to produce an ion) were

quite high. As the magnetic field was increased and ion production became more efficient, there was a significant increase in the amount of noise present indicating the onset of turbulence. However, this increase in efficiency with magnetic field would not be expected to continue indefinitely since the associated increase in resistivity will reduce electron diffusion.

The highest magnetic fields used recently in a thruster were by Moore[10] and Ramsey[11] in a high field strength multipole design. In this design the field strength was apparently high enough to greatly inhibit electron diffusion to the anodes. A plasma anode (an anode surface unprotected by a magnetic field) was, in fact, required to maintain the discharge with this greatly reduced diffusion. This would suggest that this thruster was operating beyond the onset of turbulence.

Neutral Loss

There is a discharge-chamber pressure at which the most efficient production of ions occurs. This pressure, together with the accelerator system configuration, can be used to determine the neutral loss rate. A complete description of this neutral-loss theory is presented in Reference 32 with only a brief summary presented herein.

The density of primary electrons increases with discharge current.[8] Therefore, for a maximum-utilization condition at high discharge current, ion production can be approximated by considering only primary electrons. The total ion production rate $\dot{N}$ from primary electrons is then

$$\dot{N} = n_p v_p n_o \sigma \forall_p \tag{11}$$

where n_p = primary electron density

v_p = primary electron velocity

n_o = neutral density

σ = ionization cross section

$\forall_p$ = volume of primary electron region.

The total loss rate of ions from this region is

$$\dot{N} = n_i v_i A_p \tag{12}$$

where n_i = ion density

v_i = ion velocity

A_p = area of primary electron region

Equating the loss and production rates and solving for the neutral density gives

$$n_o = \frac{(n_i/n_p)(v_i/v_p)}{\sigma(\forall_p/A_p)} \tag{13}$$

Assuming a limiting condition where all electrons are primary electrons, plasma neutrality then requires $n_p = n_i$. Using the minimum ion velocity from the Bohm criterion gives

$$v_i = v_p \sqrt{m_e/2m_i} \tag{14}$$

where m_e = electron mass

m_i = ion mass.

Thus Equation (13) can be rewritten as

$$n_o = \frac{\sqrt{m_e/2m_i}}{\sigma(\forall_p/A_p)} \quad . \tag{15}$$

All of the parameters in Equation (15) are constants, giving a constant value for neutral density or discharge-chamber pressure, at maximum

utilization. This constant pressure upstream of the accelerator system implies a constant neutral-loss rate at maximum utilization regardless of the total mass flow. Thus, maximum utilization will increase with increasing flow rate.

The neutral-loss rate $\dot{N}_o$ can be obtained by combining Equation (15) with an effective sharp-edged orifice area A_o for the accelerator system and the average magnitude of the neutral velocity $\bar{v}_o$.

$$\bar{v}_o = \sqrt{8kT/\pi m_o} \quad . \tag{16}$$

where T = wall temperature

m_o = neutral mass.

The wall temperature should be roughly the same for all ion chambers, thus

$$\dot{N}_o = K n_o A_o / m_o^{\frac{1}{2}} \tag{17}$$

Where K includes all constants that are not a function of the ion source configuration or the propellant. Substituting for n_o from Equation (15) gives

$$\dot{N}_o = \frac{K\, A_o \sqrt{m_e/2m_i}}{m_0^{\frac{1}{2}}\, \sigma\, (\forall_p/A_p)} \tag{18}$$

Assuming $m_o = m_i$ and then redefining K gives

$$\dot{N}_o = \frac{K\, A_o}{m_i\, \sigma\, (\forall_p/A_p)} \tag{19}$$

Solving for K,

$$K = \dot{N}_o\, m_i\, \sigma\, (\forall_p/A_p)/A_o \tag{20}$$

Thus the product $\dot{N}_o\, m_i\, \sigma\, (\forall_p/A_p)/A_o$, referred to as the neutral-loss parameter, should be nearly constant for all ion chambers. This was verified by the experimental results presented in Reference 32.

A wider range of chamber lengths was to be included in this investigation than in any recent study of discharge-chamber performance. Also, more than one propellant was to be used. The possibility of correlating performance for different lengths and propellants was therefore examined. The value of the neutral-loss parameter used in correlating the maximum utilization, or "knee", performance[32] made it a promising candidate for a more general performance correlation over a wide range of utilizations. The neutral-loss rate $\dot{N}_o$ can be rewritten as $I_o(1-\eta_u)$ where I_o is the total neutral flow rate in amperes-equivalent and η_u is the propellant utilization. Thus the neutral-loss parameter becomes $I_o(1-\eta_u)m_i\, \sigma\, (\forall_p/A_p)/A_o$ which allows correlation over the entire range of utilization rather than just at the maximum value.

For a discharge-loss parameter, some means of compensating for changes in wall area (and associated wall losses) was also required. The simplest approach would be to multiply experimental discharge losses (eV/ion), by the ratio of beam area to primary electron area, A_b/A_p. The beam area A_b is the same for all chamber lengths. However, the primary electron area A_p (and associated ion losses to the walls) will increase with increasing chamber length. Therefore, the ratio A_b/A_p will decrease, and the discharge losses will increase, with increasing chamber length. The distribution of actual losses is more complicated, but the use of this simple area ratio might be expected to give a first-order correction and therefore, it will be used.

V. EXPERIMENTAL RESULTS AND DISCUSSION

Experimental performance was measured and compared to the theory described in the preceding section. This comparison established the criterion for primary electron containment. It also indicated that the plasma is turbulent within the fringe field, so that use of this criterion would not result in excessive containment for Maxwellian electrons. The design approach developed was verified in an independent investigation in which a 30-cm diameter ion source was designed, fabricated, and tested. Finally, the correlation parameters given in the theory section were used to generalize performance for a wide range of discharge chamber configurations.

Primary Electron Considerations

As previously indicated, there is an optimum magnetic field for primary electron containment. Experimental results obtained for the determination of this field for the MP-I design using argon propellant are shown in Figure 6. Discharge losses continuously decrease with increasing magnetic field with near minimum values being obtained at about 8×10^{-3} tesla.

Additional tests were conducted using various anode configurations. The configurations were:

(1) All anodes at anode potential (all anodes, or original configuration);

(2) The anodes adjacent to the upstream corner pole pieces at cathode potential, all others at anode potential (corner out configuration);

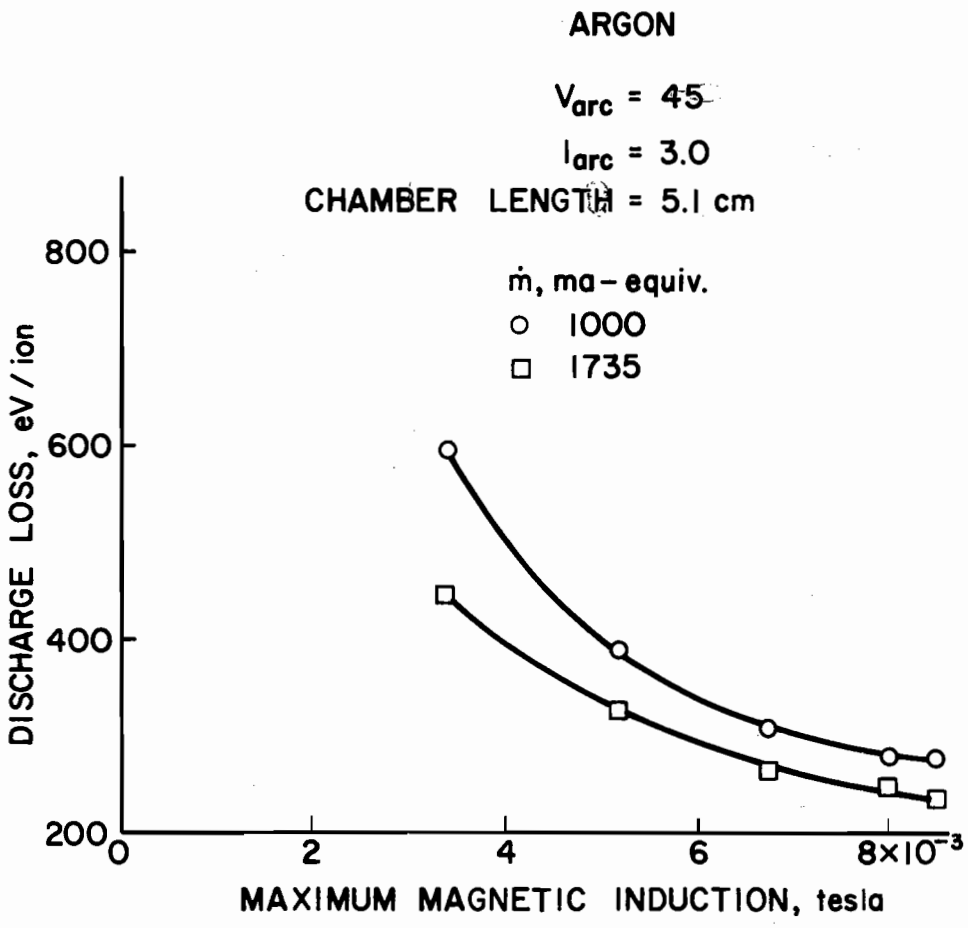

Figure 6. Variation of discharge loss with magnetic field for MP-I.

(3) The anodes adjacent to the upstream corner pole pieces at anode potential, all others at cathode potential (corner only configuration);

The results of these tests are given in Figure 7. With low magnet currents, performance is degraded in going from the all anodes configuration to the corner only configuration, but is improved for the corner out configuration. The corner only configuration would not operate at magnet currents above 6 amperes, but resulted in the highest losses where operation was possible. The all anodes and corner out configurations, however, converge to yield nearly the same performance at magnet currents of 8 to 10 amperes, which corresponds to a magnetic field of 6×10^{-3} to 8×10^{-3} tesla. Similar results obtained with xenon are given in Figure 8.

The improved performance at low magnet currents for the corner out configuration was an unexpected result. To explain this apparent discrepancy, detailed magnetic-field measurements were made. Values were obtained in the plane of each anode from a point midway (both radially and axially) between adjacent pole pieces inward until the field was negligible. Results obtained with a magnet current of 10 amperes are shown in Figure 9 for both a side and corner location. The side location is defined as a pair of adjacent pole pieces that are not at either end of the chamber and is typical of most of the ion chamber. Note that the 10 ampere magnet current corresponds to low discharge losses in Figures 7, 8 and 9. Integration of this field over distance normal to the anode,

$$\int_{\text{anode}}^{\infty} B d\ell \qquad (21)$$

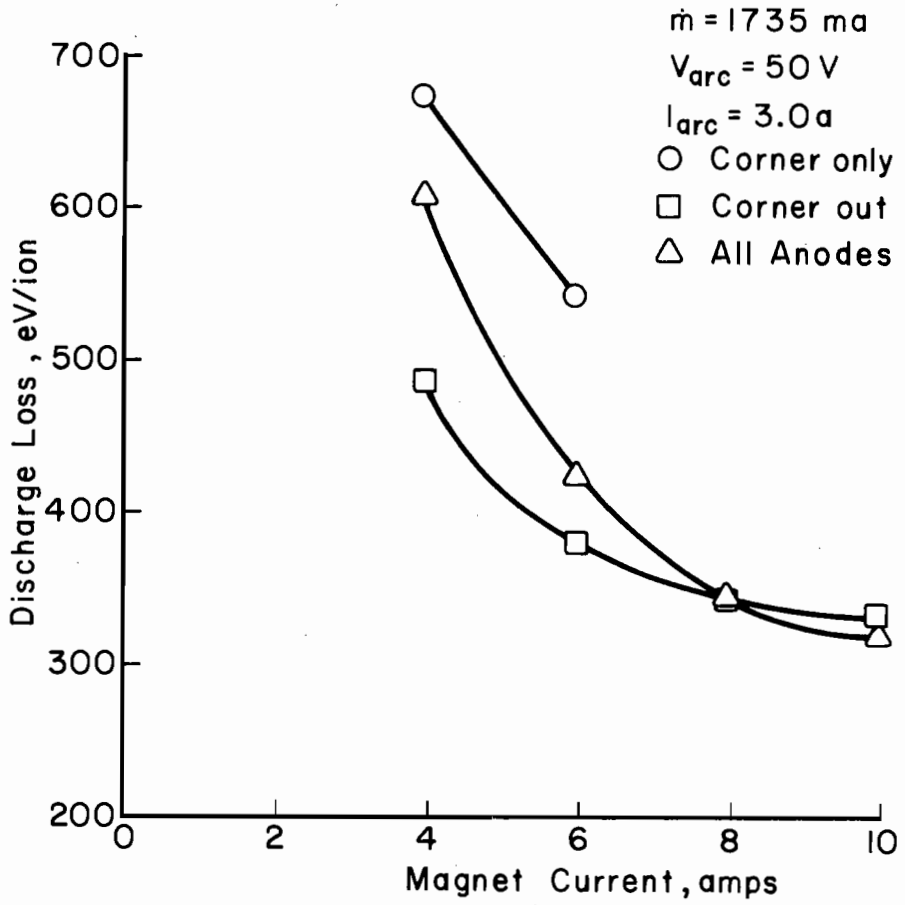

Figure 7. Variation of discharge loss with magnet current for different anode configurations with argon propellant.

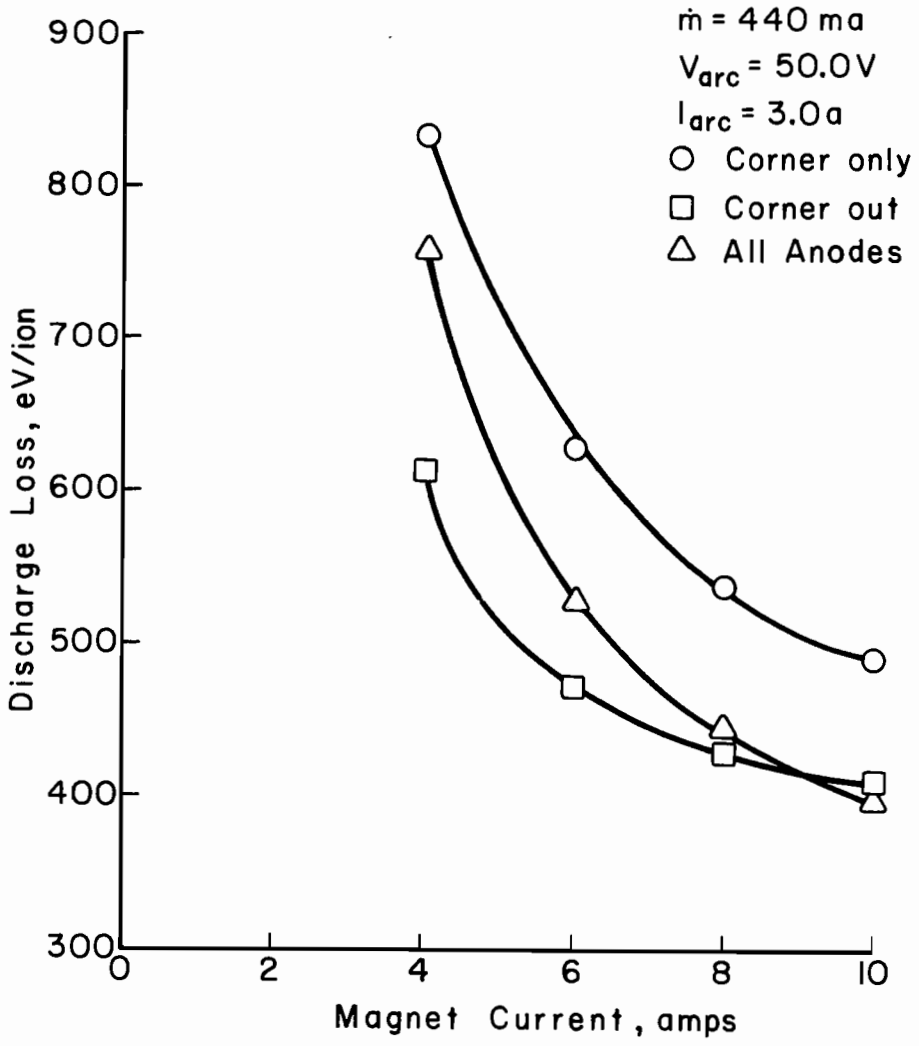

Figure 8. Variation of discharge losses with magnet current for different anode configurations with xenon propellant.

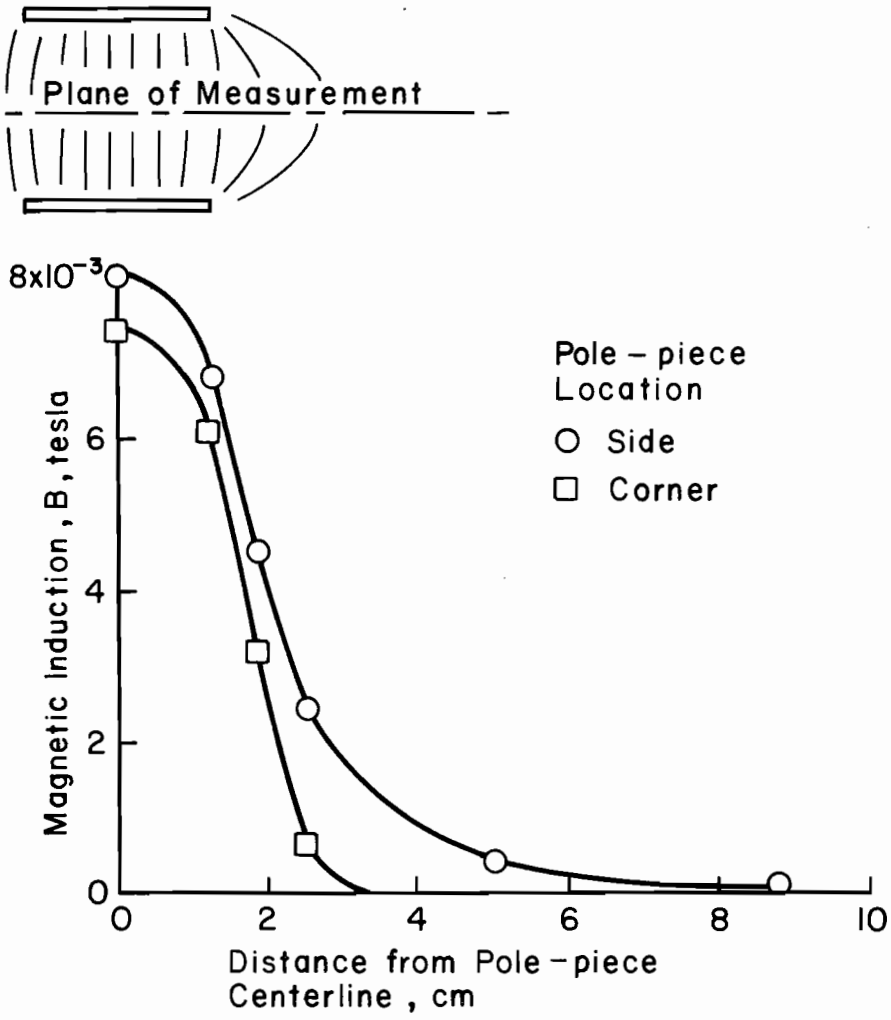

Figure 9. Magnetic field between pole pieces of MP-I.

yields the flux per unit anode length. The upper limit of ∞ would apply to a pair of isolated pole pieces. In an ion chamber, the intergration is carried to the first point of negligible magnetic field. For the side pole piece location, numerical integration yielded about 88 x 10^{-6} tesla-meters. From Figure 5 (b), 45 x 10^{-6} tesla-meters should have been sufficient to prevent the 50 eV primary electrons present within the chamber from reaching the anode. An examination of fringe fields at different anode locations showed the weakest field was in the corner location. The corner field, also shown in Figure 9, integrated to 42 x 10^{-6} tesla-meters at this same 10 ampere condition. Comparison of these two integrated values with the theoretical value from Figure 5 (b) suggests that the escape of primary electrons is controlled by the corner fringe field. This conclusion is supported by both the improved performance at low magnet currents in the corner out configuration and by the experimental observation that the corner aluminum anode was more likely to warp during operation.

This phenomena of the most current being collected in the region where the electrons have to cross the least number of field lines has also been observed in other thruster designs. In a study of a mildly divergent field design by Reader,[5] only the downstream end of the anode was found to be necessary for operation. For the cusped field design reported by Beattie,[9] about 99 percent of the current to the upstream anode was collected by the inner edge of this electrode. Also, for the strongly divergent field design examined by Harbour, et al.,[22] about 94 percent of the current to the anode was collected by the downstream end. In each case, the high current regions correspond to those having the minimum number of field lines for the electrons to cross.

Because of the inability of this design to show a definite optimum magnetic field strength as well as the problems with thermal deterioration of the magnet windings and warping of the aluminum anodes, a new thruster was designed. To obtain a uniform integrated fringe field throughout the thruster, the corner anodes would be recessed (behind the edges of the pole pieces) to provide the required magnetic field integral. The magnetic field was measured in the plane of the anodes for the new thruster with results similar to those shown in Figure 9 for MP-I. The amount of recess required was then determined by moving the lower limit of integration back between the pole pieces until the field integral at the corner equalled that at the side. This was found to occur at a point 2.5 mm behind the edge of the pole pieces, or about 10 percent of the pole piece spacing.

The variation in discharge loss with magnet current is shown in Figure 10 for both argon and xenon in the new thruster, MP-II. For both propellants, the discharge loss decreases rapidly as the magnet current is increased to about 4 amperes and then decreases slowly with further increases in magnet current. Numerical integration of the fringe field at 4 amperes, using data similar to that of Figure 9, yielded about 54 x 10^{-6} tesla-meters. This is in good agreement with the previously predicted value of 45 x 10^{-6} tesla-meters. However, because discharge losses were slightly lower at higher magnet currents and because minimizing these losses was one of the objectives, a magnet current of 8 amperes was used for all further tests. Numerical integration of the fringe field at 8 amperes resulted in about 100 x 10^{-6} tesla-meters. These results indicate that the use of the criterion given in Figure 5 for determining the required fringe field will

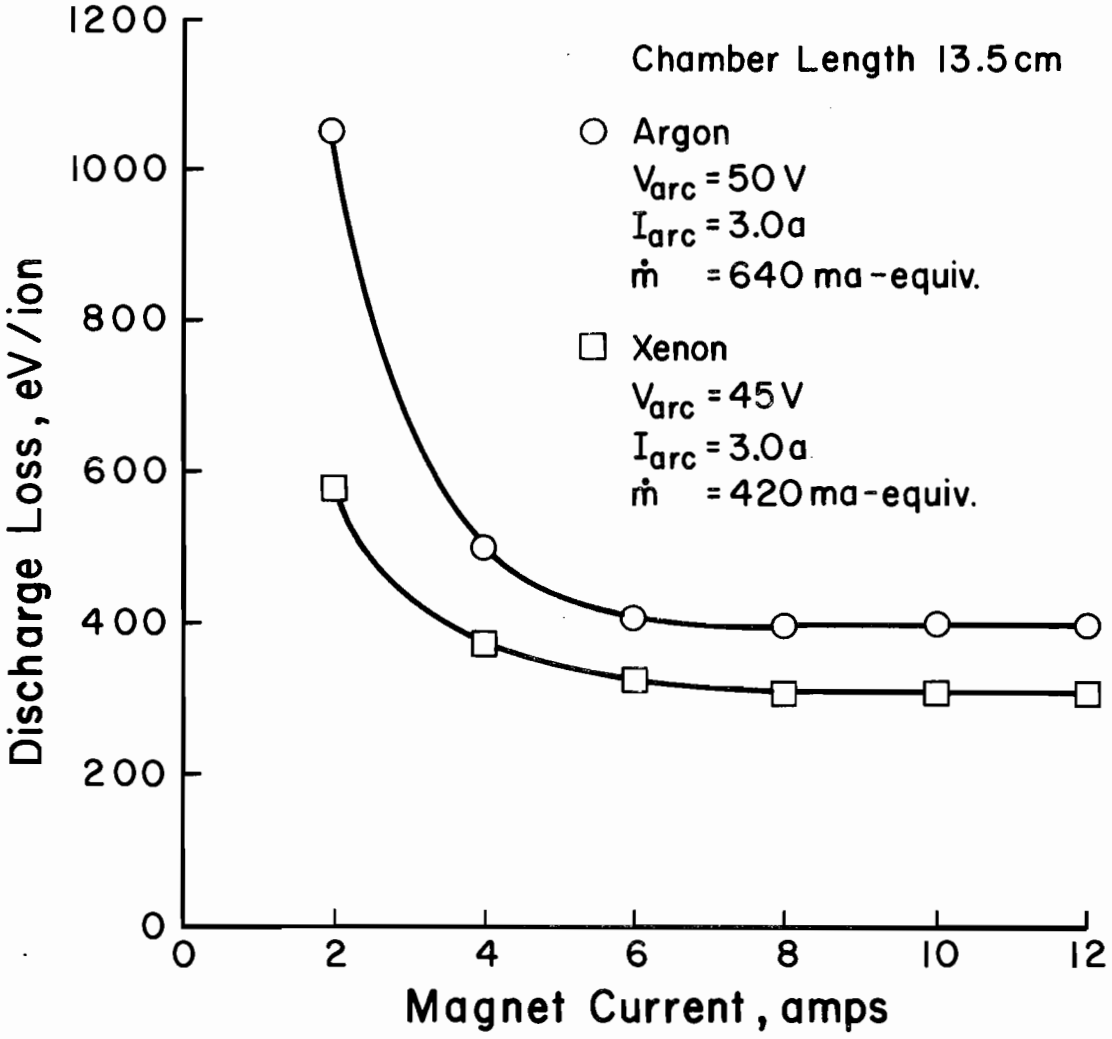

Figure 10. Variation of discharge loss with magnet current for MP-II.

produce a design that will have near minimum discharge losses. This level of performance would be acceptable for designs used in ground applications, however, for space applications where maximum optimization of performance is necessary, a value 1½ to 2 times the predicted value should be used.

The distribution of current per unit anode length to the anodes of MP-II is shown in Figure 11 for both propellants. With the exception of the number 1 anode, the distribution is fairly uniform. This uniformity can be considered to be an independent check on the amount of recess used for the corner anodes. The higher values obtained for the number 1 anode are attributed to the fact that this anode is located immediately upstream from the cathode. Thus, electrons are injected directly into the fringe field in front of this anode resulting in a higher current.

Typical ion chamber performance obtained at an electromagnet current of 8 amperes is shown in Figure 12 for argon and Figure 13 for xenon. As with the MP-I design, operation was not possible at this magnet current in the corner only configuration with argon propellant. For both propellants, there is now a definite improvement in performance for the "all anodes" configuration compared to the other configurations. Because of the good performance and overall uniformity of current to the anodes as well as the ability to increase the magnetic field to an optimum, the MP-II design was used for all further testing.

Plasma Properties and Phenomena

Plasma properties within the ion chamber were obtained using a movable Langmuir probe. Data obtained with the 8.1 cm MP-II chamber

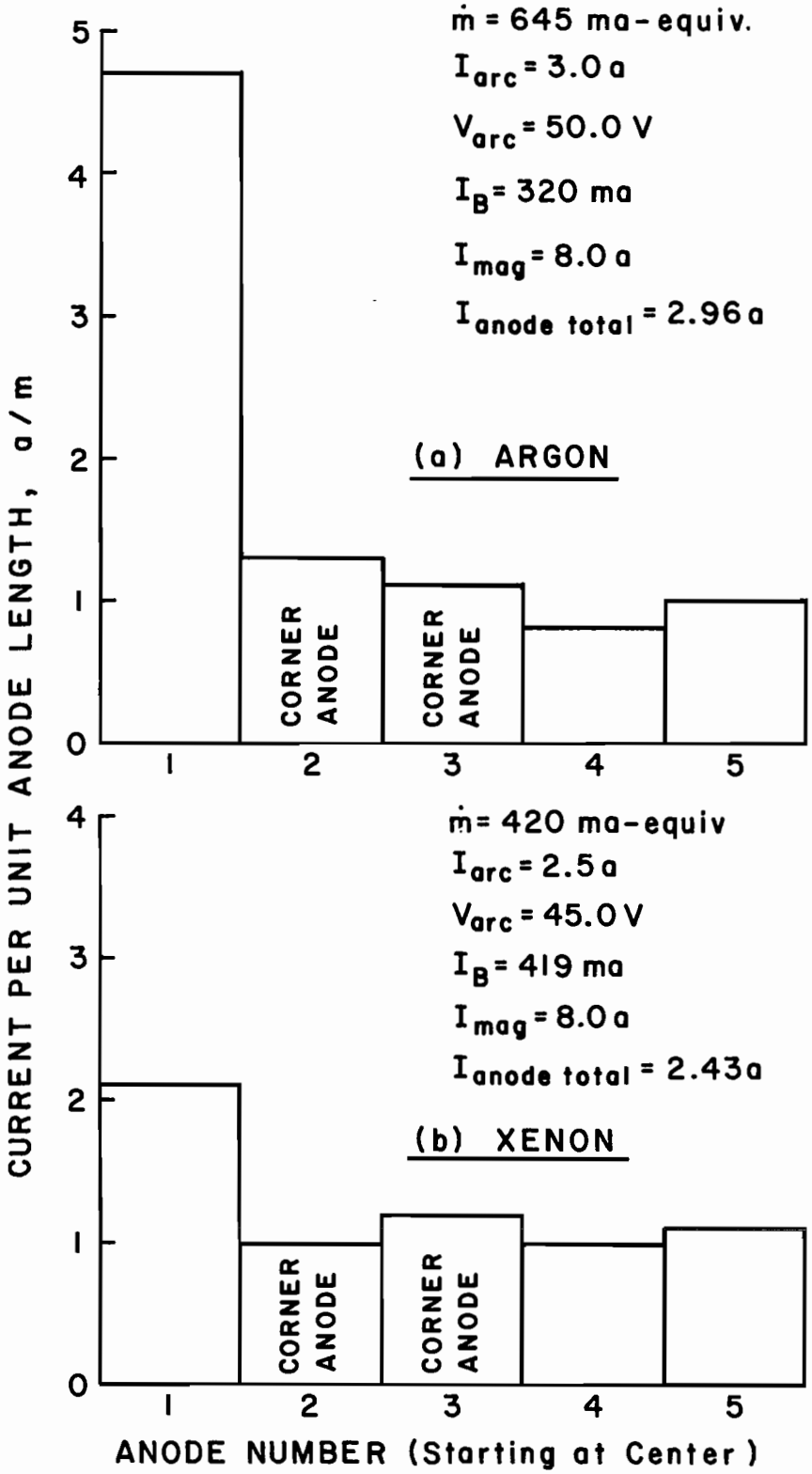

Figure 11. Anode distribution of discharge current per unit anode length.

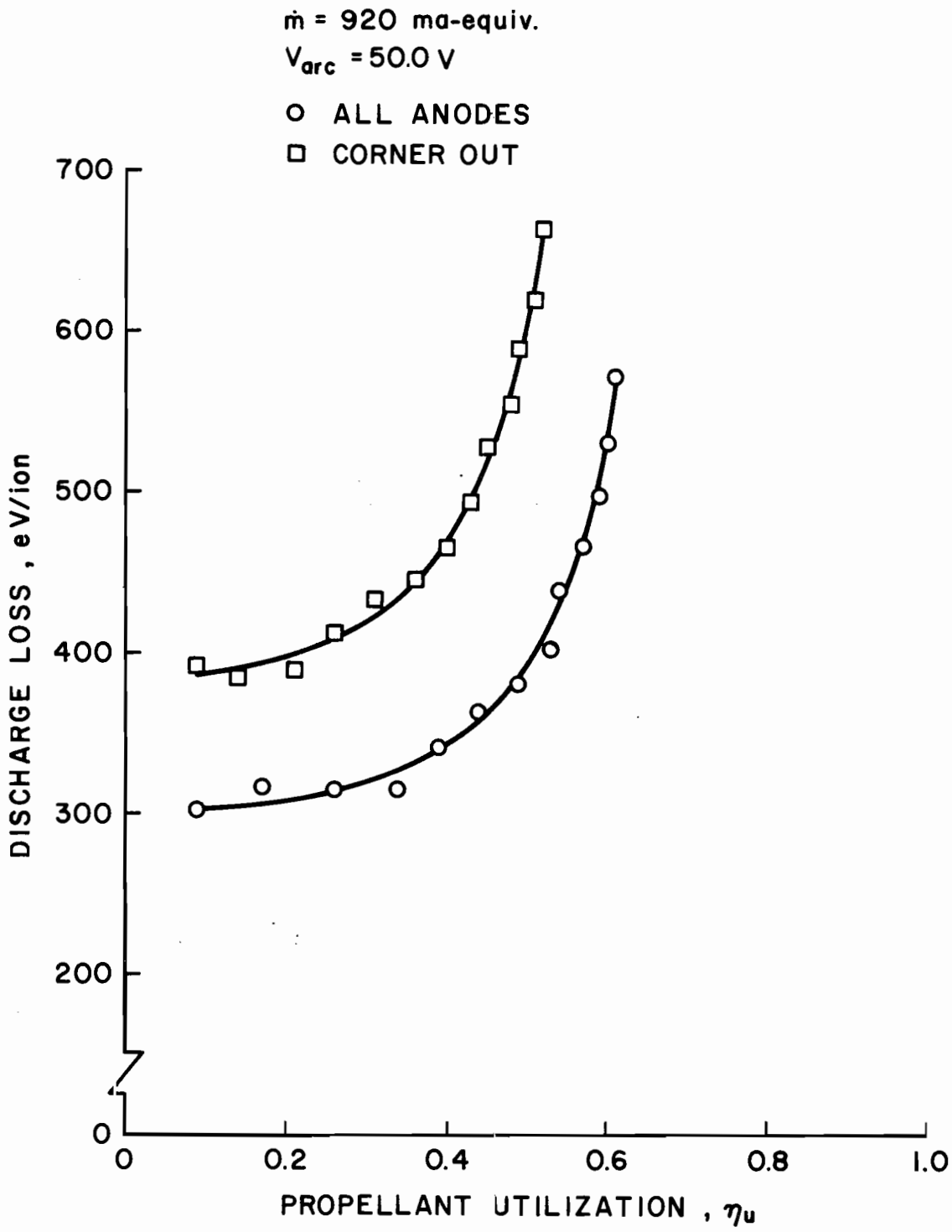

Figure 12. Effect of anode configuration on discharge-chamber performance with argon propellant for MP-II.

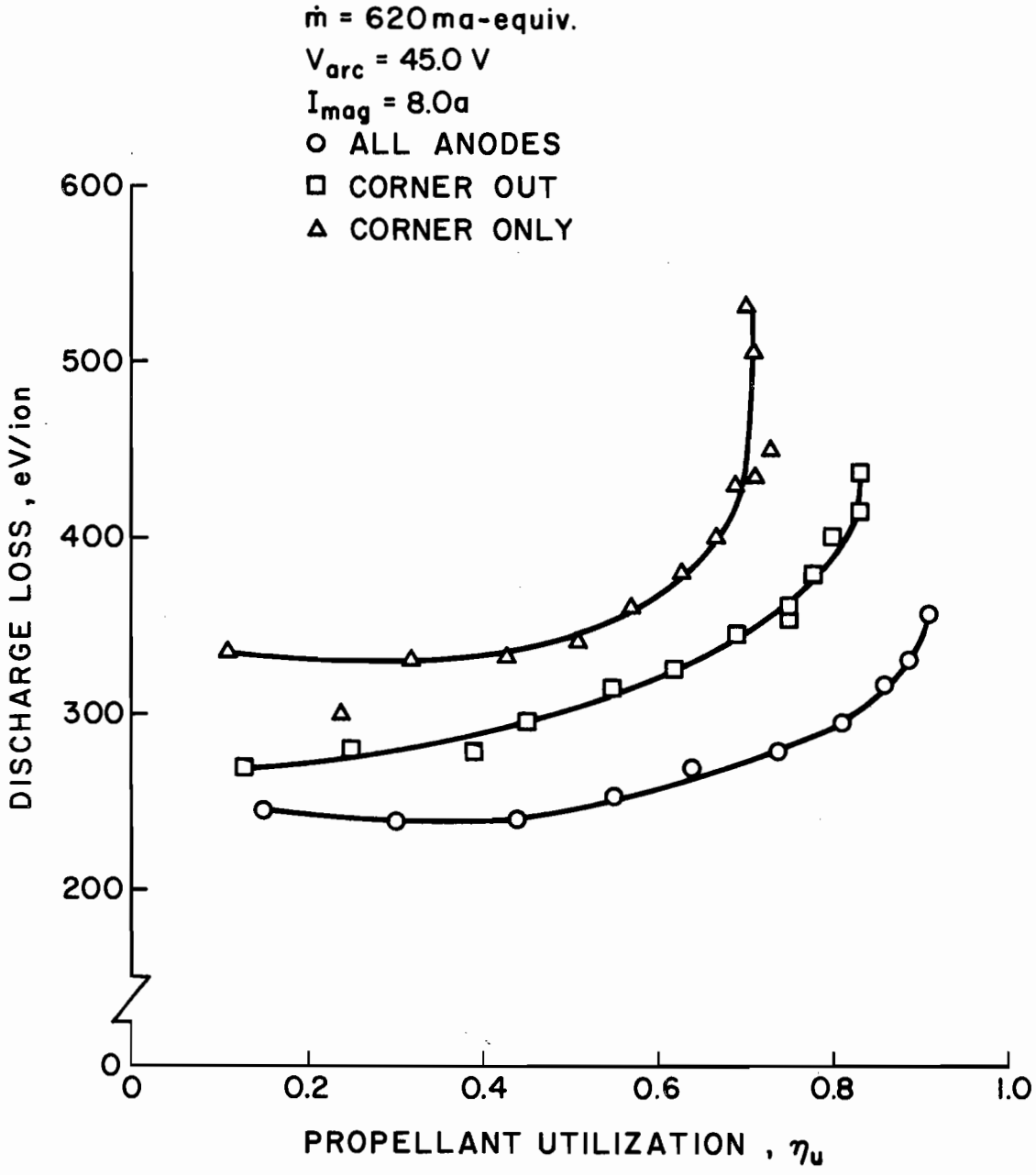

Figure 13. Effect of anode configuration on discharge-chamber performance with xenon propellant for MP-II.

are presented for both argon, Figure 14, and xenon, Figure 15. Plasma potential, Maxwellian temperature and Maxwellian and primary densities are shown for both propellants. The locations of the various pole pieces and anodes are also indicated. The cathode and its support occupied the open region at the upstream end of the chamber opposite the screen.

For both argon and xenon, plasma potential is very uniform throughout the chamber at a value slightly above the anode potential. Some of the nonuniformity observed in the remaining properties is felt to be a result of the analysis procedure rather than actual variations in the plasma. The overall trends indicated, such as decreasing values near the boundary, are, however, felt to be valid.

The effect of anode width on electron diffusion was examined. The 1.5 mm wide anodes (narrow anodes) shown in Figure 3 (b) were replaced with 12.5 mm wide ones (wide anodes). This width is equal to one half the pole piece spacing. Results obtained are presented in Figure 16 for argon, and Figure 17 for xenon. The results show that the narrow anodes do not adversely affect the diffusion of electrons. The diffusion parallel to the magnetic field is apparently rapid enough so that the anode width is not critical. The slight decrease in performance with wide anodes is probably due to the wider section cutting more flux lines, thus resulting in fewer flux lines that the electrons must cross to reach the anode. Because of these results, all subsequent testing was conducted using the original 1.5 mm wide anodes.

Experimental performance was also compared to the theory described in Chapter 4. The predicted electron current to the anodes was calculated for both Bohm diffusion (Equations 8 and 10) and turbulent

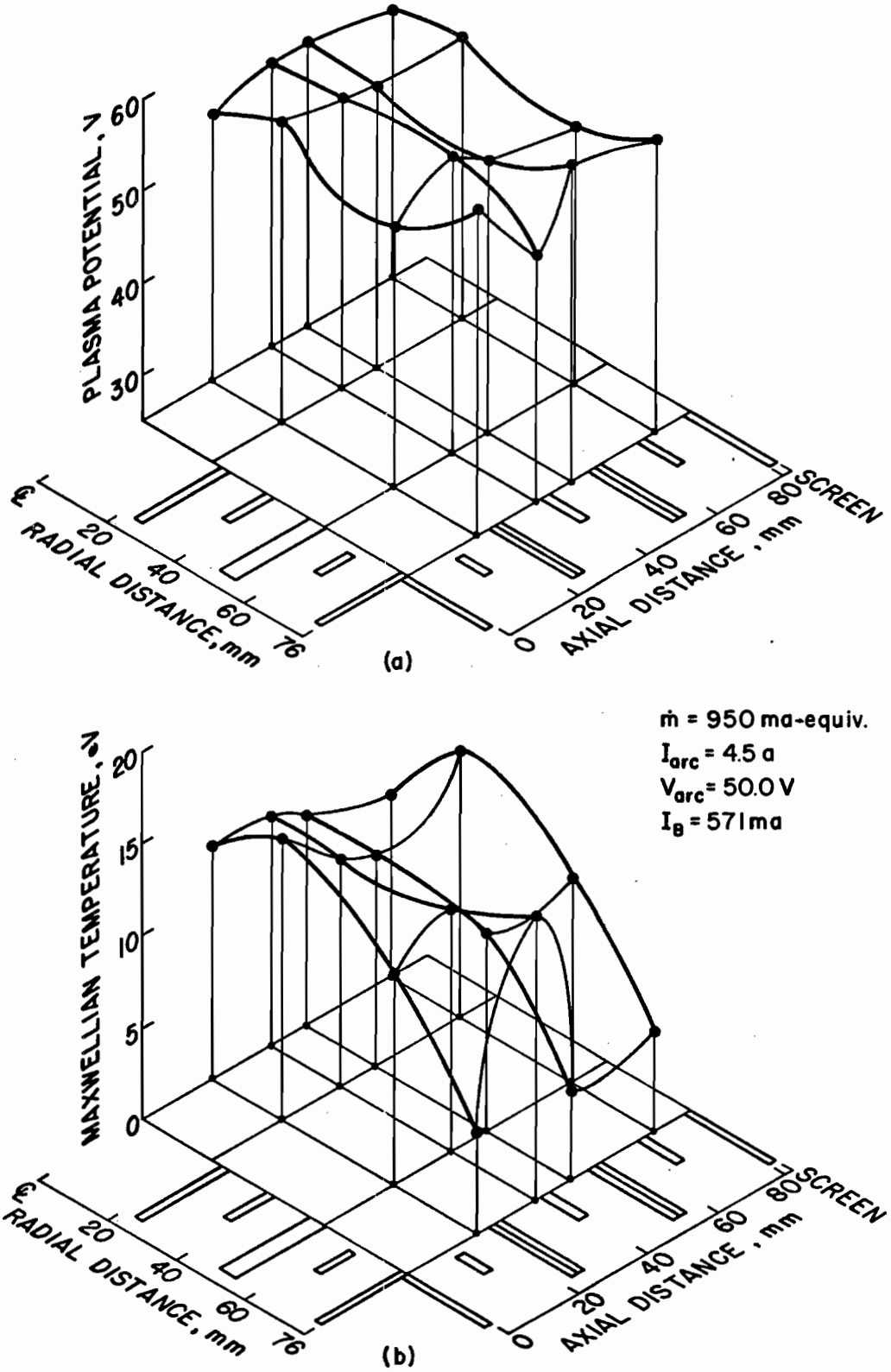

Figure 14. Plasma properties for 8.1 cm chamber length with argon propellant.

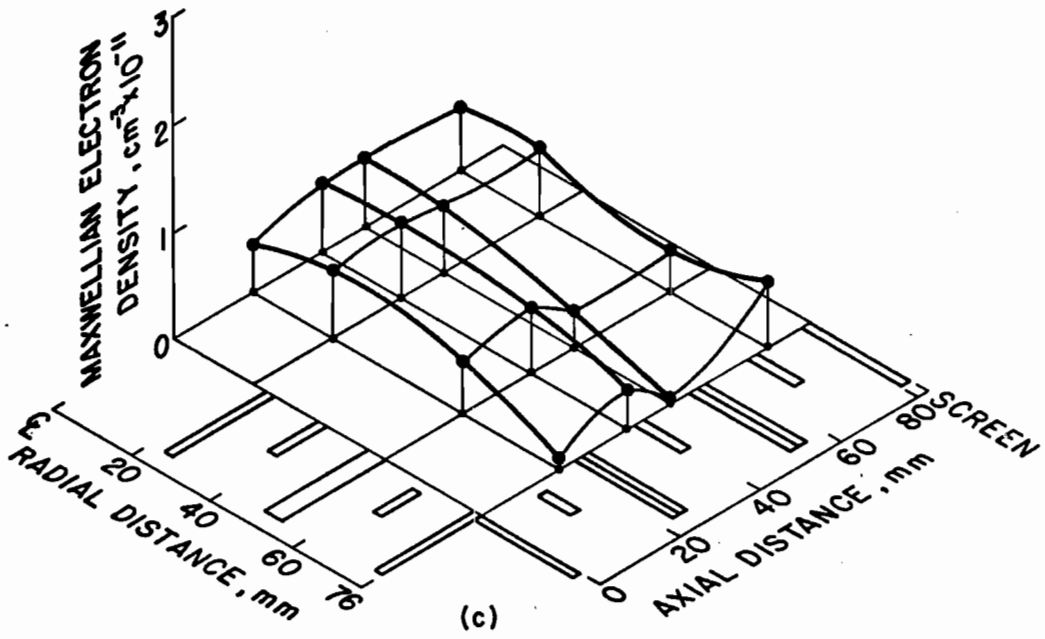

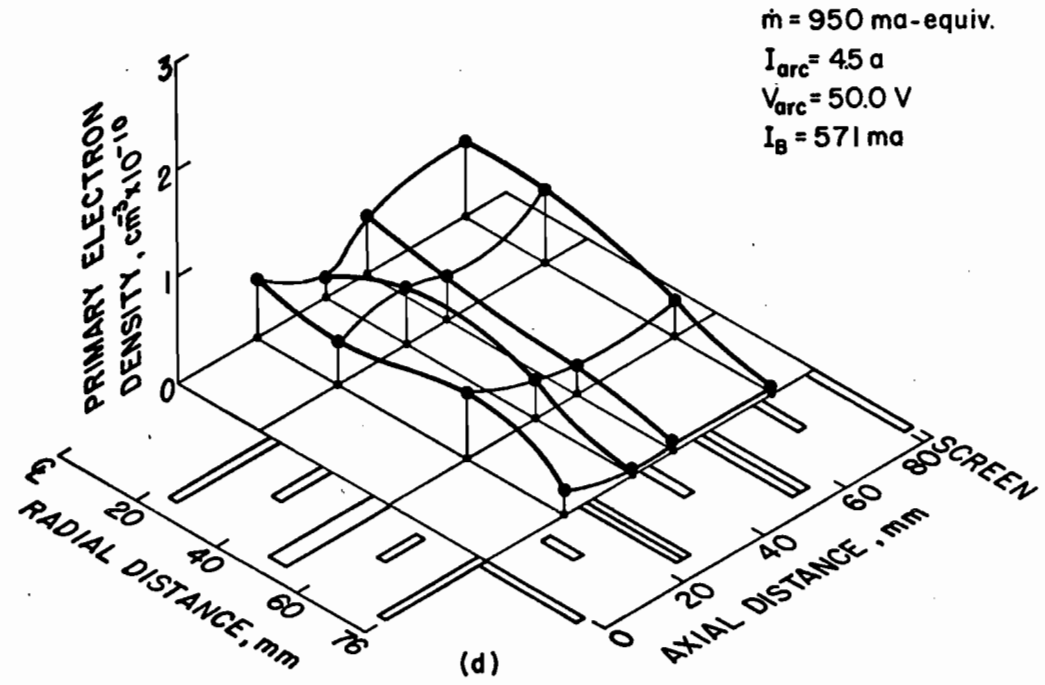

Figure 14. Concluded.

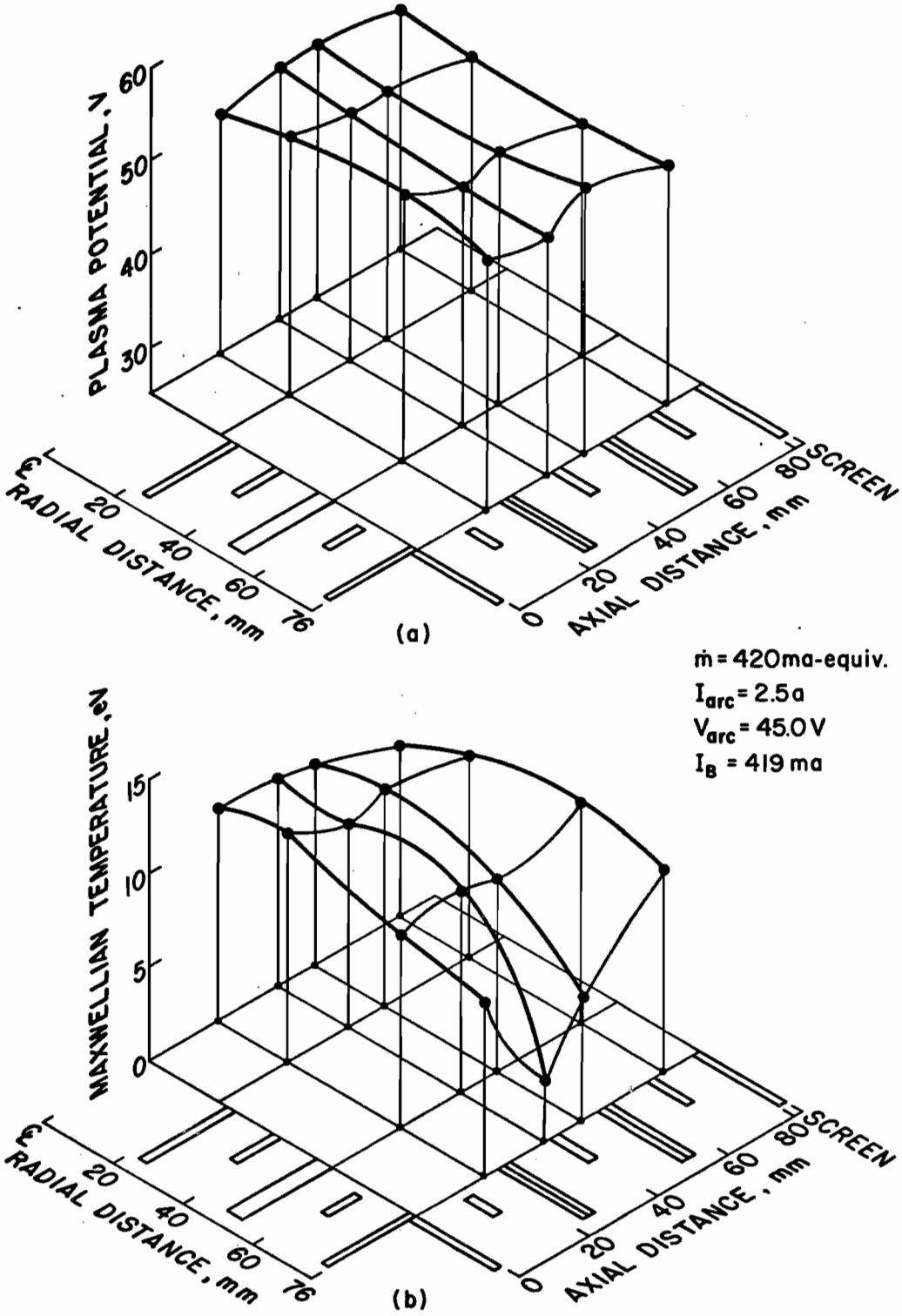

Figure 15. Plasma properties for 8.1 cm chamber length with xenon propellant.

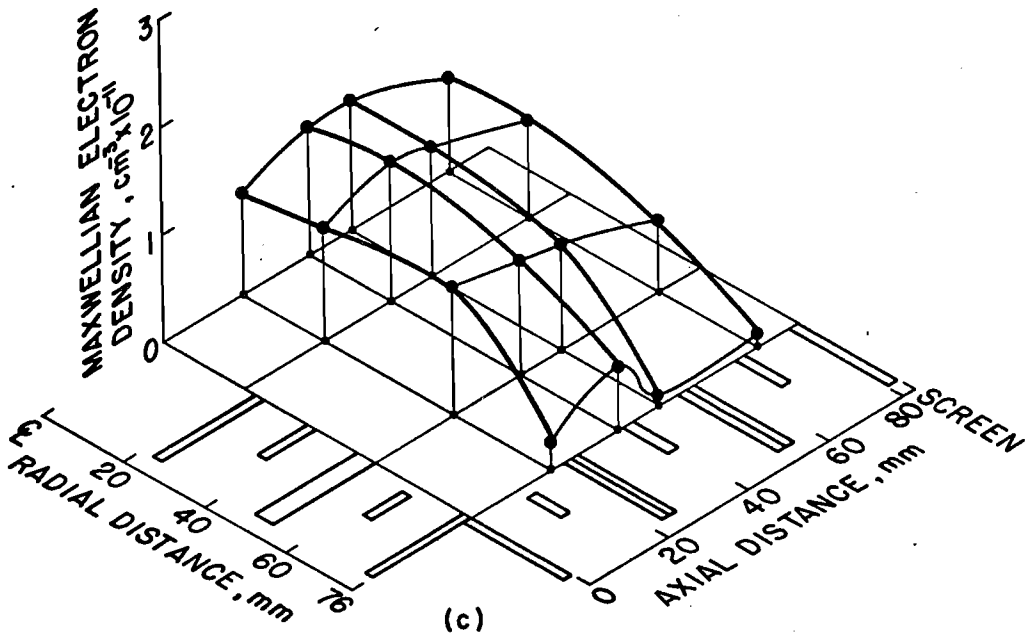

(c)

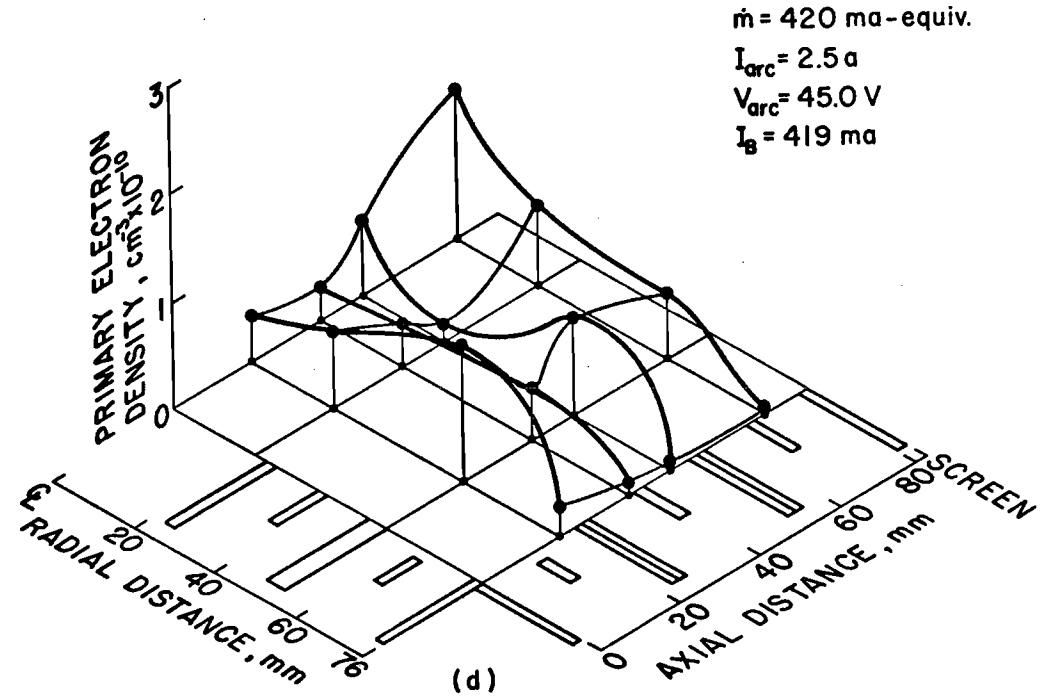

(d)

Figure 15. Concluded.

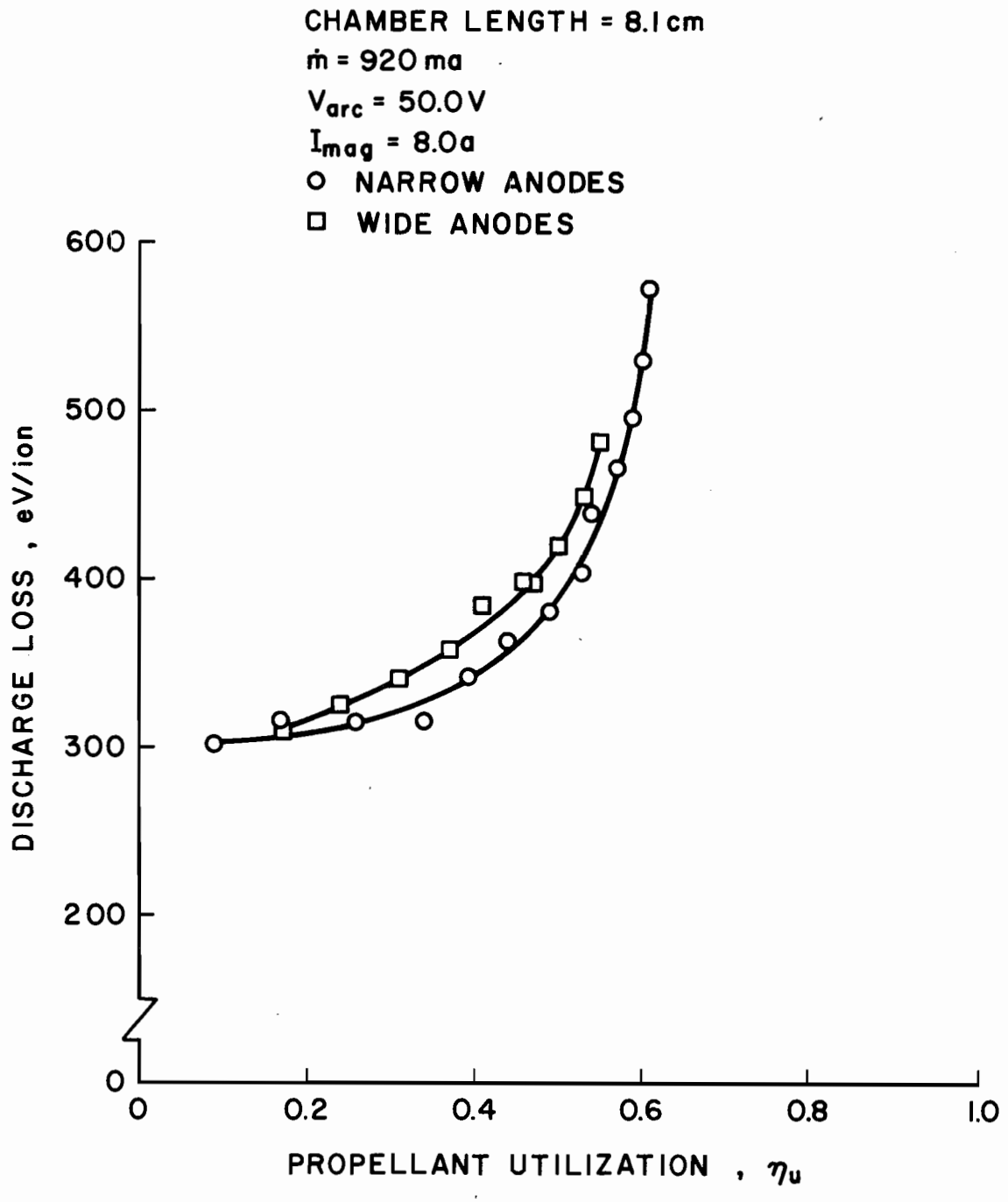

Figure 16. Variation of discharge-chamber performance for different anode widths with argon propellant.

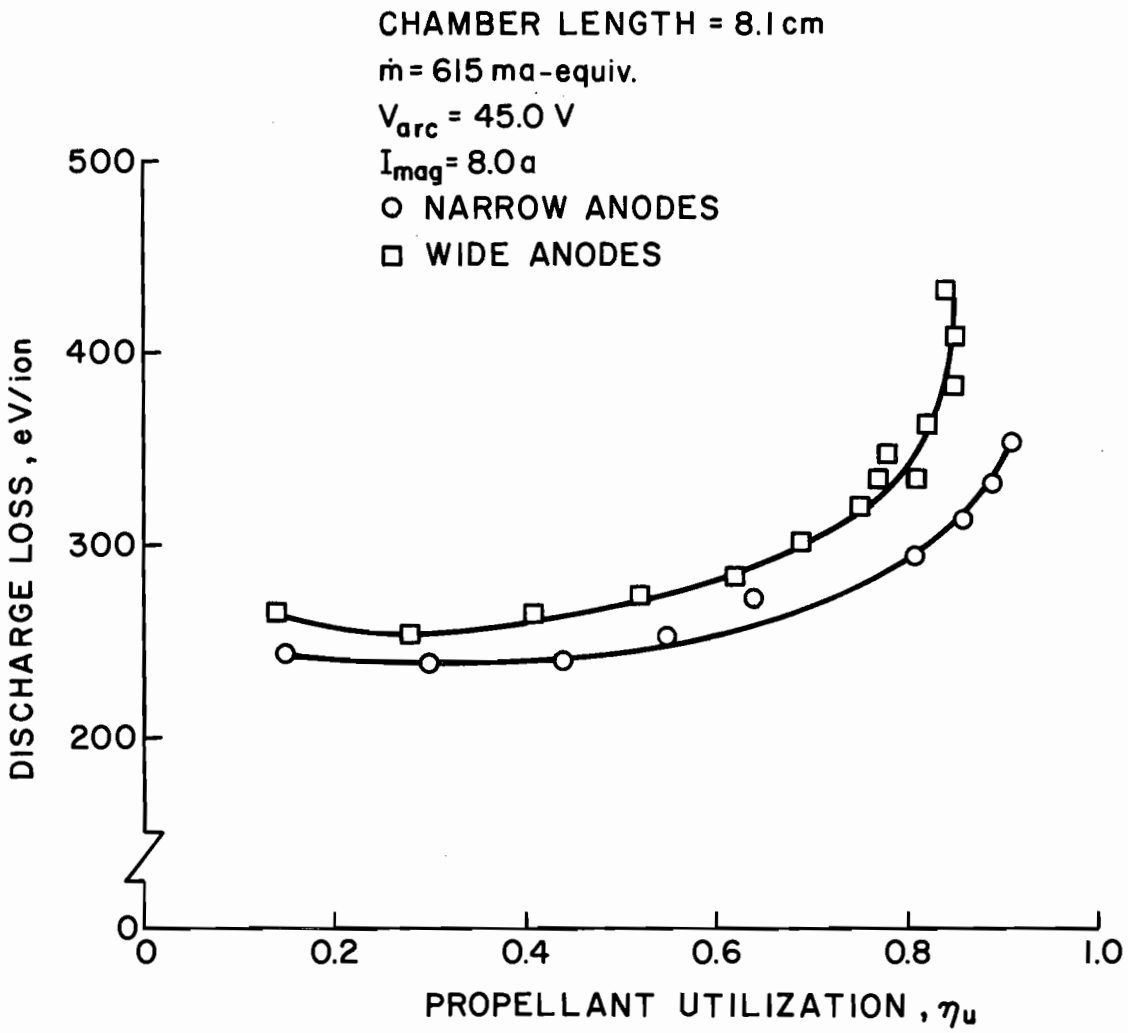

Figure 17. Variation of discharge-chamber performance for different anode widths with xenon propellant.

diffusion (using the method of Kaufman[29]). In order to obtain the current due to Bohm diffusion, voltage and density gradients within the plasma had to be determined. Detailed Langmuir probe surveys were obtained in the fringe field region, as well as selected points in the bulk plasma, to determine the necessary plasma properties. Within the fringe field, data was obtained at 2 mm increments radially and 6 mm increments axially. Typical results are shown as approximate equal value contour lines in Figure 18 and 19 for argon and xenon. Comparison of these results with those presented in Figures 14 and 15 indicates that they are similar with the exception of the Maxwellian temperature which is lower in this case. Higher temperatures were measured at some points within the bulk plasma, however, because this was primarily a survey of the fringe field region, sufficient data for a higher temperature contour line were not available. However, near the boundary of the chamber the Maxwellian temperature in Figures 14 (b) and 15 (b), does decrease to approximately the values indicated in Figures 18 (b) and 19 (b).

From these results, as well as from the results of additional surveys, the majority of the change in values was found to occur within a distance of about one-half the pole piece spacing from the anode. However, to simplify calculations, the distance was assumed to be 1 centimeter. To further simplify the calculations, the voltage change over this distance was assumed to be equal to the Maxwellian electron temperature and the density change equal to the Maxwellian electron density. Finally, to calculate the anode current, the area through which the electrons could diffuse to each anode was assumed to have a width of one-half the pole piece spacing. This width was chosen since

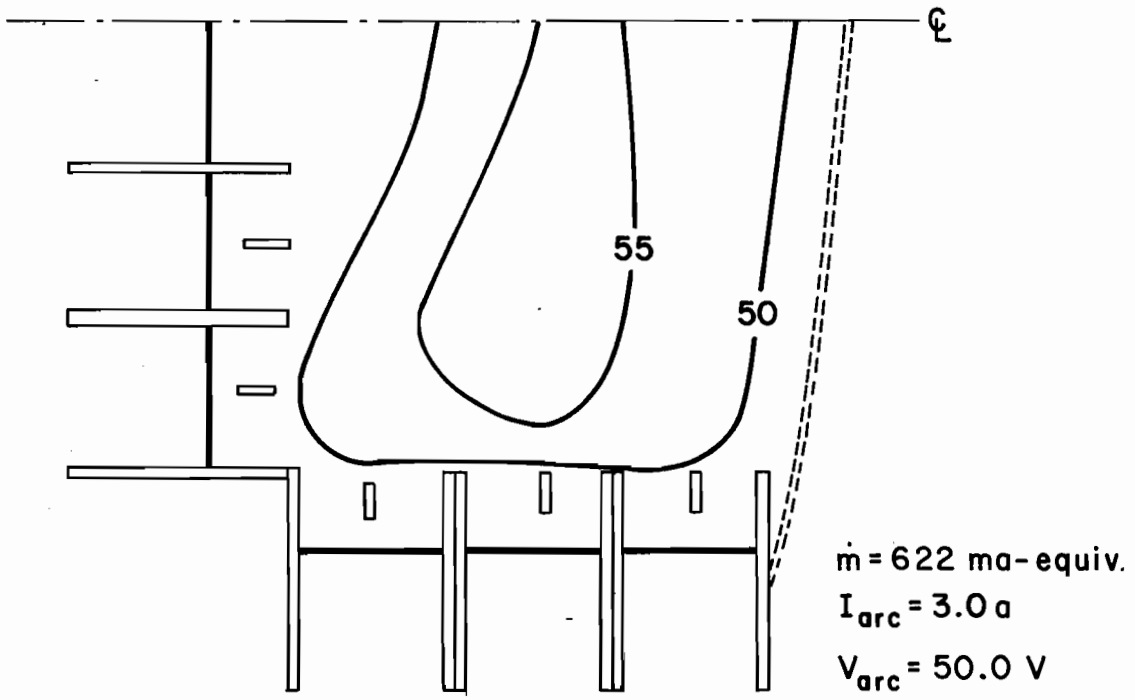

(a) PLASMA POTENTIAL, V

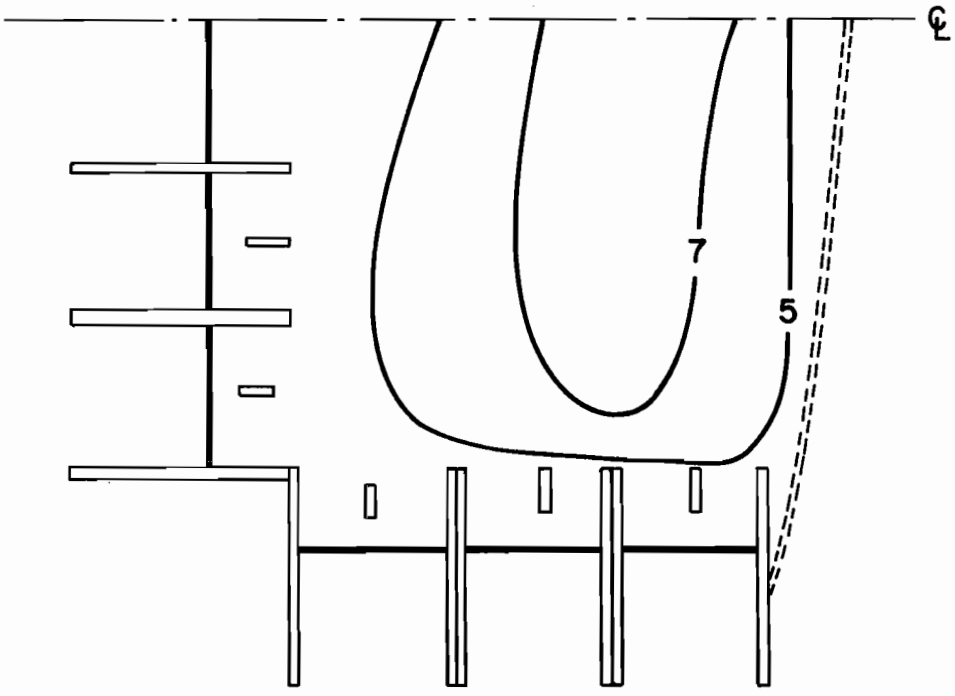

(b) MAXWELLIAN TEMPERATURE, eV

Figure 18. Plasma property contours for 8.1 cm chamber length with argon propellant.

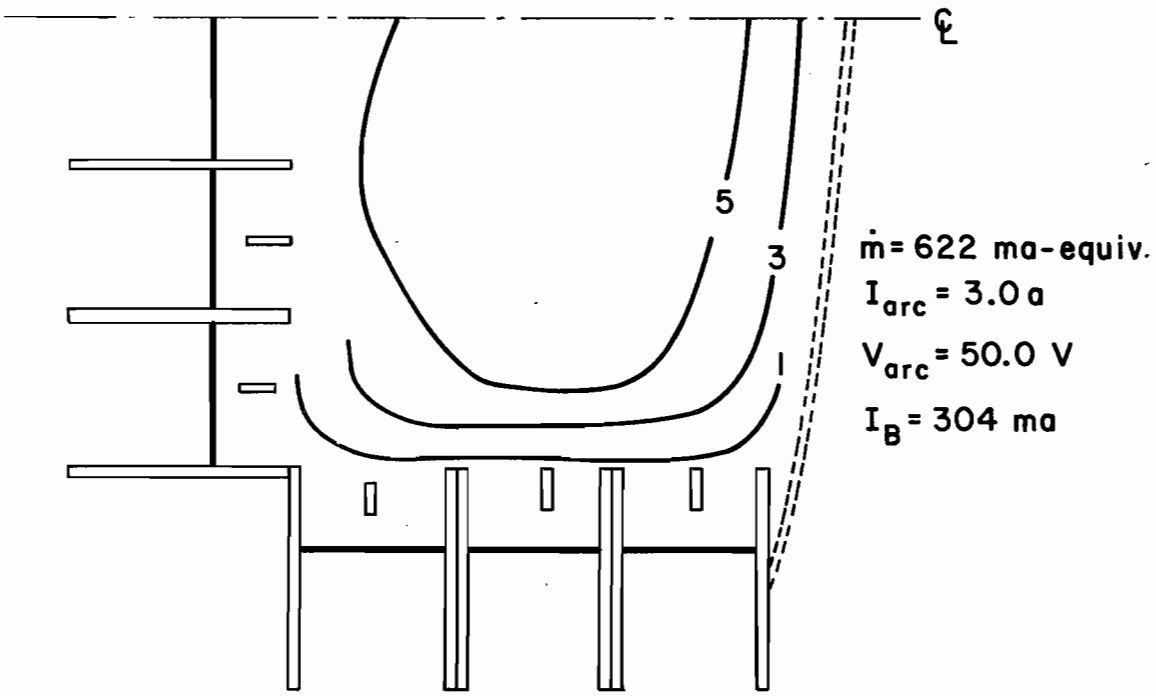

(c) MAXWELLIAN ELECTRON DENSITY, $\times 10^{-10}$ / cm^3

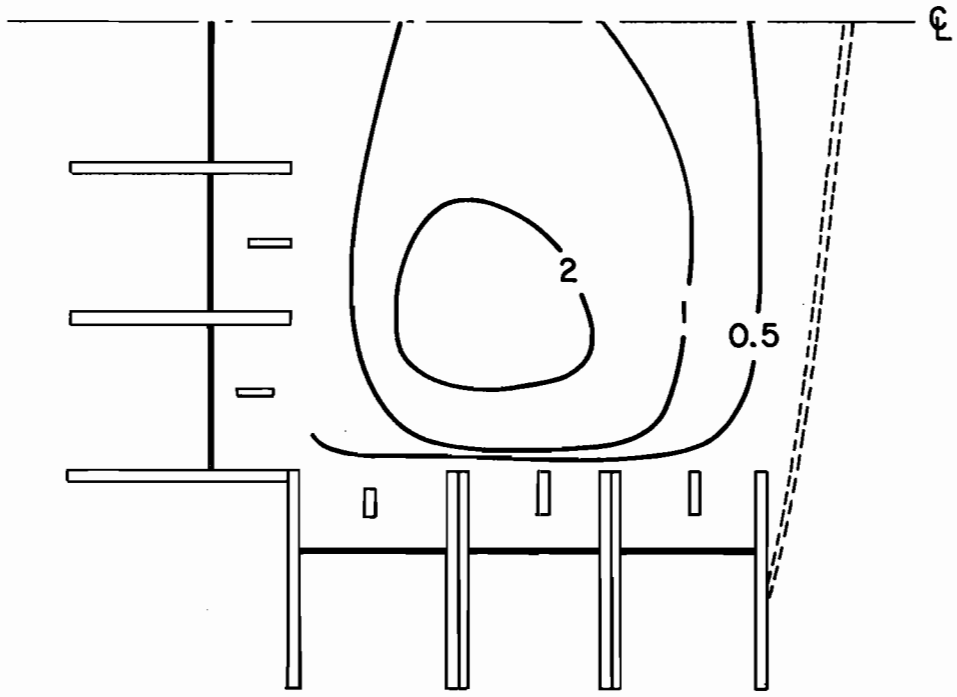

(d) PRIMARY ELECTRON DENSITY, $\times 10^{-9}$/cm^3

Figure 18. Concluded.

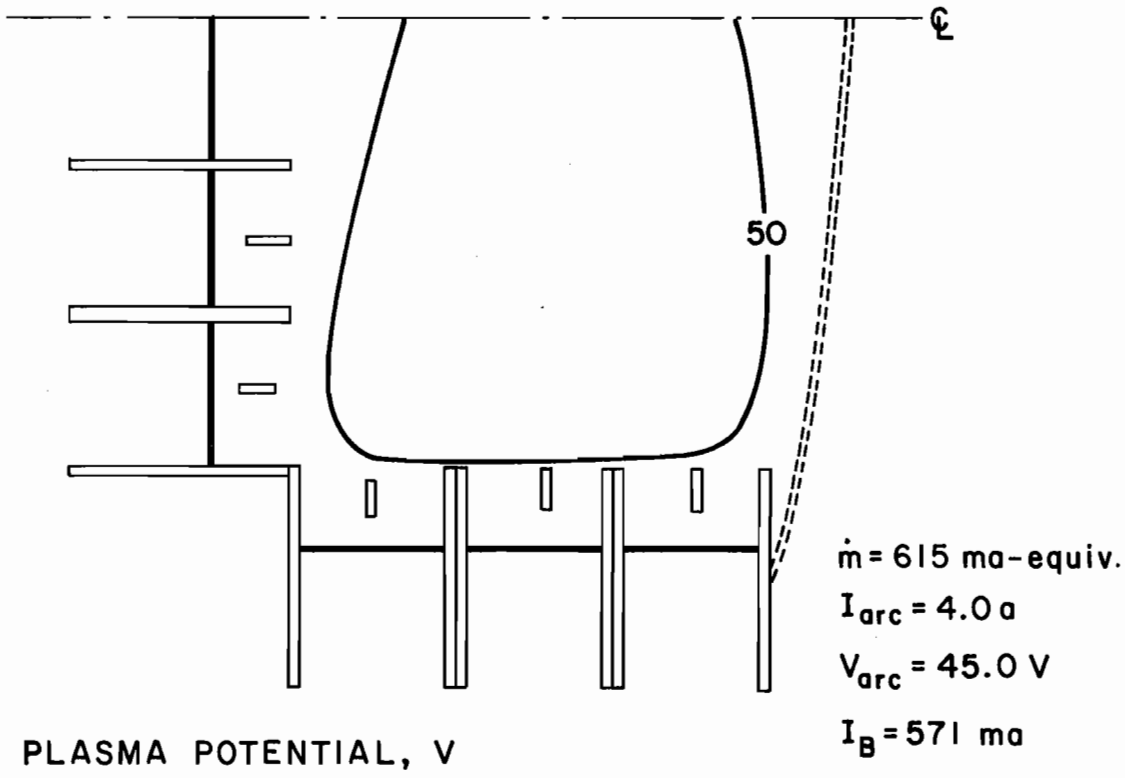

(a) PLASMA POTENTIAL, V

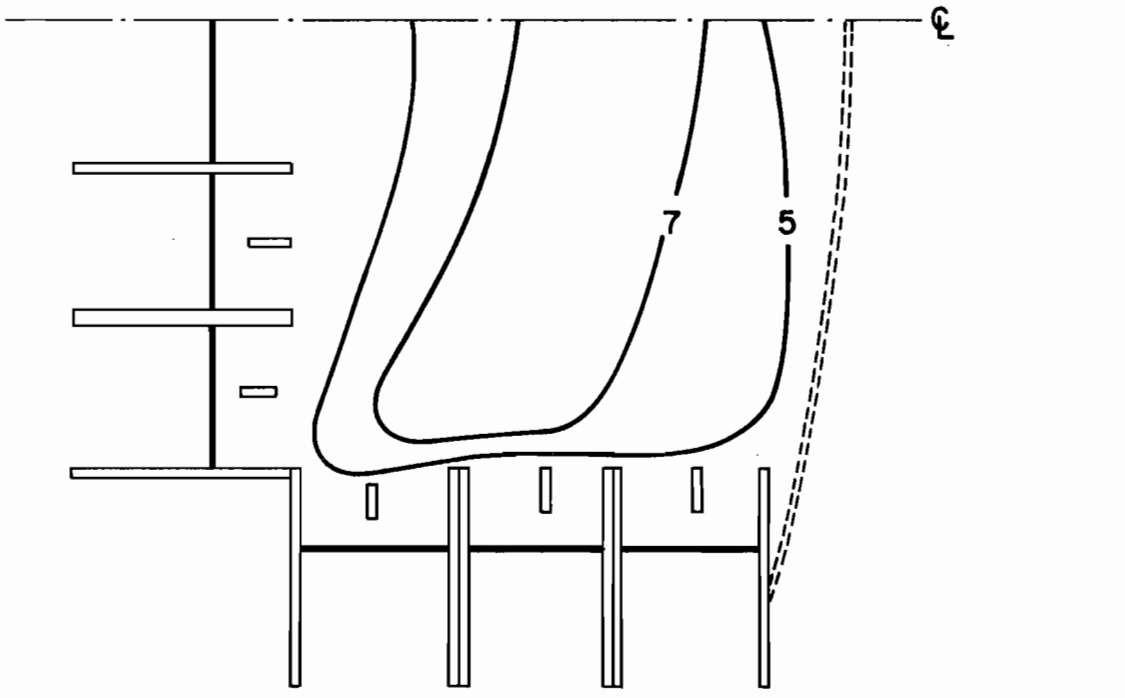

(b) MAXWELLIAN TEMPERATURE, eV

Figure 19. Plasma property contours for 8.1 cm chamber length with xenon propellant.

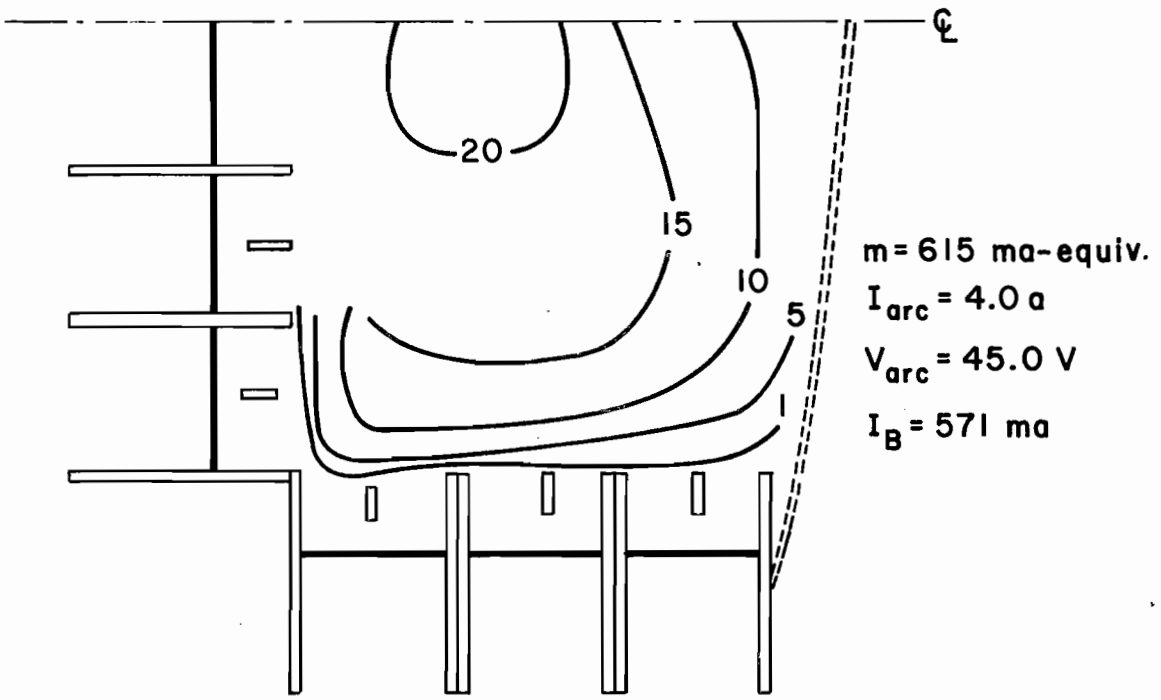

(c) MAXWELLIAN ELECTRON DENSITY, $\times 10^{-10}/cm^3$

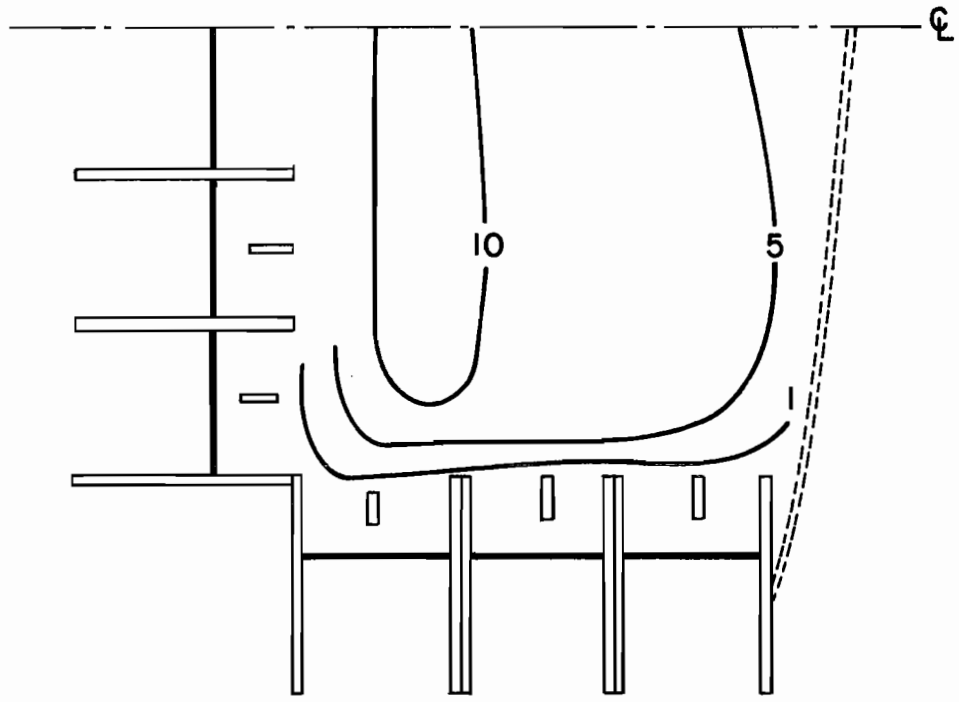

(d) PRIMARY ELECTRON DENSITY, $\times 10^{-9}/cm^3$

Figure 19. Concluded.

electron diffusion would be expected to be inhibited greatly in a region near each pole piece where the magnetic field strength is much higher.

The results obtained from these calculations for Maxwellian electron temperatures of 5 eV and 10 eV over a range of Maxwellian electron densities, are presented in Figure 20 for argon and Figure 21 for xenon. Since Bohm diffusion (dashed line) involves only the electrons, the results are independent of the propellant used and are thus the same in Figures 20 and 21. Turbulent diffusion (solid line), however, uses two-stream instability which includes the mass of the ion. Therefore, these results are dependent upon the propellant used and differ in the two Figures. Note that the currents are smaller for a given density with xenon indicating that the plasma is slightly less turbulent for this propellant. Experimental results (solid symbols) are also presented in Figure 20 and 21. The densities and temperatures were obtained from Langmuir probe data and the current is the corresponding measured anode current. For both propellants, there is reasonable agreement between theoretical and experimental results. This agreement is even more reasonable considering that the maximum discharge currents calculated using laminar diffusion theory were less than 5 ma for both propellants. These results strongly suggest that the plasma within the magnetic fringe field of the MP-II thruster is turbulent. Because of this turbulence, the escape of Maxwellian electrons will not require large potential differences near the anodes for the magnetic field strengths used.

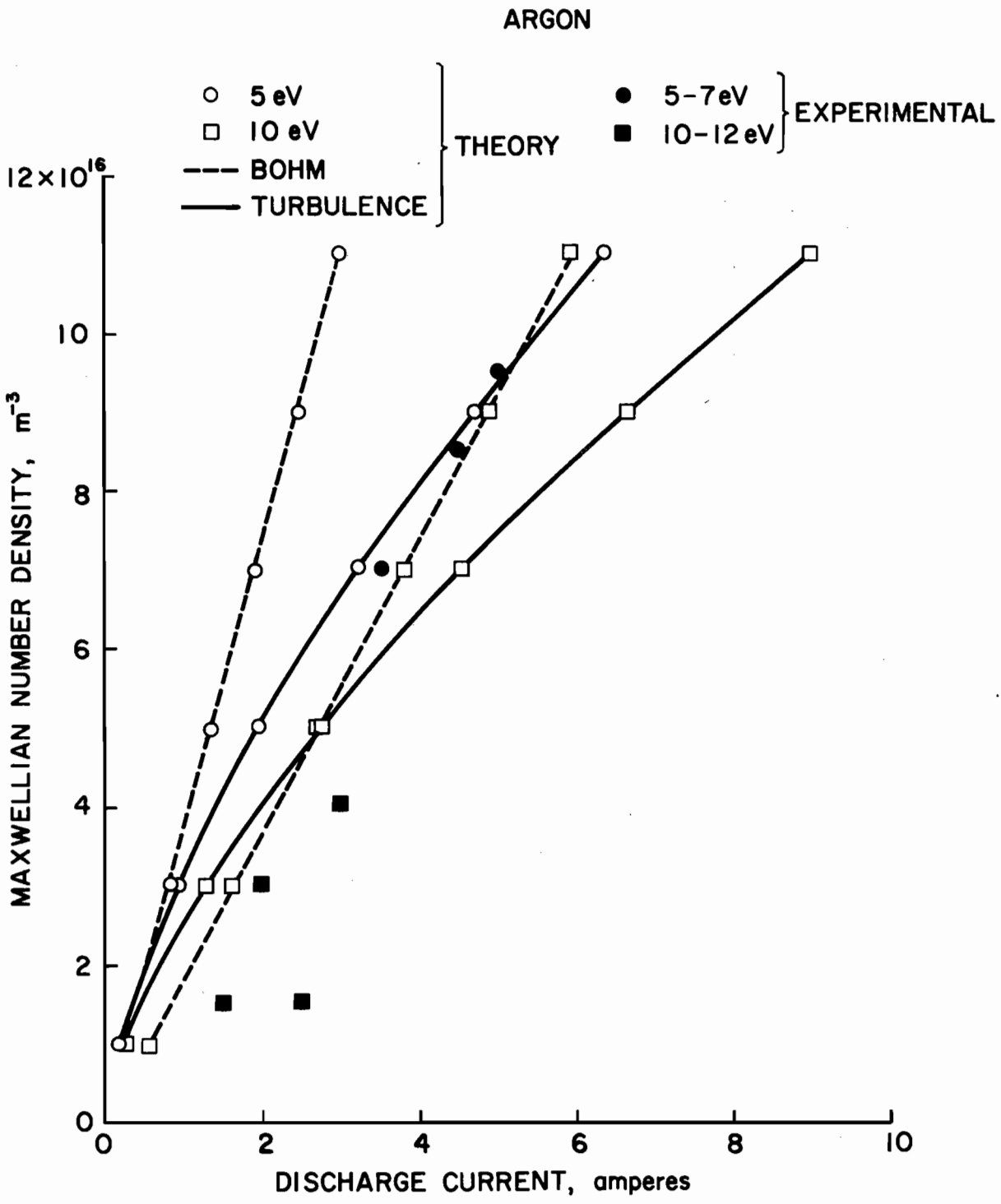

Figure 20. Comparison of calculated and measured discharge currents at various Maxwellian number densities for electron temperatures of about 5 and 10 eV with argon propellant.

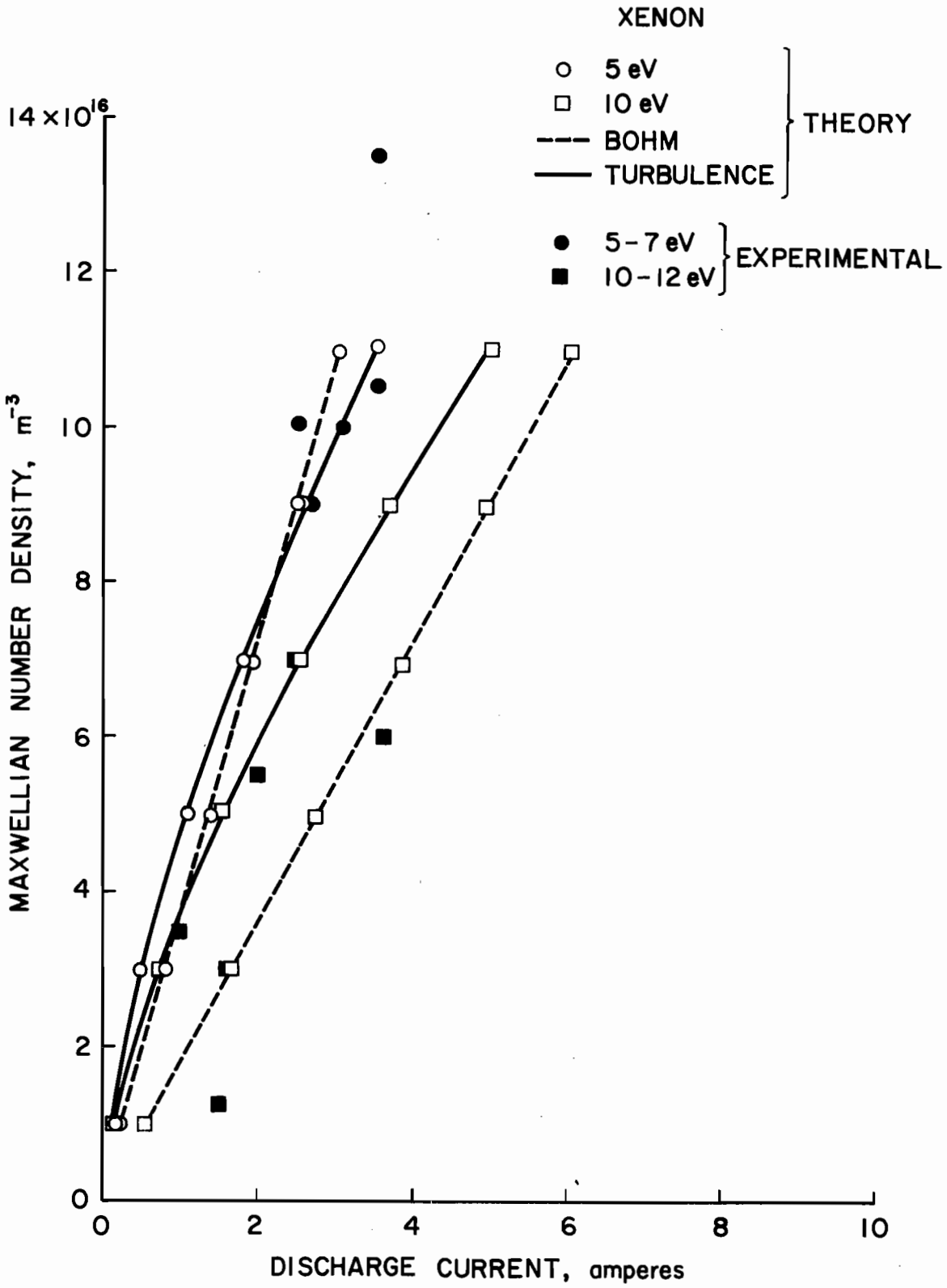

Figure 21. Comparison of calculated and measured discharge currents at various Maxwellian number densities for electron temperatures of about 5 and 10 eV with xenon propellant.

Effect of Discharge Chamber Configuration

The effects of discharge-chamber length on performance were investigated. The chamber length was decreased from a maximum of 16.2 cm in 2.7 cm increments for both propellants. The electromagnet current was kept constant at 8 amperes, which was near optimum for both propellants.

Discharge-chamber performance is shown in Figure 22 for argon. Minimum discharge losses decreased as the discharge-chamber length decreased from 16.2 cm to 8.1 cm, and then increased slightly at the 5.4 cm length. Operation was not possible with argon at the 2.7 cm length. The maximum utilization decreased continuously with a decrease in discharge-chamber length. Except for the increase in losses at the 5.4 cm length, these trends are in agreement with the classical effects of discharge-chamber length. That is, the longer chamber gives a higher probability of ionization (hence higher utilization), but it also gives a higher probability of ion recombination on the walls of the discharge chamber (hence higher discharge losses).

To obtain some additional insight into the trends of Figure 22, the neutral loss rates were calculated for the five chamber lengths using the method of Kaufman and Cohen[32] with a numerical value from the center of the scatter band given therein. This method gives a single neutral loss rate that should correspond to the "knee" of the discharge loss versus utilization curve. Because the scatter band is quite large, close numerical agreement should not be expected. For argon with 5.4, 8.1, 10.8, 13.5, and 16.2 cm long chambers, the predicted loss rates were 0.486, 0.390, 0.343, 0.315, and 0.296 ampere-equivalent. For a

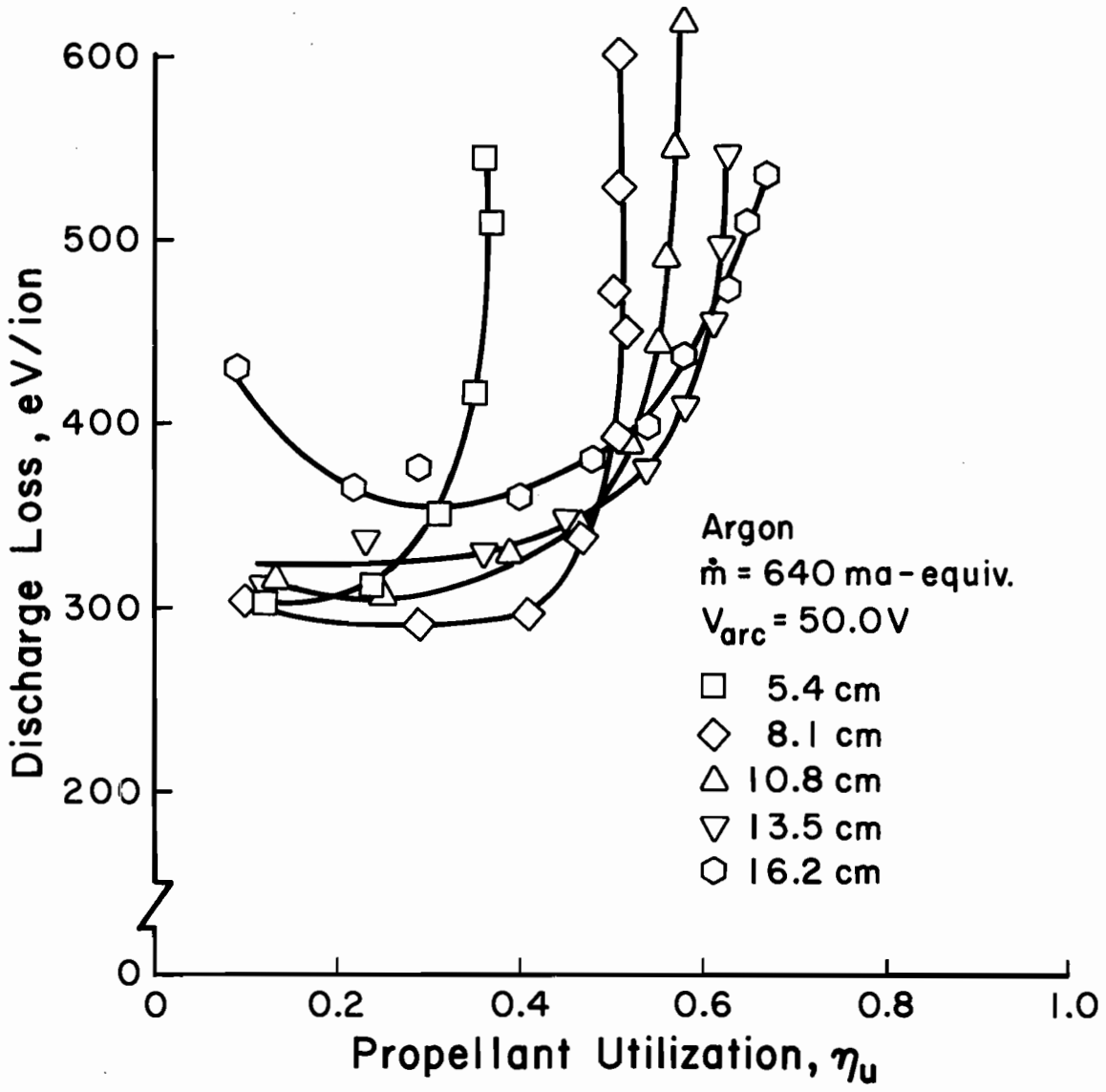

Figure 22. Effect of chamber length on discharge-chamber performance with argon propellant.

neutral flow rate of 0.640 ampere-equivalent, these neutral loss rates correspond to knee utilizations of 0.24, 0.39, 0.46, 0.51, and 0.54. These predicted knee utilizations appear to be in good agreement with the experimental values.

Ion beam profiles obtained in a plane 6.5 mm downstream of the center of the accelerator system for each chamber length are shown in Figure 23. Each profile was obtained at about the knee of the performance curve. The profiles are generally quite flat. As was the case with the performance curves, the 5.4 cm length yields the poorest results. In calculating the flatness parameters (ratio of average current density to peak current density) shown in Figure 23, the average current density is determined using the beam area in the plane of the probe. Because the grids are dished, the probe is about 1.3 cm downstream at the edge of the beam, which gives room for radial expansion of the beam. If the area were based on the accelerator-system diameter instead (15 cm), the values would increase to about 0.83 - 0.88. These higher values are believed to be better indicators of the beam flatness at the accelerator system and thus the efficiency of use for the accelerator-system area. The decrease in flatness parameter downstream of the accelerator system is more a measure of the lack of collimation. The degree of collimation is, of course, not necessarily related to the beam flatness at the accelerator system.

For xenon, similar performance data is shown in Figures 24 and 25. In Figure 24, in general, the minimum discharge losses decrease with chamber length from 16.2 to 8.1 cm, then increased when it was further shortened to 5.4 cm. Operation was possible at the 2.7 cm length with xenon and resulted in the lowest discharge losses obtained. At this

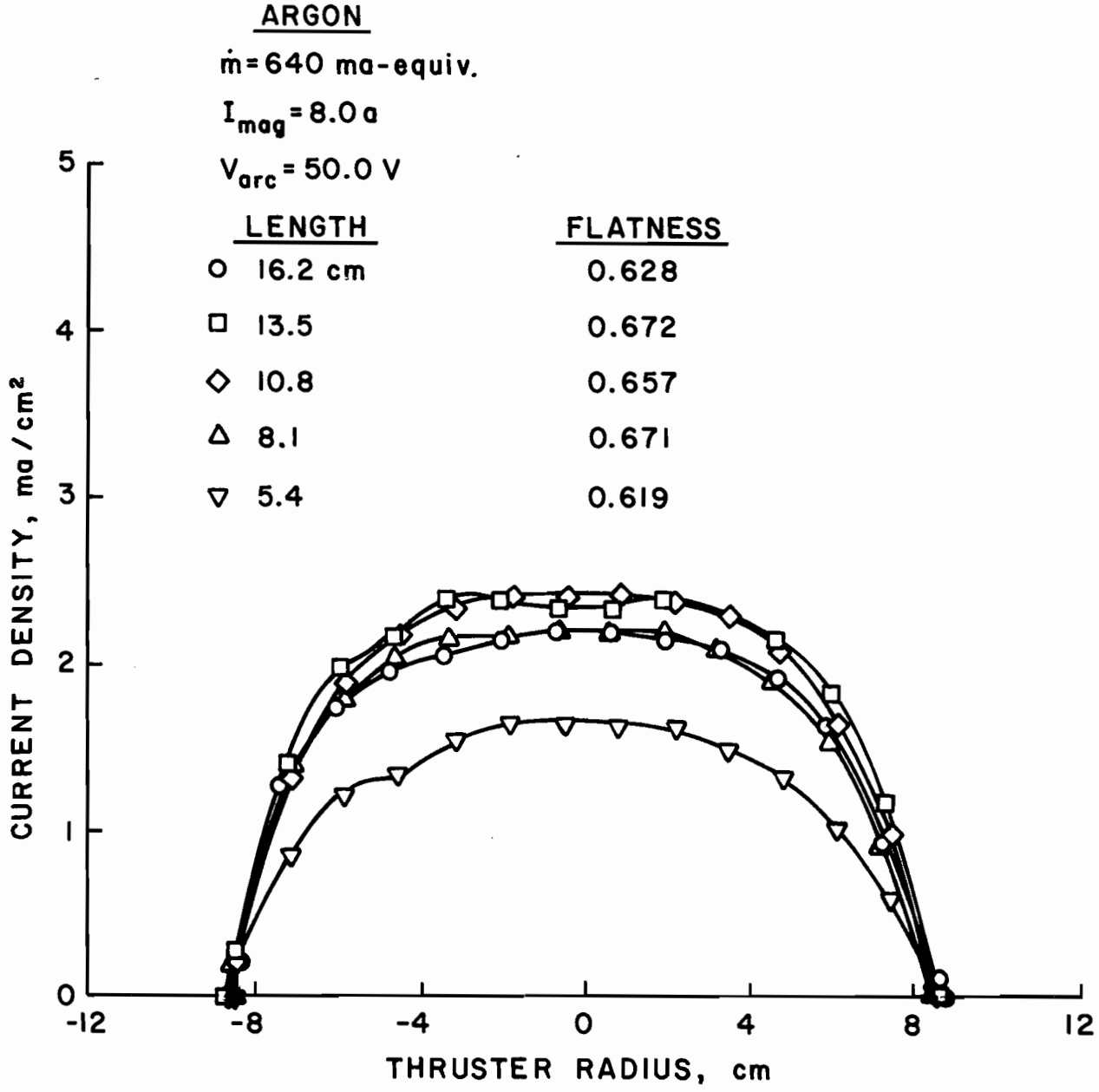

Figure 23. Effect of chamber length on ion beam profiles with argon propellant.

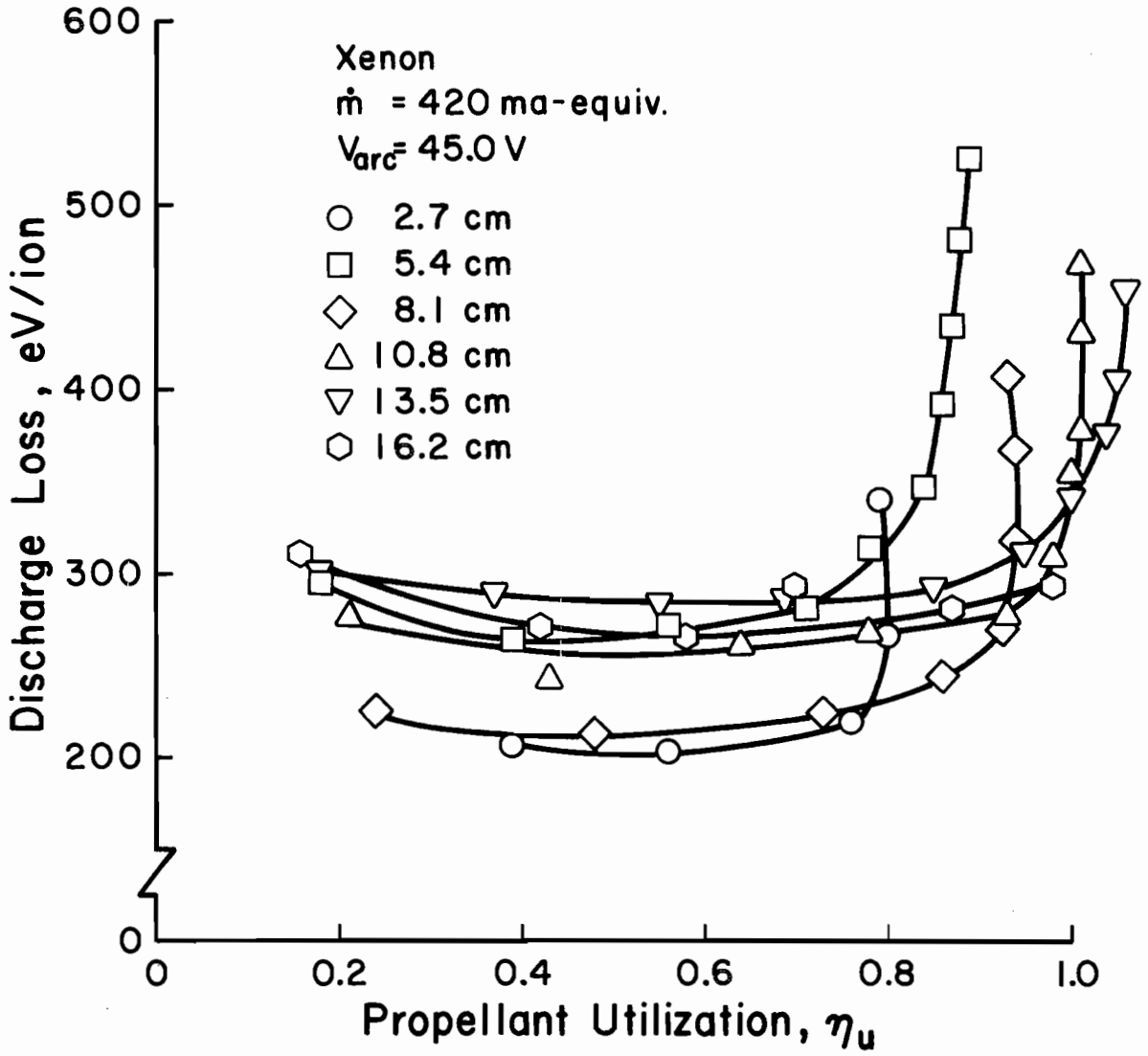

Figure 24. Effect of chamber length on discharge-chamber performance with xenon propellant.

length, however, the discharge was unstable and subject to extinction from any perturbation. Except for the 16.2 cm length, which was constrained by a cathode emission limit, the maximum utilization again decreased with decreased chamber length. Using the same procedure as with argon, the predicted loss rates were 0.142, 0.089, 0.072, 0.063, 0.057, and 0.054 ampere-equivalent for discharge chamber lengths of 2.7, 5.4, 8.1, 10.8, 13.5, and 16.2 cm respectively. For a 0.420 ampere-equivalent xenon flow rate, these neutral loss rates correspond to knee utilizations of 0.66, 0.79, 0.83, 0.85, 0.86, and 0.87. These predicted knee utilizations appear to be in reasonable agreement with experimental data. The discrepancy between predicted values and experimental data for the three longer chambers is due, at least in part, to the presence of double ions. As explained in the Appendix, complete double-ion data were obtained at only one chamber length. Because of this, the correction used for the three longer chambers was felt to be somewhat less than it should have been.

The corresponding ion beam profiles are shown in Figure 25. As with argon, there is a substantial decrease in beam uniformity (flatness parameter) with the 5.4 cm length. Flatness parameters in the plane of the grids, with the exception of the 5.4 cm length, are about 0.83 - 0.93. The flatness parameters given in Figure 25 are for the plane of the probe.

The increase in minimum discharge losses when going from an 8.1 cm length to a 5.4 cm length (both argon and xenon) and the decrease in going from 5.4 cm to 2.7 cm (xenon) was not expected. It is believed that these particular trends result from improper placement of the main cathode with respect to the fields above the anodes. That is, the trends would be expected to be modified if the cathode were relocated.

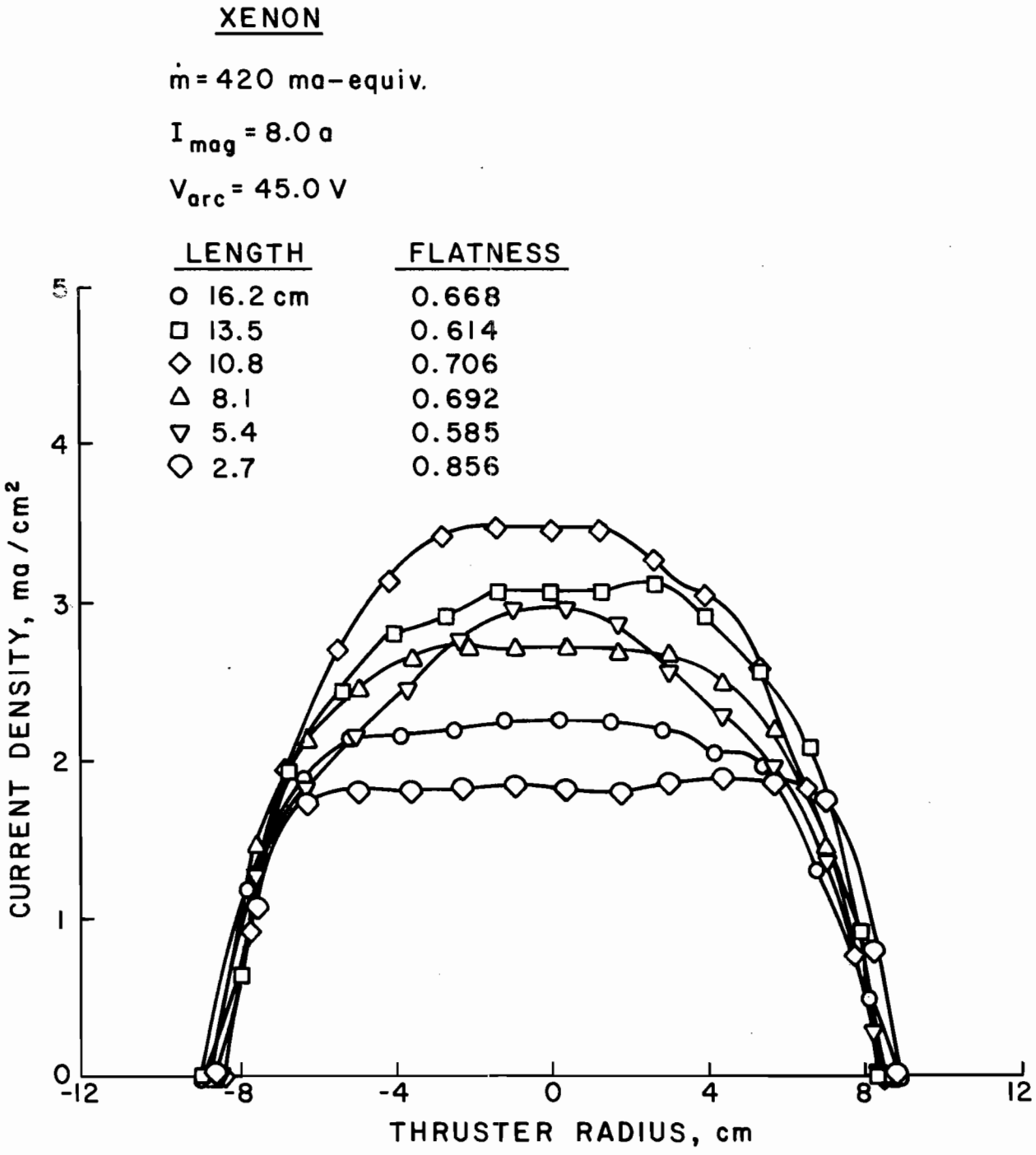

Figure 25. Effect of chamber length on ion beam profiles with xenon propellant.

The 8.1 cm length appeared to give the best compromise between minimum discharge losses and maximum knee utilization for both propellants. This length was therefore used for all remaining tests.

The effect of varying the propellant flow rate on thruster performance was investigated using the 8.1 cm long chamber for both argon and xenon. Data was obtained over approximately a 3:1 range for both propellants. Performance data obtained with argon, Figure 26, shows increased discharge losses and decreased utilization as the flow rate is decreased. The minimum discharge losses were about 300 eV/ion for the 0.922 and 1.534 ampere-equivalent flows. The higher discharge losses for the 0.416 and 0.622 ampere-equivalent flows is due to the high neutral loss rate. For the lower flow rates, this results in a significantly lower neutral density within the discharge chamber and thus higher discharge losses. The ion beam profiles are presented in Figure 27. Beam uniformity is fairly constant over the entire flow range. For these profiles, the flatness parameter at the grids is 0.85 - 0.87.

Similar flow rate data for xenon are presented in Figures 28 and 29. In Figure 28 the maximum utilization decreases with decreasing flow rate, but the minimum discharge loss remains nearly constant at about 225 eV/ion. For xenon, the neutral loss rate is much lower than for argon, thus there is little effect on neutral density and discharge losses, for all flow rates. The ion beam profiles of Figure 29 indicate even greater uniformity than was obtained with argon. This may be due to the previously indicated lesser degree of turbulence within the fringe field for this propellant. This could lead to increased

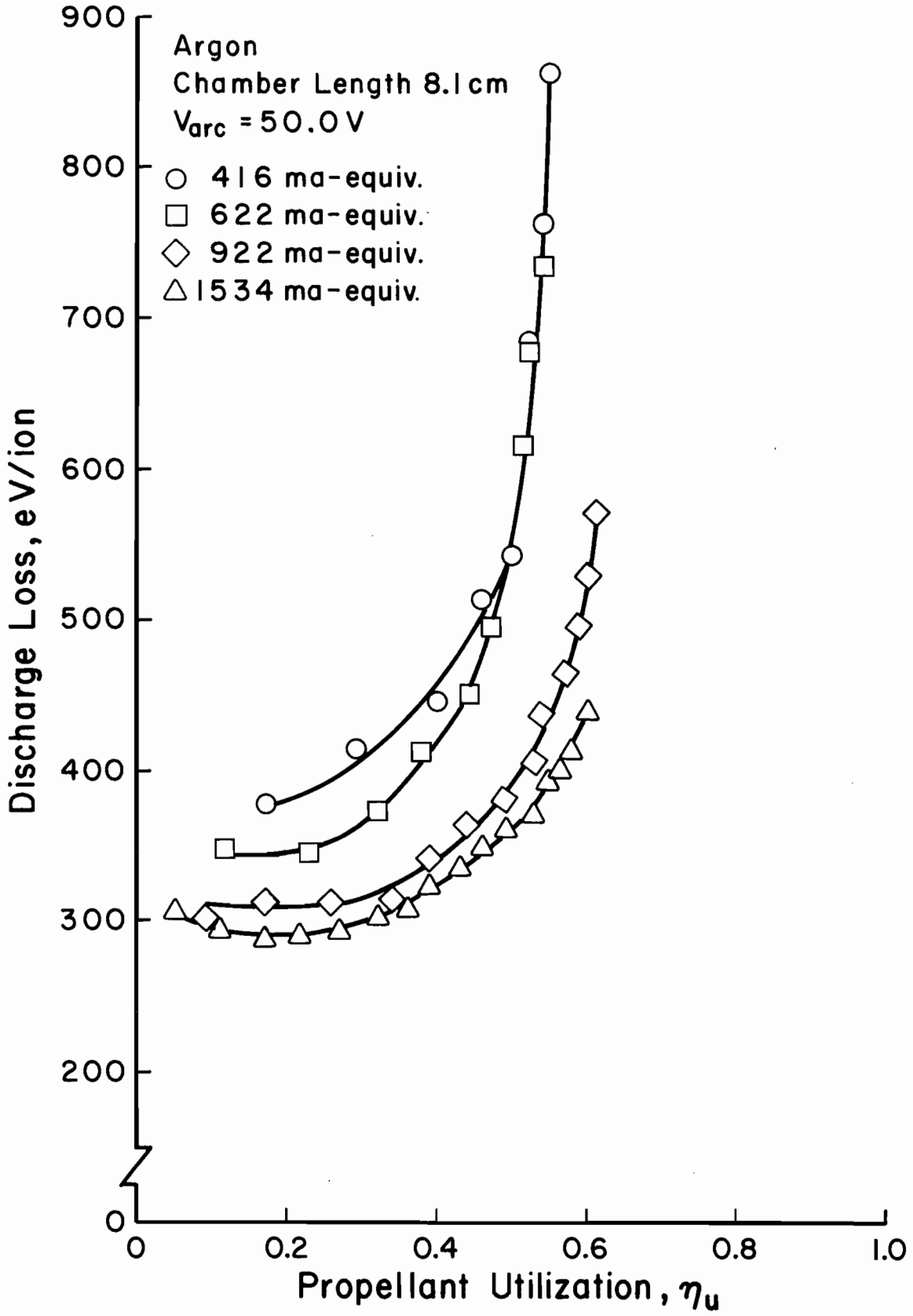

Figure 26. Effect of flow rate on discharge-chamber performance with argon propellant.

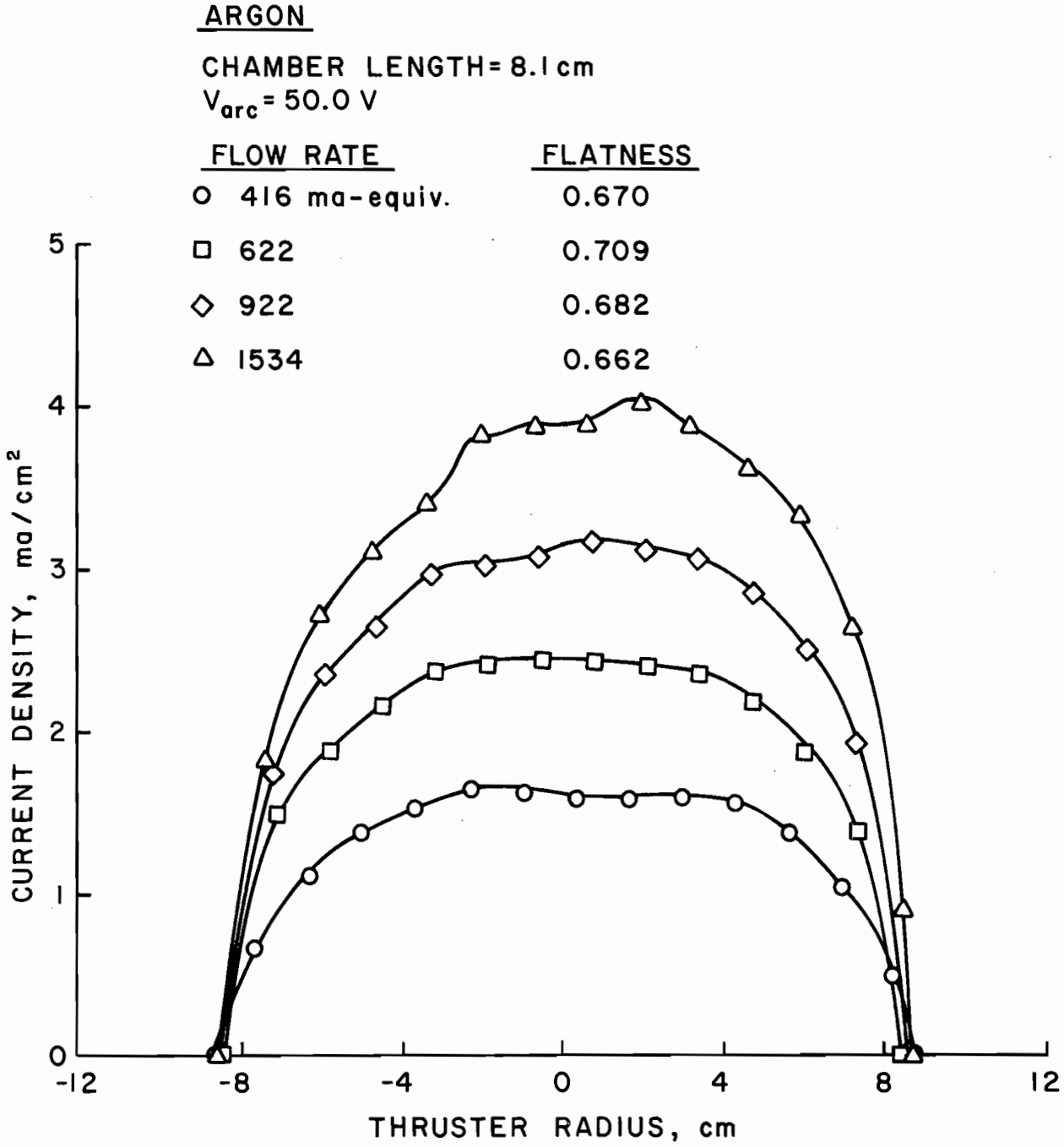

Figure 27. Effect of flow rate on ion beam profiles with argon propellant.

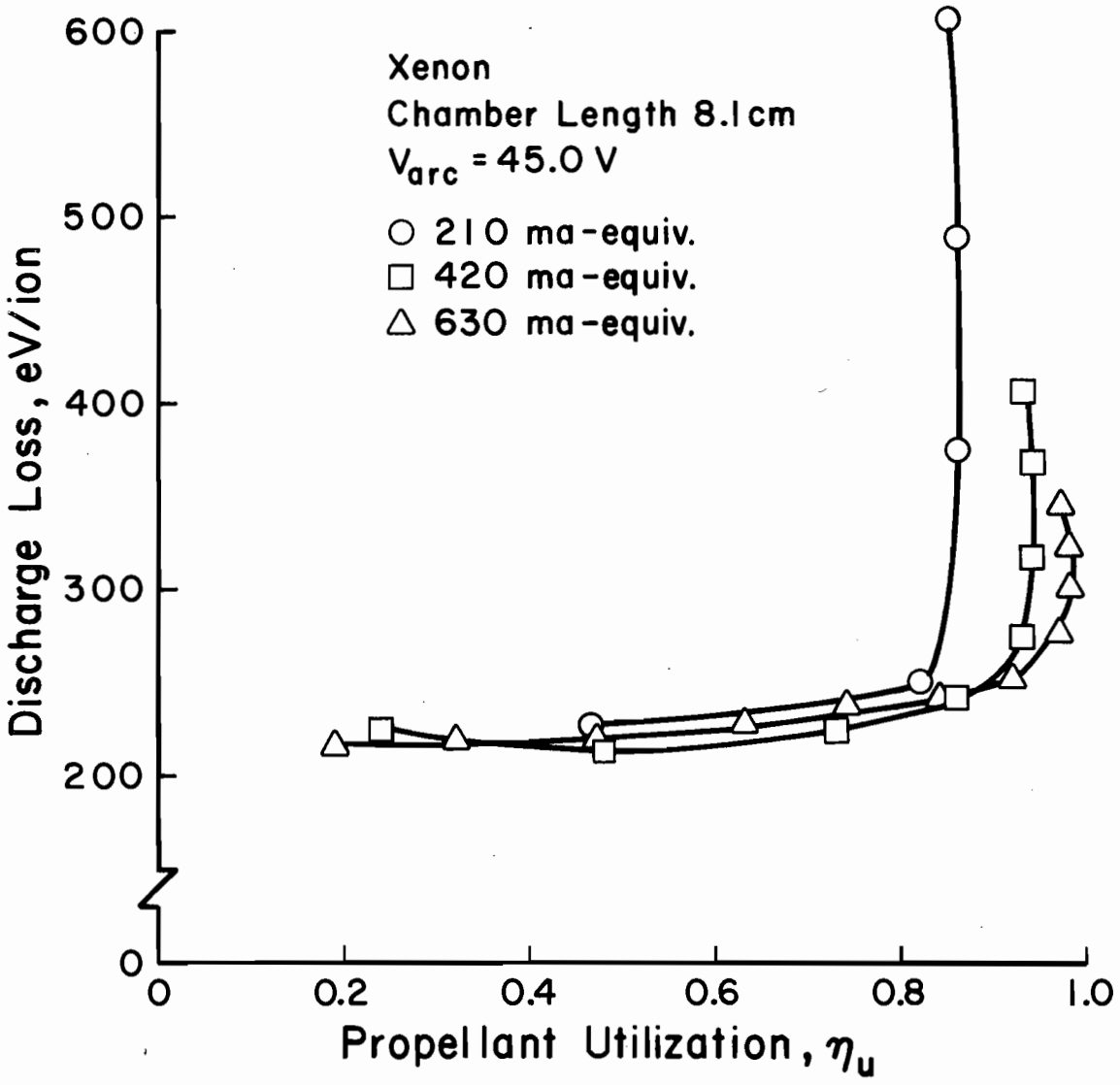

Figure 28. Effect of flow rate on discharge-chamber performance with xenon propellant.

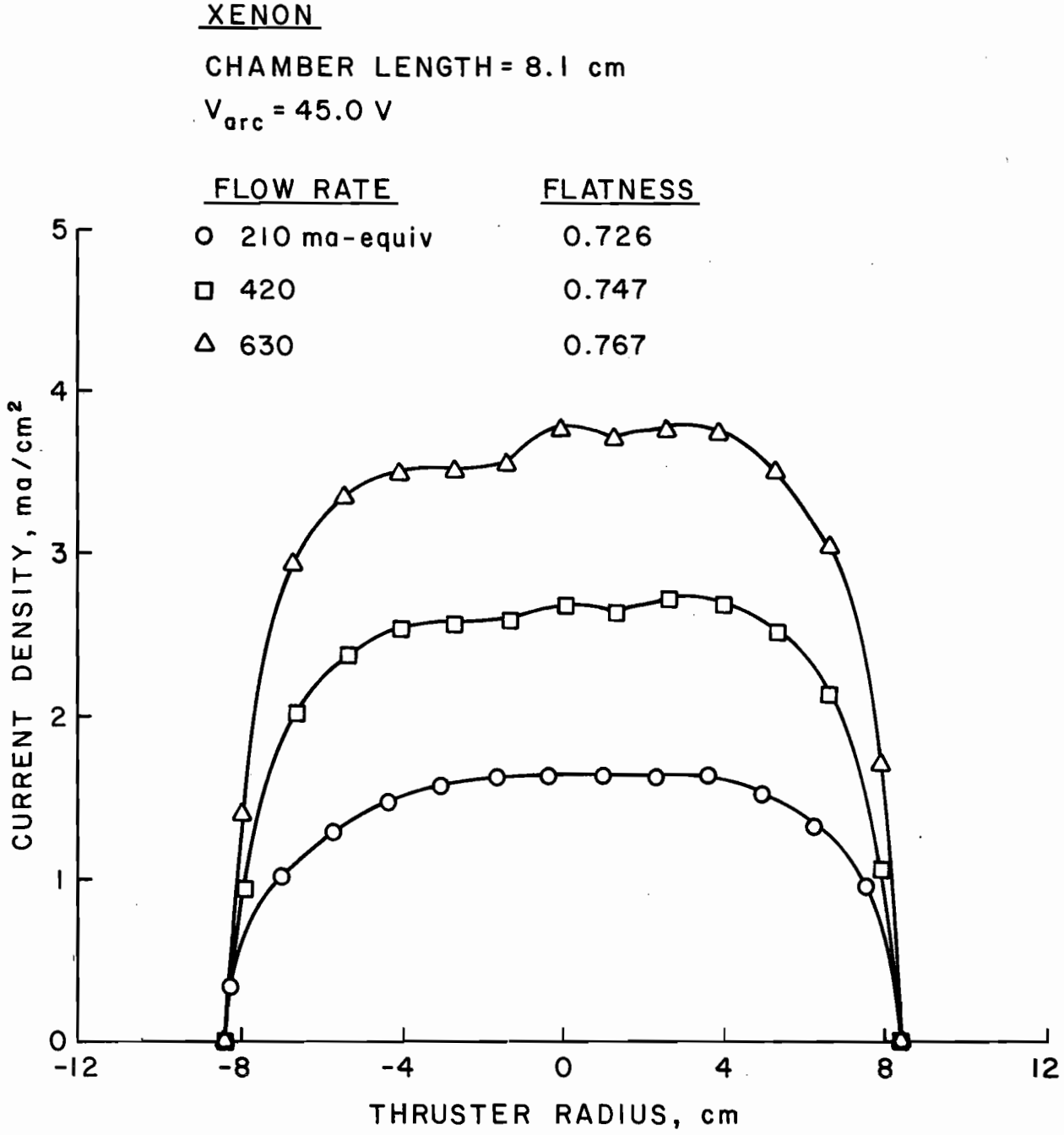

Figure 29. Effect of flow rate on ion beam profiles with xenon propellant.

ionization near the boundaries as indicated by the profiles. Flatness parameters calculated at the grids are 0.90 - 0.93.

30-cm Diameter Multipole Source

As indicated in the first chapter, the multipole design was expected to eliminate many of the problems normally associated with the scaling of a thruster to a different size. A 30-cm diameter multipole ion source was designed and built using the procedure and theory present herein.[26] Although the performance correlations presented in the following section were not completed at the time the source was designed, the trends indicated in Figures 22 and 24 were used. That is, that the best compromise between minimum discharge losses, maximum propellant utilization, and beam uniformity occurred at a length-to-diameter ratio of about one-half. However, because this ratio typically decreases with increasing diameter, a value of one-third was used. Subsequent completion of the performance correlations has resulted in a better basis from which this selection can be made.

The design is similar to the MP-II design with the major differences being a circumferential cathode and permanent magnets. The magnetic fringe field was adjusted during assembly to approximate the integral of magnetic field over distance to the anode determined experimentally with the MP-II design. Recessed corner anodes were used to obtain the proper integrated values in the corner locations.

Without any modifications after assembly, the source was operated with standard 30 cm diameter compensated dished grids having a 67 percent open area screen and 43 percent open area accelerator grid. With argon as

the propellant, the performance curve shown in Figure 30 was obtained. Discharge losses are quite low with a minimum value of about 250 eV/ion, the maximum utilization is about the same as was obtained with the MP-II. It should be noted that these data have not been corrected for either backflow or neutral propellant atoms from the vacuum facility or double ions.

An ion beam current density profile obtained 10 cm downstream from the center of the accelerator grid is presented in Figure 31. The profile is quite uniform over the center 20 cm of the beam. The flatness parameter at the plane of the grids was determined by using additional profiles taken at 20 and 30 cm and extrapolating the value of the peak current density to the grids. The average current density was obtained from the area of the beam and the measured beam current. The resultant flatness parameter value of 0.795 is excellent and is even more impressive considering that it was obtained from an unmodified design.

Performance Correlation

As indicated previously, because of the large range of configurations tested the possibility of correlating performance for different lengths was examined. A modified version of the neutral-loss parameter, $I_o(1-\eta_u)m_i\ \sigma(V_p/A_p)/A_o$, determined in Chapter 4, was used in this initial performance correlation. Inasmuch as the accelerator system was constant for all data, the effective open area A_o was omitted. Also, the use of data for only one gas at a time permitted ion mass m_i and ionization cross section σ to both be omitted. These omissions left

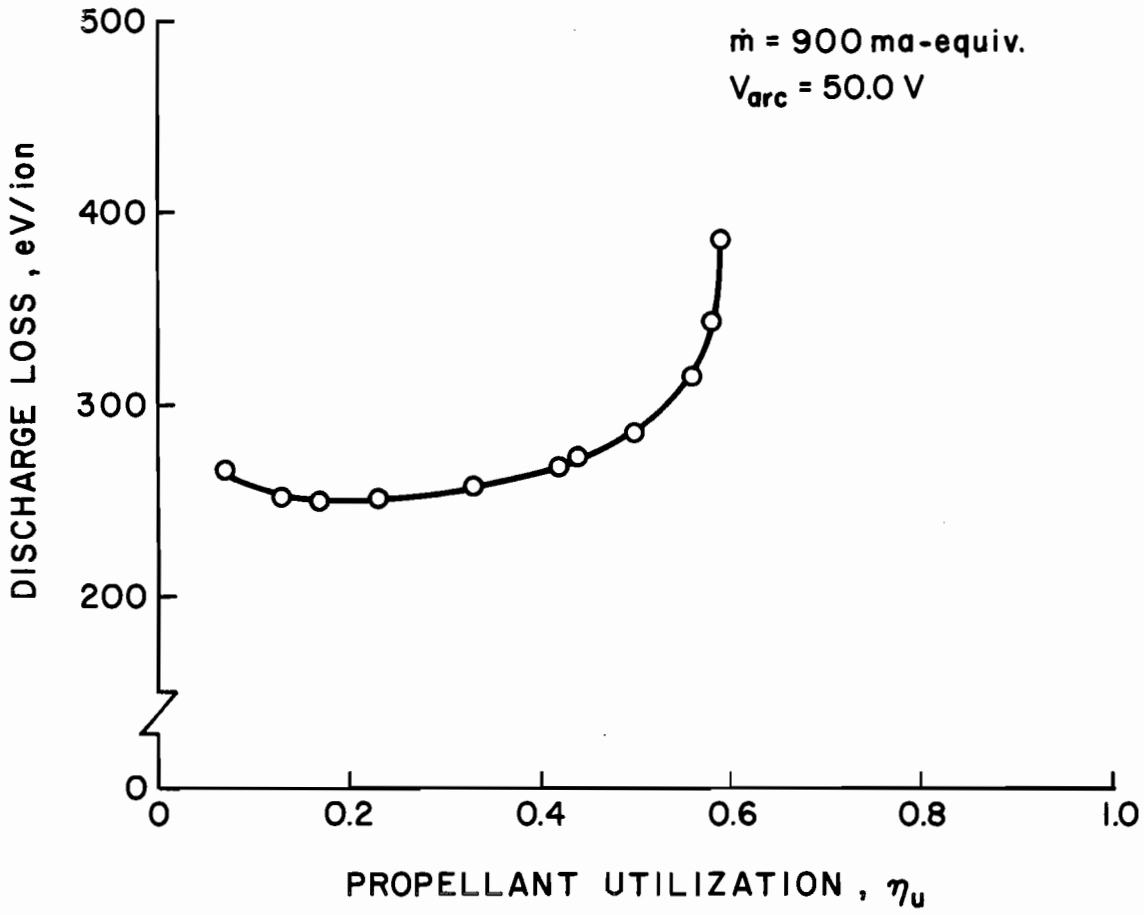

Figure 30. Discharge-chamber performance for 30 cm diameter ion source with argon propellant.

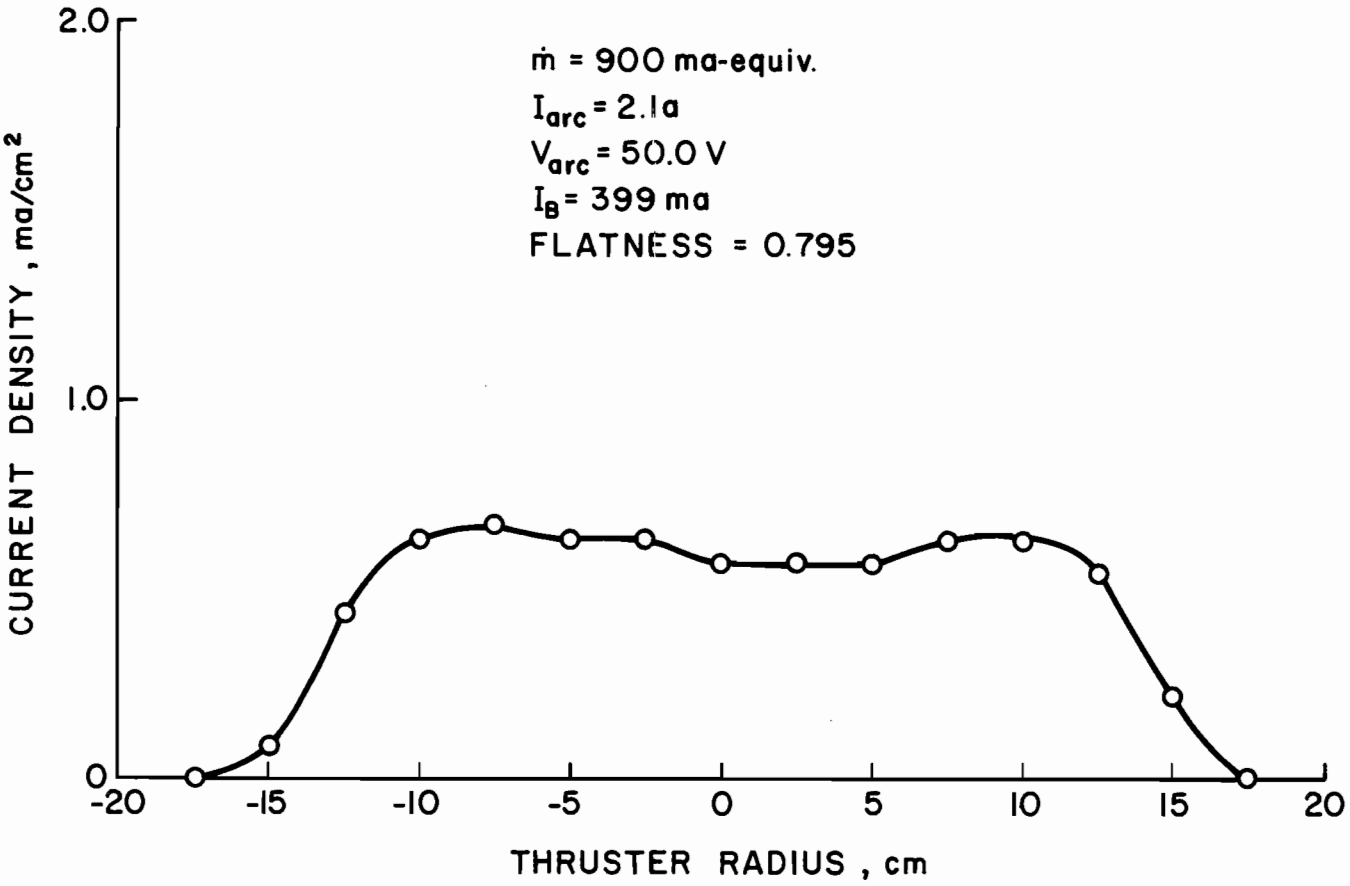

Figure 31. Ion beam profile for 30 cm diameter ion source with argon propellant.

$I_o(1-\eta_u)(V_p/A_p)$ where I_o is the total neutral flow rate in amperes-equivalent, η_u is the propellant utilization, and V_p/A_p is the ratio of volume to outside area for the primary electron region. In a multipole thruster, the primary electron region can be approximated as the cylindrical volume enclosed by the accelerator system and the inside edges of the pole pieces and anodes. The ratio V_p/A_p has the units of meters. The discharge-loss parameter remained unchanged as the product of discharge losses and the ratio of beam area to surface area of the primary electron region.

The ion chamber data for both argon and xenon over a range of propellant utilizations, flow rates and chamber lengths are plotted in Figures 32 and 33. It is evident that these parameters give a reasonable degree of data correlation for both propellants. The solid line is the approximate average value of the data scatter band.

The expected neutral losses for the discharge-loss knee were calculated using the method of Kaufman and Cohen.[32] The results corresponded to neutral-loss parameters of 0.0077 for argon in Figure 32 and 0.0014 for xenon in Figure 33. These values are in good agreement with the knee of the data bands shown.

In order to determine how well the 30 cm data would agree with the MP-II data, a more general performance correlation was obtained. Data from Figures 32 and 33 were recalculated using the entire neutral-loss parameter. Values for the discharge-loss parameter and the neutral-loss parameter for the 30 cm were obtained from the data in Figure 30. The results are presented in Figure 34. The MP-II data bands for both argon and xenon are represented by the two shaded regions with 30 cm data being indicated by the solid symbols. Again, a reasonable degree

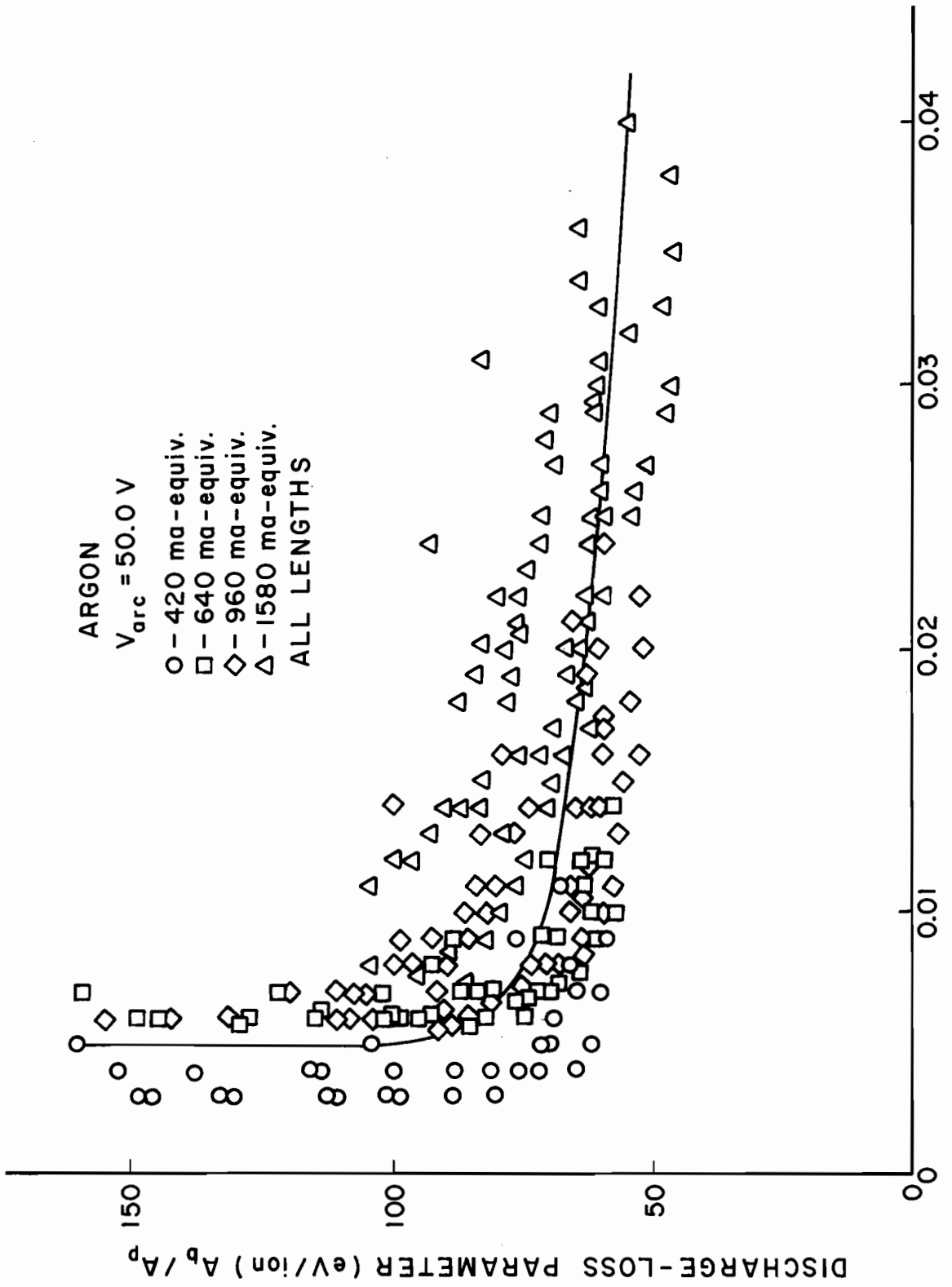

Figure 32. Performance correlation for all discharge-chamber lengths and all flow rates with argon propellant.

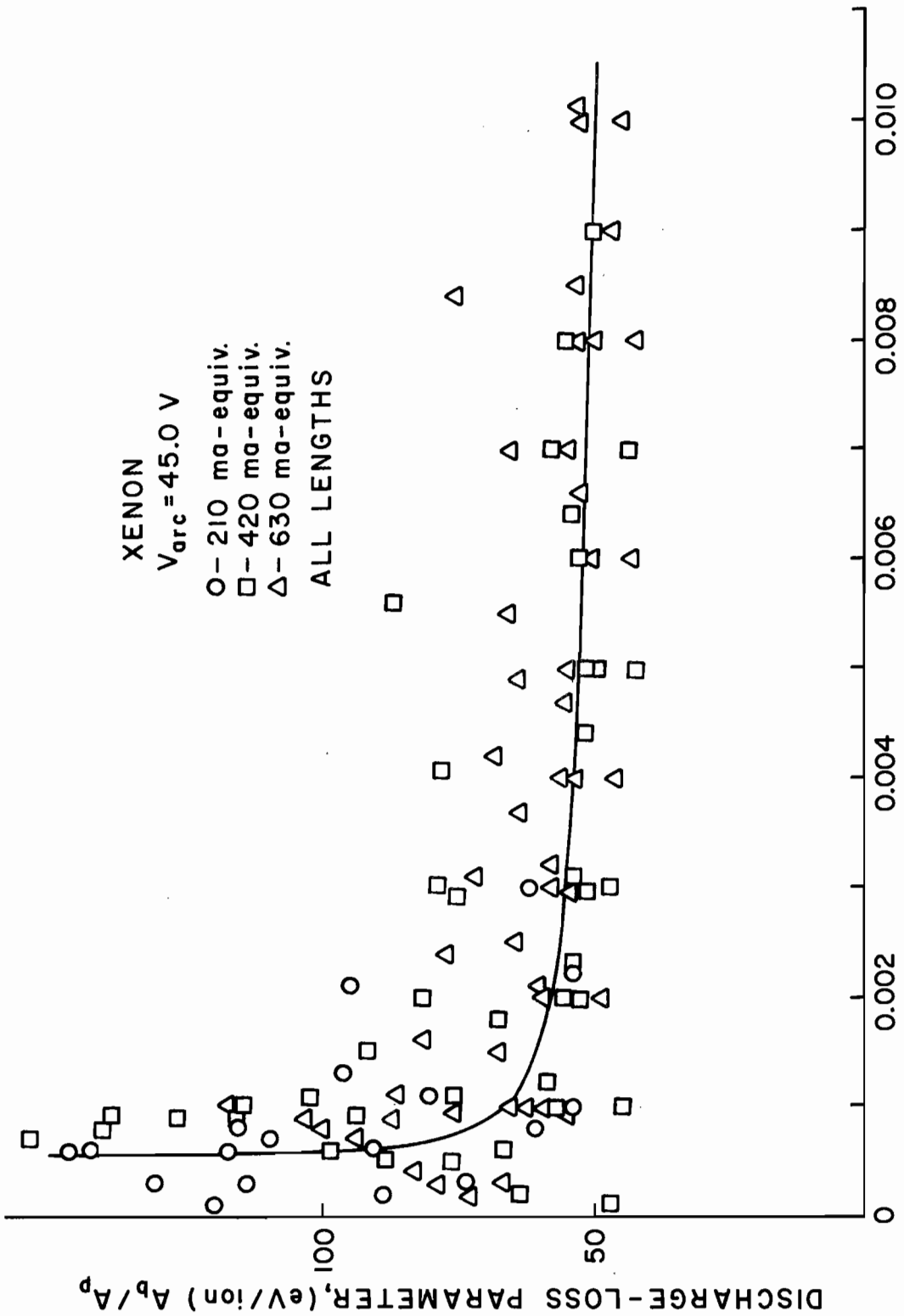

Figure 33. Performance correlation for all discharge-chamber lengths and all flow rates with xenon propellant.

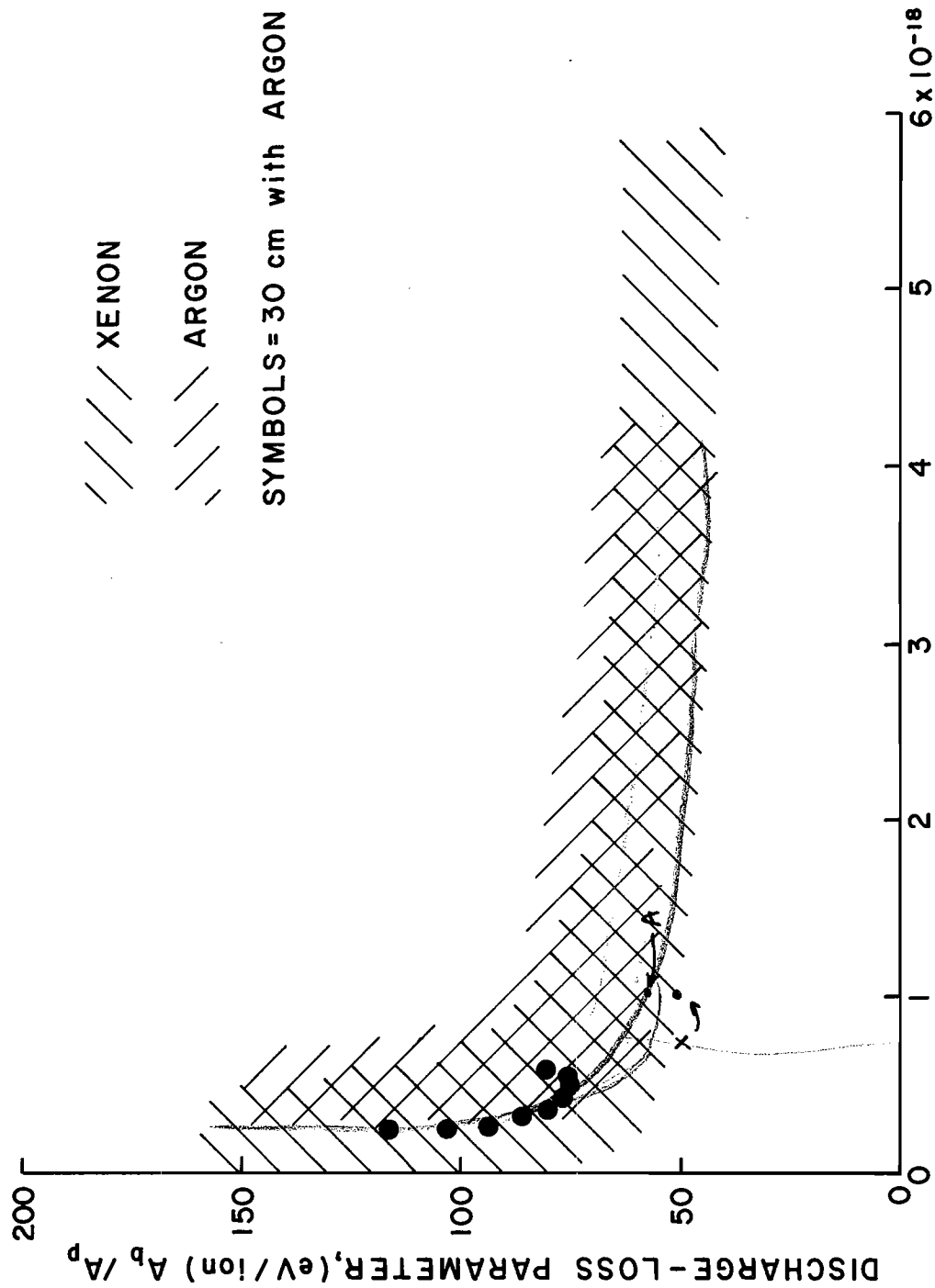

Figure 34. General performance correlation for all discharge-chamber lengths and all flow rates for both argon and xenon propellants with MP-II and for the 30 cm ion source with argon propellant.

of correlation is present. The 30 cm data is at the edge of the argon band, however, correction of this data for propellant backflow would result in its being shifted to the right, giving even better agreement.

Design Example

From the correlation given in Figure 34, the chamber length and discharge losses for a multipole thruster can be determined if the diameter, propellant, effective accelerator open area and desired utilization and beam current are specified. To further illustrate this, the following example is given.

A 20 cm diameter multipole thruster that uses mercury propellant is to be designed. The accelerator system has an effective open area equal to 30 percent of the beam area. The desired knee operating conditions are 95 percent utilization and a 800 ma beam current. Thus the following values will be used in the neutral-loss parameter

I_o = 0.842 ampere-equivalent neutral flow rate

η_u = 95%

m_i = 200 amu

$\sigma = 5 \times 10^{-20}$ m^2 Ionization Cross section

$A_o = 9.4 \times 10^{-3}$ m^2 Accel Open Area

diameter = 0.2 m.

From Figure 34, the value of the neutral-loss parameter at the center of the knee is about 7×10^{-19} amp-amu-m and the discharge loss parameter is about 75 eV/ion. Thus,

$$I_o(1-\eta_u)m_i\ \sigma(V_p/A_p)/A_o = 7 \times 10^{-19} \text{ amp-amu-m} \qquad (22)$$

Vol. Ri region

Surface Area Ri Region

and

$$(\text{eV/ion})\ A_b/A_p = 75\ \text{eV/ion} \qquad (23)$$

Substituting the preceding values into the neutral-loss parameter and solving for the chamber length results in a length of 4.6 cm. Using this length in equation (23), and solving for the knee discharge loss gives a value of 204 eV/ion.

For this thruster, if a pole piece separation of 2.7 cm is used (as in this investigation), two side sections would be required to obtain the necessary length. However, in some cases it may be desirable to change the pole piece spacing. For example, for long chamber lengths where several sections would be required, a wider spacing and thus fewer sections might be appropriate. Also, for very short chamber lengths, smaller separations may be required. In either case, the magnetic field must also be adjusted so that the criterion for required flux per unit anode length (presented in Chapters IV and V) remains unchanged.

The 30-cm diameter multipole thruster described earlier is also a design example for different performance objectives. The resultant performance of this unoptimized thruster has been shown to be excellent.

The use of the information given in Figure 34 will be a valuable aid in designing future multipole thrusters by eliminating the necessity for costly trial and error experimental programs. The example given used ion beam current and propellant utilization as the major independent design parameters. It should be apparent that different ion source design problems may require different independent design parameters. It

should also be apparent that some values for design parameters will not permit a practical solution.

VI. Conclusions

This investigation of a 15 cm diameter multipole thruster resulted in the following conclusions:

1. A design criterion is given for the integrated magnetic flux above an anode. The theoretical value of this criterion is in good agreement with experimental results. Slightly lower discharge losses, which would be desirable for space applications, can be obtained by using a value 1½ to 2 times the predicted value. The ion-chamber corner losses have been evaluated and a corrective action in the form of recessing the corner anodes has been implemented. This resulted in lower discharge losses and nearly uniform electron current densities to all anodes.
2. Diffusion across the magnetic fringe field region above an anode was found to correspond to a "turbulent" plasma condition. Experimental results were in agreement with both Bohm diffusion and a diffusion controlled by two-stream instability. This turbulent condition permits the escape of Maxwellian electrons across the fringe field region without large potential differences.
3. Low discharge losses and flat ion-beam profiles were obtained with a minimum of optimization. Minimum discharge losses were in the 300-350 eV/ion range for argon and in the 200-250 eV/ion range for xenon. Flatness parameters in the plane of the grids were typically in the 0.85-0.95 range, which equals, or betters, the best values obtained previously in highly optimized designs.

4. The performance has been correlated for a wide range of ion-chamber lengths and operating conditions. The predicted neutral losses for the discharge-loss knee are in good agreement with the experimental data.
5. A 30-cm diameter ion source designed and built using the procedure and theory presented herein, was shown capable of low discharge losses and flat ion-beam profiles without optimization. Furthermore, performance data agreed well with a more general performance correlation that included propellant type, ion-chamber size, and accelerator system open area.
6. Because of the low magnetic field strengths and the extensive use of flat or cylindrical sheet-metal parts as well as the general performance correlation information, it should be possible to rapidly translate initial performance specifications into easily fabricated, high performance prototypes.

REFERENCES

1. Wilbur, P. J., "Correlation of Ion and Beam Current Densities in Kaufman Thrusters," Journal of Spacecraft and Rockets, Vol. 10, No. 9, pp. 623-624, Sept. 1973.

2. Knauer, W., Poeschel, R. L., and Ward, J. W., "Radial Field Kaufman Thruster," Journal of Spacecraft and Rockets, Vol. 7, No. 3, pp. 248-252, Mar. 1970.

3. Kaufman, H. R., and Reader, P. D., "Experimental Performance of Ion Rockets Employing Electron-Bombardment Ion Sources," American Rocket Society Paper 1374-60, Nov. 1960.

4. Kaufman, H. R., "An Ion Rocket with an Electron-Bombardment Ion Source," NASA TN D-585, Jan. 1961.

5. Reader, P. D., "Investigation of a 10 - Centimeter-Diameter Electron-Bombardment Ion Rocket," NASA TN D-1163, Jan. 1962.

6. Bechtel, R. T., "Discharge Chamber Optimization of the SERT II Thruster," Journal of Spacecraft and Rockets, Vol. 5, No. 7, pp. 795-800, July 1968.

7. Kaufman, H. R., "Performance Correlation for Electron-Bombardment Ion Sources," NASA TN D-3041, Oct. 1965.

8. Kaufman, H. R., "Ion-Thruster Propellant Utilization," Ph.D. Thesis, Dept. of Mechanical Engineering, Colorado State University, Fort Collins, Colorado, June 1971.

9. Beattie, J. R., "Cusped Magnetic Field Mercury Ion Thruster," NASA CR-135047, July 1976.

10. Moore, R. D., "Magneto-Electrostatically Contained Plasma Ion Thruster," AIAA Paper 69-260, Mar. 1969.

11. Ramsey, W. D., "12-cm Magneto-Electrostatic Containment Mercury Ion Thruster Development," Journal of Spacecraft and Rockets, Vol. 9, No. 5, pp. 318-321, May 1972.

12. Reader, P. D., "The Operation of an Electron-Bombardment Ion Source with Various Gases," NASA TM X-52006, May 1964.

13. Schertler, R. J., "Preliminary Results of the Operation of a SERT II Thruster on Argon," AIAA Paper 71-157, Jan. 1971.

14. Byers, D. C. and Reader, P. D., "Operation of an Electron-Bombardment Ion Source using Various Gases," NASA TN D-6620, Dec. 1971.

15. Martin, A. R., "Design and Operation of an Ion Engine using the Rare Gases," Journal of the British Interplanetary Society, Vol. 26, pp. 742-752, 1973.

16. Martin, A. R., "Physical Behaviour of some Biowaste Gases in an Ion Engine," AIAA Paper 73-1113, Oct. 31 - Nov. 2, 1973.

17. Bechtel, R. T., "Performance and Control of a 30-Centimeter Diameter, Low Impulse Kaufman Thruster," AIAA Paper 69-238, Mar. 1969.

18. Poeschel, R. L., and Vahrenkamp, R., "The Radial Magnetic Field Geometry as an Approach to Total Ion Utilization in Kaufman Thrusters," AIAA Paper 72-481, April 1972.

19. Reader, P. D., "Experimental Effects of Scaling on Performance of Ion Rockets Employing Electron-Bombardment Ion Sources," American Rocket Society Paper 1781-61, 1961.

20. Martin, A. R., "Scaling Laws in Electron-Bombardment Ion Engines," Journal of the British Interplanetary Society, Vol. 25, pp. 19-29, 1972.

21. Wells, A. A., Harrison, M.F.A., White, B. M., and Harbour, P. J., "Laws for Scaling of Electron Bombardment Thrusters," Culham/IEE Conference on Electric Propulsion of Space Vehicles at Culham Laboratory, April 1973.

22. Harbour, P. J., Wells, A. A., Harrison, M.F.A., and White, B. M., "Physical Processes Affecting the Design and Performance of Ion Thrusters with Particular Reference to the 10-cm, RAE/Culham T4 Thruster," AIAA Paper 73-1112, Oct. 31 - Nov. 2, 1973.

23. Wilbur, P. J., "An Experimental Investigation of a Hollow Cathode Discharge," NASA CR-121038, Dec. 1972.

24. Vahrenkamp, R. P., "Measurement of Double Charged Ions in the Beam of a 30-cm Mercury Bombardment Thruster," AIAA Paper 73-1057, Oct. 31 - Nov. 2, 1973.

25. Beattie, J. R., in "15" cm Diameter Ion Thruster Research - 1975," (by P. J. Wilbur) pp. 100-106, NASA CR-134905, Dec. 1975.

26. Robinson, R. S., and Kaufman, H. R., "Application of Ion Thruster Technology to a 30-cm Multipole Sputtering Ion Source," AIAA Paper 76-1016, Nov. 1976.

27. Chen, F. F., Introduction to Plasma Physics, Plenum Publishing Corp., 1974.

28. Bohm, D., "Qualitative Description of the Arc Plasma in a Magnetic Field," The Characteristics of Electrical Discharges in Magnetic Fields, A. Guthrie and R. K. Wakerling, eds., McGraw-Hill Book Co., Inc., 1949.

29. Kaufman, H. R., "Electron Diffusion in a Turbulent Plasma." NASA TN D-1324, June 1962.

30. Spitzer, L., Jr., Physics of Fully Ionized Bases, Interscience Publishers, 1962.

31. Domitz, S., "Experimental Evaluation of a Direct-Current Low-Pressure Plasma Source," NASA TN D-1659, April 1963.

32. Kaufman, H. R., and Cohen, A. J., "Maximum Propellant Utilization in an Electron-Bombardment Thruster," in Proceedings of the Symposium on Ion Sources and Formation of Ion Beams, Brookhaven National Laboratory, Upton, New York, Oct. 1972.

APPENDIX

Double Ion Correction

In order to properly evaluate the performance of a thruster, propellant utilization data must be corrected for the presence of double ions. The propellant utilization, or ratio of beam current to input neutral flow rate in amperes-equivalent, assumes that all of the measured beam current is due only to single ions. If there are double ions, however, the measured beam current is

$$I_B = I_+ + I_{++} \tag{A-1}$$

and the measured utilization is

$$\eta_{u,\ meas} = (I_+ + I_{++})/I_0 \tag{A-2}$$

The actual utilization is

$$\eta_{u,\ act} = (I_+ + I_{++}/2)/I_0 \quad . \tag{A-3}$$

The correction for utilization is thus

$$\frac{\eta_{u,\ act}}{\eta_{u,\ meas}} = \frac{I_+ + I_{++}/2}{I_+ + I_{++}} \tag{A-4}$$

or

$$\frac{\eta_{u,\ act}}{\eta_{u,\ meas}} = \frac{1 + I_{++}/(2\ I_+)}{1 + I_{++}/I_+} \tag{A-5}$$

Therefore, the actual utilization can be determined once the double to single ion current ratio is known.

Using an $\vec{E}$ X $\vec{B}$ momentum analyzer, this ratio was determined for the 8.1-cm long chamber for both propellants over a range of operating conditions and flow rates. The results are presented in Figure A-1 for argon and Figure A-2 for xenon. In general, the results follow the expected trend of increasing values with increasing discharge current and voltage. Since for a given discharge current, propellant utilization was lower for the 1535 ma-equivalent flow of argon than for the other flows, lower current ratios would also be expected.

By proper interpolation of these results, it is possible to obtain an approximate double to single ion current ratio for any operating condition or flow rate within the range examined. The amount of time required to obtain and analyze a complete set of data made it impractical to acquire this data for all chamber lengths. Although the double to single ion current ratio will change slightly with chamber length, the information in Figures A-1 and A-2 was used to correct all data obtained with the 15 cm diameter thrusters. This was felt to be acceptable for a first approximation, since there would be minimum error for the data obtained at the optimum chamber length.

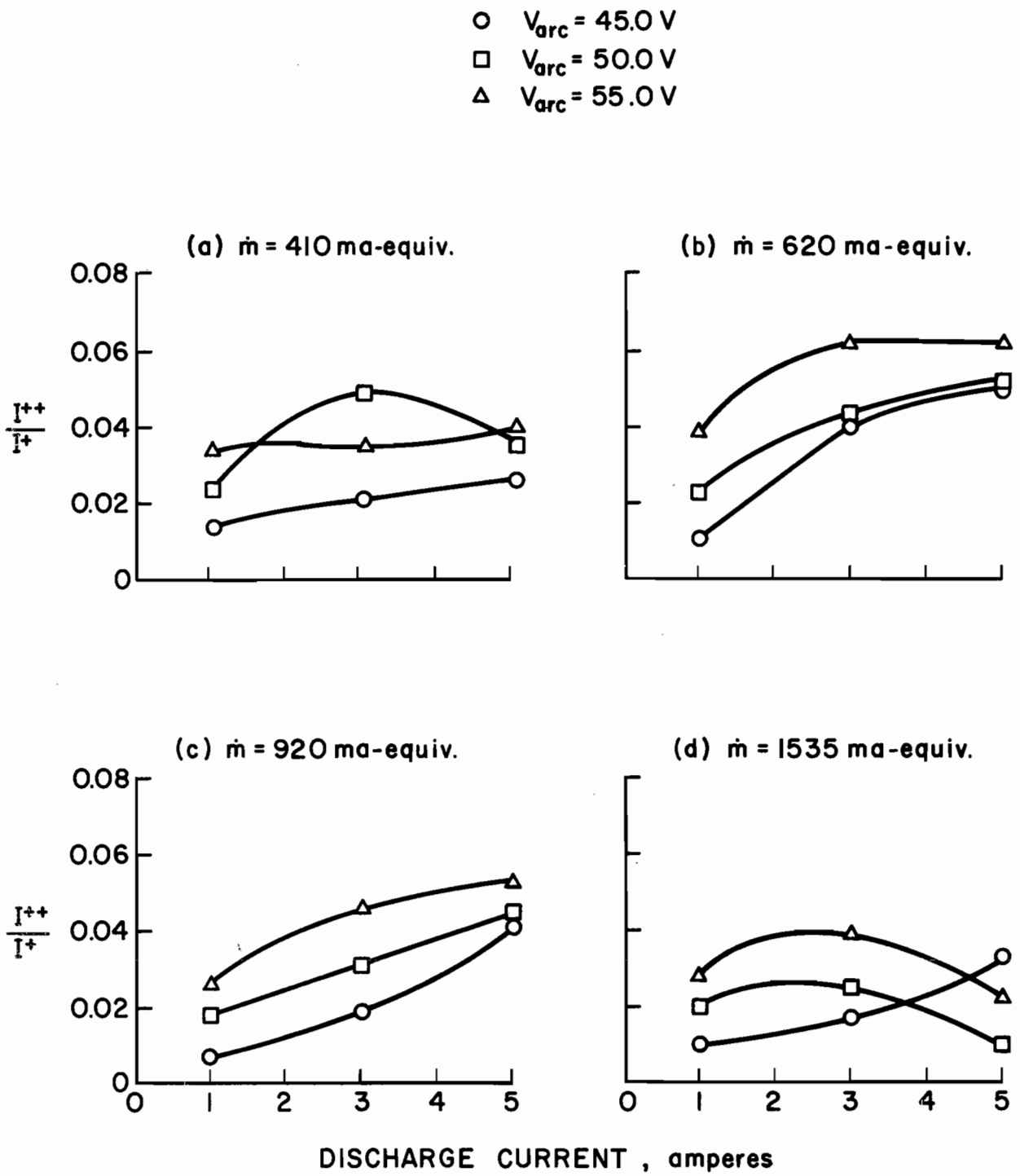

Figure A-1. Effect of discharge current and voltage on double to single ion current ratio for various flow rates with argon propellant.

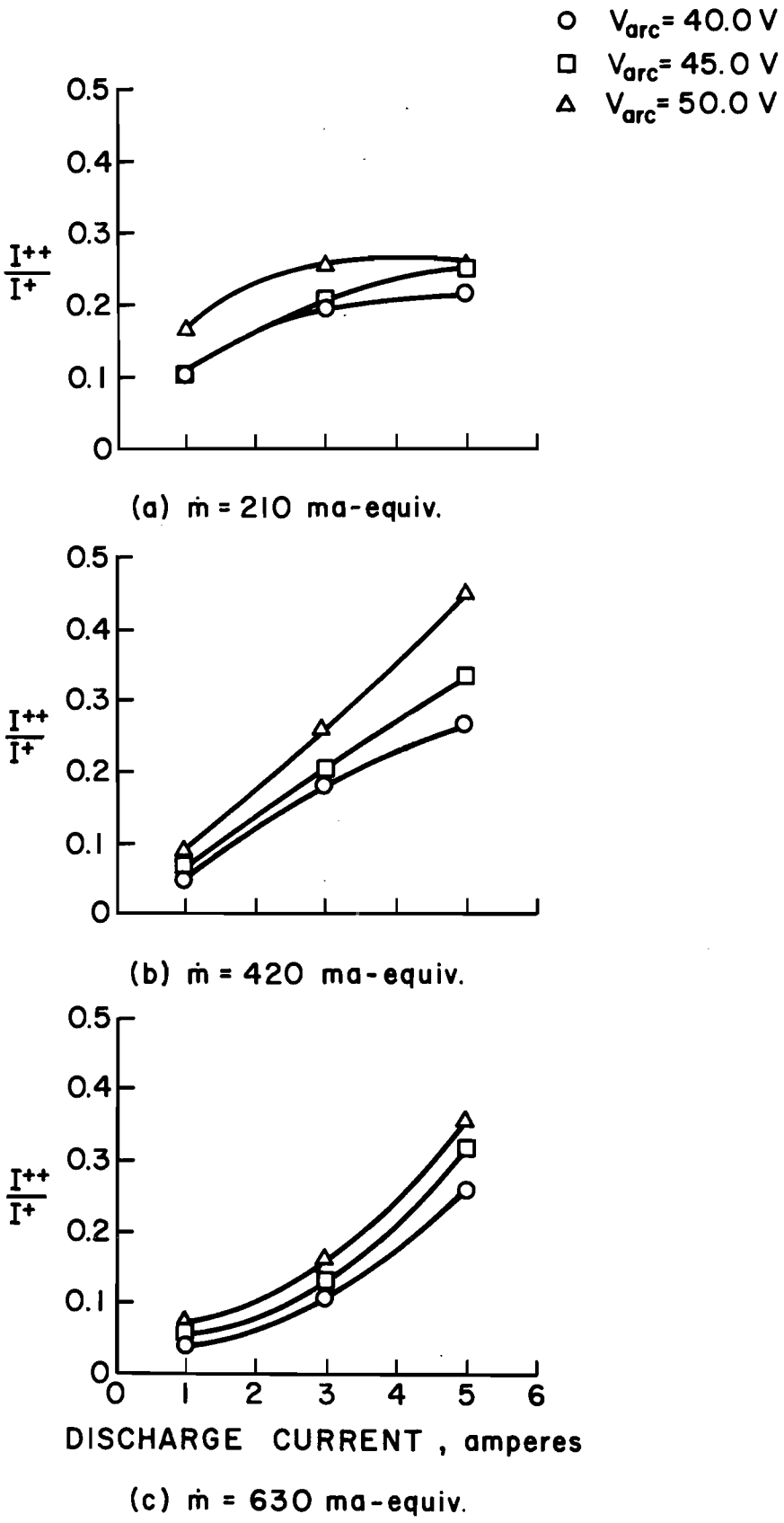

Figure A-2. Effect of discharge current and voltage on double to single ion current ratio for various flow rates with xenon propellant.

DISTRIBUTION LIST

	No. of Copies
National Aeronautics and Space Administration Washington, D. C. 20546	
Attn: RPE/Mr. Wayne Hudson	1
Mr. Daniel H. Herman, Code SL	1
National Aeronautics and Space Administration Lewis Research Center 21000 Brookpark Road Cleveland, Ohio 44135	
Attn: Research Support Procurement Section	
Mr. Allen Jones, MS 500-313	1
Technology Utilization Office, MS 3-19	1
Report Control Office, MS 5-5	1
Library, MS 60-3	2
N. T. Musial, MS 600-113	1
Spacecraft Technology Division, MS 501-8	
Mr. H. Douglass	1
Mr. R. Finke	1
Mr. D. Byers	1
Mr. B. Banks	1
Mr. S. Domitz	1
Mr. F. Terdan	1
Mr. W. Kerslake	1
Mr. Vincent K. Rawlin	20
Mr. M. Mirtich	1
Physical Science Division, MS 301-1	
Mr. W. E. Moeckel	1
National Aeronautics and Space Administration Marshall Space Flight Center Huntsville, Alabama 35812	
Attn: Mr. Jerry P. Hethcoate	1
Research and Technology Division Wright-Patterson AFB, Ohio 45433	
Attn: (ADTN) Lt. David A. Fromme	1
NASA Scientific and Technical Information Facility P. O. Box 8757 Baltimore/Washington International Airport Baltimore, Maryland 21240	40
Case Western Reserve University 10900 Euclid Avenue Cleveland, Ohio 44106	
Attn: Dr. Eli Reshotko	1
Royal Aircraft Establishment Space Department Farnborough, Hants, England	
Attn: Dr. D. G. Fearn	1

United Kingdom Atomic Energy Authority
Culham Laboratory
Abingdom, Berkshire, England
Attn: Dr. P. J. Harbour 1
Dr. M. F. A. Harrison 1
Dr. T. S. Green 1

National Aeronautics and Space Administration
Goddard Space Flight Center
Greenbelt, Maryland 20771
Attn: Mr. W. Isley, Code 734 1
Mr. R. Bartlett, Code 713 1
Mr. R. Callens, Code 734 1

SAMSO
Air Force Unit Post Office
Los Angeles, California 90045
Attn: Capt. D. Egan/SYAX 1

Comsat Laboratories
P. O. Box 115
Clarksburg, Maryland 20734
Attn: Mr. B. Free 1
Mr. O. Revesz 1

Rocket Propulsion Laboratory
Edwards AFB, California 93523
Attn: LKDA/Mr. Tom Waddell 2

DFVLR - Institut für Plasmadynamik
Technische Universitat Stuttgart
7 Stuttgart-Vaihingen
Allmandstr 124
West Germany
Attn: Dr. G. Krülle 1
Mr. H. Bessling 1

Giessen University
1st Institute of Physics
Giessen, West Germany
Attn: Professor H. W. Loeb 1

Jet Propulsion Laboratory
4800 Oak Grove Drive
Pasadena, California 91102
Attn: Dr. Kenneth Atkins 1
Technical Library 1
Mr. Eugene Pawlik 1
Mr. James Graf 1

Electro-Optical Systems, Inc.
300 North Halstead
Pasadena, California 91107
Attn: Mr. R. Worlock 1
Mr. E. James 1
Mr. W. Ramsey 1

Boeing Aerospace Company
P. O. Box 3999
Seattle, Washington 98124
Attn: Mr. Donald Grim 1

Intelcom Rad Tech
7650 Convoy Court
P. O. Box 80817
San Diego, California 92138
Attn: Dr. David Vroom 1

Lockheed Missiles and Space Company
Sunnyvale, California 94088
Attn: Dr. William L. Owens
Propulsion Systems, Dept. 62-13 1

Fairchild Republic Company
Farmingdale, New York 11735
Attn: Dr. William Guman 1

COMSAT Corporation
950 L'Enfant Plaza SW
Washington, D. C. 20024
Attn: Mr. Sidney O. Metzger 1

Electrotechnical Laboratory
Tahashi Branch
5-4-1 Mukodai-Machi, Tanashi-Shi
Tokyo, Japan
Attn: Dr. Katsuva Nakayama 1

Office of Assistant for Study Support
Kirtland Air Force Base
Albuquerque, New Mexico 87117
Attn: Dr. Calvin W. Thomas OAS Ge 1
Dr. Berhart Eber OAS Ge 1

Bell Laboratories
600 Mountain Avenue
Murray Hill, New Jersey 07974
Attn: Dr. Edward G. Spencer 1
Dr. Paul H. Schmidt 1

Massachusetts Institute of Technology
Lincoln Laboratory
P. O. Box 73
Lexington, Massachusetts 02173
Attn: Dr. H. I. Smith 1

Sandia Laboratories
Mail Code 5742
Albuquerque, N.M. 87115
Attn: Mr. Ralph R. Peters 1

Service du Confinement des Plasma
Centre d'Etudes Nucléaires - F.A.R.
B.P. 6
92260 Fontenay-aux-Roses
France
Attn: Dr. J. F. Bonal 1